Projected changes in a multiscale environment: the subpolar North Atlantic Ocean

A Dissertation
Presented to
The Academic Faculty

by

Filippos Tagklis

In Partial Fulfillment
of the Requirements for the Degree
Doctor of Philosophy in the
School of Earth and Atmospheric Sciences

Georgia Institute of Technology
December 2020

Projected changes in a multiscale environment: the subpolar North Atlantic Ocean

Approved by:

Dr. Annalisa Bracco, Advisor
School of Earth and Atmospheric Sciences
Georgia Institute of Technology

Dr. Takamitsu Ito, co-Advisor
School of Earth and Atmospheric Sciences
Georgia Institute of Technology

Dr. Emanuele Di Lorenzo
School of Earth and Atmospheric Sciences
Georgia Institute of Technology

Dr. Renato M Castelao
Department of Marine Sciences
University of Georgia

Dr. Vincenzo Artale
Italian National Agency for New Technologies, Energy and Sustainable Economic Development (ENEA)

Date Approved: November 2nd, 2020

ACKNOWLEDGEMENTS

First and foremost, I would like to express my deepest appreciation to my thesis advisors, Prof. Annalisa Bracco and Prof. Takamitsu Ito. Without their assistance and dedicated involvement in every step throughout the process, this work would have never been accomplished. I would like to thank you very much for your support and understanding over these past 5 years.

I would also like to show gratitude to my committee, including Prof. Emanuele DiLorenzo, Prof. Renato M Castelao and Dr. Vincenzo Artale for the thoughtful comments and recommendations on this dissertation.

Finally, I wish to thank my friends and family, especially my parents Panagiotis and Eleni for their support and encouragement throughout my study and life abroad.

TABLE OF CONTENTS

LIST OF TABLES

LIST OF FIGURES

SUMMARY

By the end of this century, the marine environment will markedly change in response to anthropogenic stressors and increasing greenhouse gas emissions. Ocean circulation and the horizontal and vertical transport of heat, salt, carbon, oxygen and nutrients will be impacted. In response to rising temperatures, stratification will increase in most of the world oceans, affecting ventilation of the deep ocean and nutrient transport from the deep and nutrient-rich waters to the euphotic layer. Seawater will become more acidic as well, as atmospheric carbon dioxide is taken up by the ocean and redistributed by its circulation, and will lose oxygen.

The key areas in the process of replenishing the global oceans with newly ventilated water are those where open ocean deep convection and deep-water formation occurs. In the North Atlantic (NA), the Labrador Sea (LS) is one of such regions and the best observed. The LS acts as a window where the ocean takes up heat, oxygen and carbon dioxide from the atmosphere. The evaluation of historical and future climate model simulations reveals a weakening of convective events in the Labrador Sea, and a declining of dissolved O_2 concentrations in the subsurface waters because of increased stratification and lower solubility in a warming climate. However, state-of-the-art climate models are not yet capable of reproducing the spatial and temporal characteristics of convection and hydrography over the Subpolar North Atlantic. Climate model biases, and their limitation in representing physical transport and biogeochemical cycling correctly, reduce confidence in, and limit reliability of, future projections in representing the Atlantic Meridional Overturning Circulation (AMOC) and the gas inventories.

In this thesis I will investigate how Global Climate Models (GCMs) represent convective variability in the NA and LS, and I will diagnose few major sources of GCMs biases and their role in simulating the NA circulation and LS convection.

In the first half of this work, I present analyses of state-of-the-art Earth Systems Models (ESMs) included in the Coupled Model Intercomparison Project Phase 5 (CMIP5), to investigate their skill in representing the physics and biogeochemistry with attention paid to oxygen and nutrient inventories. Furthermore, I take a close look at the mechanisms that regulate the changes of oxygen and nutrients in the subtropical and subpolar NA region at centennial timescales.

In the second half of my doctoral work, I introduce simulations performed with a state-of-art high-resolution regional ocean model to investigate how ocean turbulence impact the representation of deep convection in the LS. I investigate the transport pathways and the ultimate fate of the Irminger Current water from the continental slope along the west coast of Greenland to the Labrador Sea interior, and I show that submesoscale processes modulate this transport and in turn the stratification of the Labrador Sea interior, by controlling strength and lifespan of the coherent vortices formed along West Greenland. Including the representation of these processes ultimately impacts the amount of the Labrador Sea Water formed in the simulation, and therefore modifies the representation of the Atlantic Meridional Overturning Circulation. A linear relationship describes the dependence between the multi-year mean convective volume and the vorticity (or frontogenic tendency), opening to the possibility of simple parameterizations to account for the advective submesoscale contribution in GCMs.

CHAPTER 1. INTRODUCTION

1.1 Labrador Sea Background

The Labrador Sea (LS) is one of the two major sites of the North Atlantic where significant densification and deep convection occurs. Intense air-sea interactions in wintertime weaken the ambient stratification and result in convective mixing both in its interior and over its shelves (Marshall and Schott 1999, Pickart, Torres et al. 2002). Deep convection mixes the surface waters to depths exceeding 2000 m [(Clarke and Gascard 1983), Lazier (1988), (Lazier, Hendry et al. 2002, Yashayaev 2007, Yashayaev, Bersch et al. 2007)] and forms the fresher and colder highly oxygenated water mass, the Labrador Sea Water (LSW). LSW spreads across the northwest Atlantic (Talley and McCartney 1982) at mid-depths, flowing southward as part of the North Atlantic Deep Water (NADW) and contributing in the transport of heat, oxygen, carbon dioxide and freshwater in the Atlantic Ocean.

According to observations, the Labrador Basin undergoes significant inter-annual to decadal variability (Lazier 1988, Lazier, Hendry et al. 2002, Yashayaev 2007, Yashayaev and Seidov 2015), and the hydrographic characteristics of LS exhibited significant changes over the past six decades. Variability in LS deep convection subsequently propagates throughout the NA (Talley and McCartney 1982, Curry, McCartney et al. 1998) and impacts the Atlantic component of the Meridional Overturning Circulation (AMOC).

Schematically, the AMOC has a surface branch of warm and salty waters, the North Atlantic Current (NAC), flowing northward in the Atlantic, where the NAC loses heat to the atmosphere becoming, in winter, colder and denser enough to sink across the

Greenland-Iceland-Scotland Ridge (Figure 1.1). Another portion of the NAC warm waters veer westward and around Greenland, sinking in the LS and forming the LSW. Thus, it is not a surprise that a direct connection between convective variability in the LS and overall AMOC signals has been found in recent modeled studies (Biastoch, Boening et al. 2008, Danabasoglu, Yeager et al. 2012, Danabasoglu, Yeager et al. 2014, Danabasoglu, Yeager et al. 2016). Observational data remain inconclusive on this point so far.

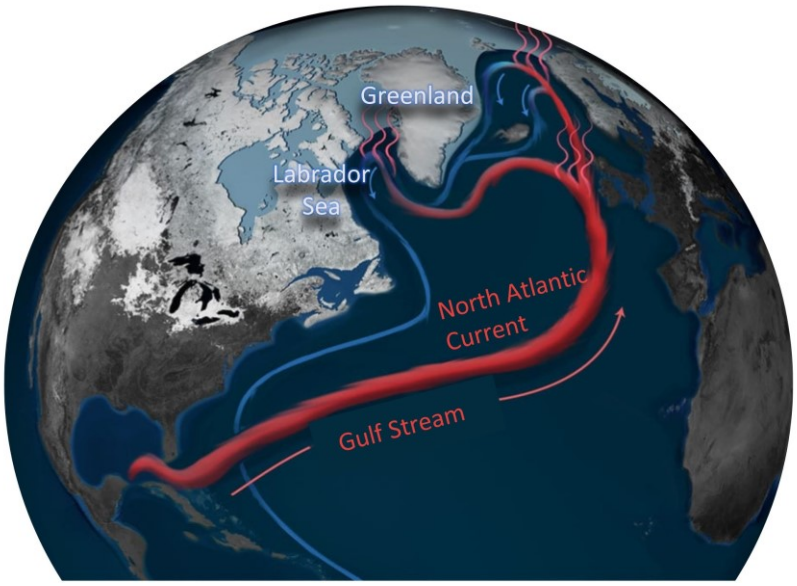

Figure 1. 1 Schematic of Atlantic Meridional Overturning Circulation (AMOC).

1.2 Hydrography, Circulation and Eddies

The Labrador Sea receives waters from three separate regions; the Nordic seas, Baffin Bay and the North Atlantic. Warm and saline Atlantic Water (AW) is carried near the ocean surface by the western branch of the North Atlantic Current (NAC), while cold and fresh water originated in the Polar Regions and known as the Arctic Outflow is transported into the LS from the Denmark Strait through the Irminger Basin. The surface circulation is cyclonic, intensified along the boundaries. Near the surface, the currents system consists of two relatively fast currents, the West Greenland Current (WGC) and the Labrador Current (LC). The WGC transports fresh and cold water originating from the Nordic Seas and enters the LS through a westward pathway along the Greenland coast. Along with the WGC, the warmer and saltier Irminger Sea Water (ISW) flows underneath and offshore of WGC via the Irminger Current (IC). The IC plays a significant role in the restratification of the whole basin (Cuny, Rhines et al. 2002) and keeps the LS warm enough preventing the ice formation in the central LS, while the western boundary along the Labrador coast is ice-covered for several months of the year. Lastly, the Labrador Current carries cold and fresh water from the Baffin Bay south-eastward along the Labrador coast. A schematic of the three major surface currents (WGC, IC, LC) is presented in **Figure 1.2 (A, B)**.

Eddy transport is key in the LS. Three types of eddies are observed in the LS and each one plays an important role in the heat budget, and the convection cycle. Near 62°N, 52°W and off the west Greenland coast there is a region of high eddy activity where the 3000 meters isobath separates from the shelf **Figure 1.2 (C, D)**. The eddies formed in this area are called Irminger Rings (IRs). They have warm-salty cores because they carry IC waters, and they can release heat and salt in the LS interior, as they approach the convective region (CR)

(Bracco and Pedlosky 2003, Lilly, Rhines et al. 2003, Hatun, Eriksen et al. 2007). The second type of eddies are the boundary current eddies formed along the Greenland coast by baroclinic instability of the boundary current system (Spall 2004). Finally, convective eddies are generated by baroclinic instability of the convective patch (Jones and Marshall 1997); they are the smallest of the three, and their representation requires the use of non-hydrostatic models.

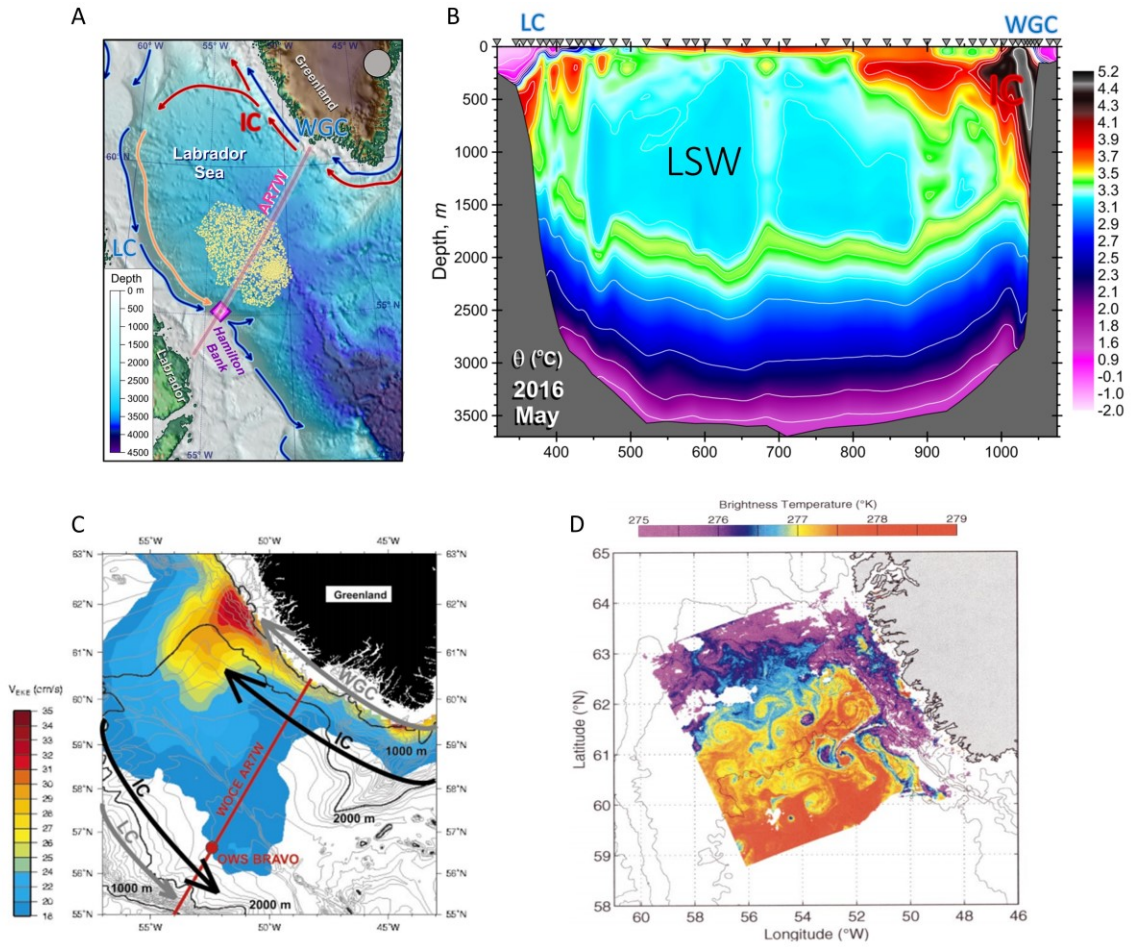

Figure 1. 2 A) Schematic of the Surface Circulation and AR7W repeated hydrography line. B) Labrador Sea (AR7W Section) potential temperature (Courtesy of Igor Yashayaev, BIO). C) Colors depict the equivalent eddy speed V EKE deduced from the sea surface height variability (Katsman, Spall et al. 2004). D) Sea surface brightness temperature image of the northern Labrador Sea (Prater 2002).

The analysis of combined observations (Yashayaev 2007, Yashayaev and Seidov 2015)], has revealed that hydrographic characteristics and convective events in the LS varied significantly over the past six decades. Between the mid-1960s and early 1970s, the whole basin was extremely warm and salty, in contrast to a colder and fresher period between the late 1980s and mid-1990s. According to (Dickson, Yashayaev et al. 2002, Curry and Mauritzen 2005), the two different states were not observed only in the LS but in the entire subpolar NA**.** These changes were reflected in different characteristics of the water masses formed during convective events and in different strenghts of the convective events in the various winter seasons.

Several factors contribute to the LS hydrographic variability including variability in the winter heat fluxes local to the LS, variability in the heat losses to the atmosphere, heat, and salt gained from tropical Atlantic waters that are carried northward into the LS, and variability in freshwater input due to ice melting from the Arctic and Greenland, continental runoff and precipitation.

1.3 Objectives of this dissertation

Due to increasing anthropogenic greenhouse gas emissions, consequent warming, and more generally environmental stressors, the marine environment is projected to change markedly in terms of circulation, stratification, nutrient and oxygen availability, and carbon dioxide concentrations and uptake. The first part of this work examines the mechanisms driving the larger scale trends of physical and chemical properties in the North Atlantic (yellow shaded area in Figure 1.3) in the context of the state-of-the-art ESMs from the Coupled Model Intercomparison Project phase 5 (CMIP5). Chapter 2 examines the centennial scale changes of circulation, stratification and dissolved oxygen in the subpolar North Atlantic, and Chapter 3 examines the broader response of the North Atlantic in comparison to the North Pacific in the context of nutrients availability, export production and dissolved oxygen utilization. The second part of this work examines in-depth the model representation of the dynamics of the Labrador Sea basin (red shaded area in Figure 1.3). Chapter 4 examines the sources of biases impacting the physical representation of LS circulation and deep convection activity through the lenses of regional ocean-only numerical simulations.

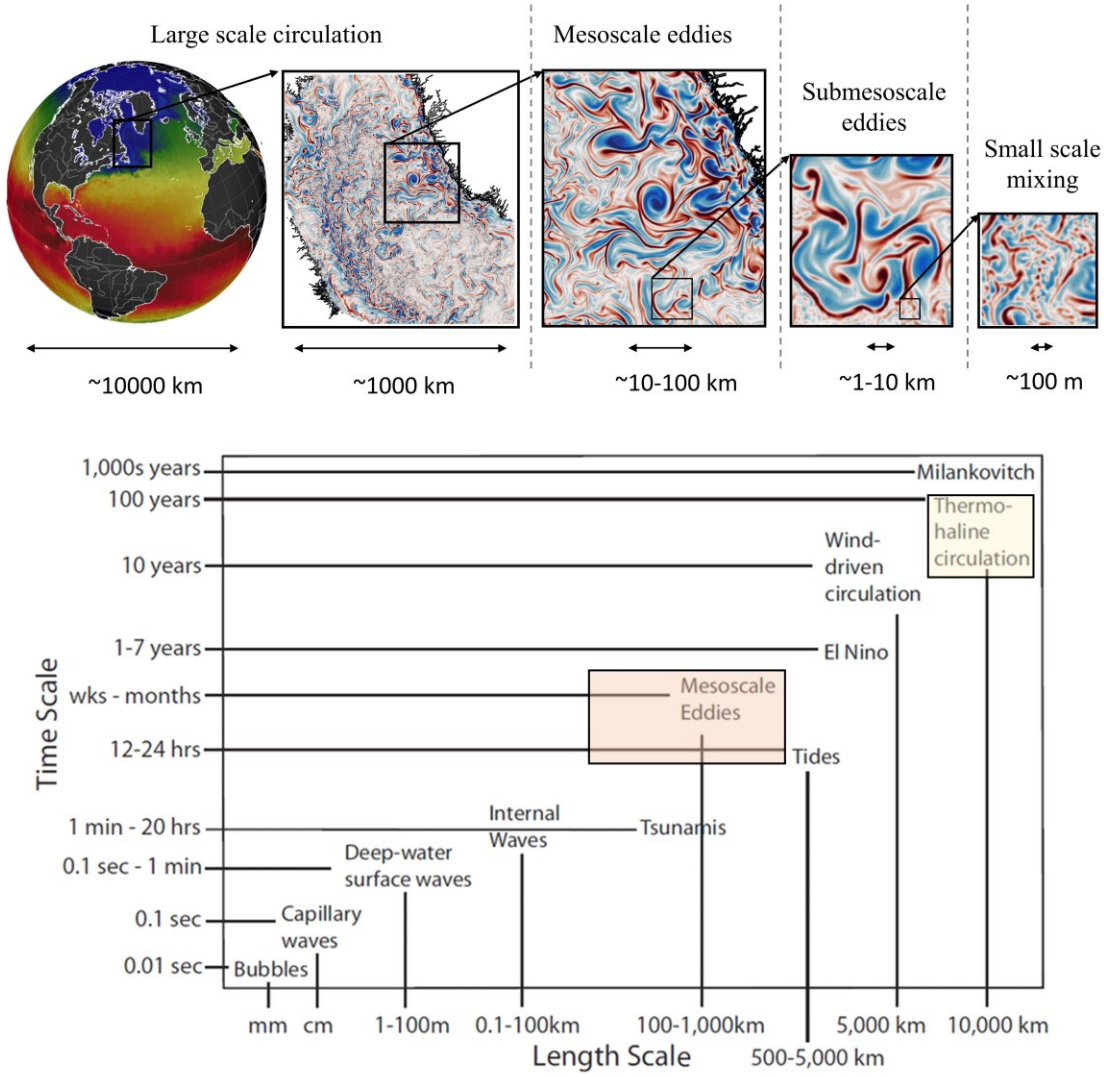

Figure 1. 3 (Top) Schematic illustrating the lateral scale of oceanic flows from large scale circulation (L~10^5km), mesoscale eddies (L~ 10-10^3km), sub mesoscale eddies and filaments (L~ 1-10km), and small scale mixing L~10^0m. (Bottom) Temporal and spatial scales of oceanographic phenomena adapted from (Talley, Pickard et al. 2011). Shaded areas indicate the temporal and spatial scales focused on in this research.

CHAPTER 2. PHYSICALLY DRIVEN PATCHY O2 CHANGES IN THE NORTH ATLANTIC OCEAN SIMULATED BY THE CMIP5 EARTH SYSTEM MODELS

Published as

Tagklis, F., Bracco, A., Ito, T. (2017) Physically driven patchy O_2 changes in the North Atlantic Ocean simulated by the CMIP5 Earth System Models. Global Biogeochem. Cycles, doi:10.1002/2016GB005617

Abstract

The subpolar North Atlantic is a key region for the oceanic uptake of heat, oxygen and carbon dioxide. Centennial oxygen (O_2) changes are investigated in the upper 700 m of the North Atlantic Ocean using a subset of Earth System Models (ESMs) included in the Coupled Model Intercomparison Project Phase 5. The climatological distributions of dissolved O_2 averaged for the recent past period (1975-2005) are generally well captured although the convective activity differs among the models in space and strength, and most models show a cold bias south of Greenland. By the end of the 21st century, all models predict an increase in depth-integrated temperature of 2-3ºC, resultant solubility decrease, weakened vertical mass transport, decreased nutrient supply into the euphotic layer, and weakened export production. Despite an overall tendency of the North Atlantic to lose oxygen, patchy regions of O_2 increase are observed due to the weakening of the North Atlantic Current (NAC) causing a regional solubility increase (the *warming hole* effect) and a decrease in the advection of subtropical, low-O_2 waters into the subpolar regions (the *nutrient stream* effect). Additionally, a shift in the NAC position contributes to localized

O_2 changes near the boundaries of water masses. The net O_2 change reflects the combination of multiple factors leading to highly heterogeneous and model-dependent patterns. Our results imply that changes in the strength and position of the NAC will likely play crucial roles in setting the pattern of O_2 changes in future projections.

2.1 Introduction

Marine ecosystems will likely face multiple stressors as a consequence of the increasing anthropogenic emissions of CO2 and of the induced climate warming in this and coming centuries. The oceans are "warming up, turning sour, and losing breath" as summarized by (Gruber 2011). Temperature increase, ocean acidification and ocean deoxygenation are global-scale phenomena with far-reaching influences on the ecosystem and biogeochemical cycling. Ocean deoxygenation, i.e. the decline of dissolved oxygen (O2) from the water column, is the least understood problem among the three, despite its profound influence on marine habitat and redox-sensitive biogeochemical tracers (Kleypas, Buddemeier et al. 1999, Gray, Wu et al. 2002, Feely, Sabine et al. 2004, Grantham, Chan et al. 2004, Orr, Fabry et al. 2005, Kleypas , Feely RA et al. 2006, Poertner and Knust 2007, Doney, Ruckelshaus et al. 2012) .

In a warming climate, the higher temperature of seawater decreases the solubility of oxygen. Additionally, upper ocean stratification may increase due to the surface warming, melting of polar ice cap at high latitudes and an increase in precipitation, weakening the ventilation of well-oxygenated surface waters into the ocean interior (Sarmiento, Hughes et al. 1998, Matear, Hirst et al. 2000, Bopp, Le Quere et al. 2002, Plattner, Joos et al. 2002,

Froelicher, Joos et al. 2009). Earth System Model (ESM) simulations indeed predict a strong sensitivity of ocean's O2 content to climate warming, suggesting a significant decline in global O2 inventory by the year 2100 especially in the extratropical thermocline (Keeling, Koertzinger et al. 2010). Regional differences, however, remain significant among models (Bopp, Resplandy et al. 2013, Cocco, Joos et al. 2013).

The reinforcing mechanisms above, thermally-driven decrease of solubility and stratification-driven decrease of ocean ventilation, can be particularly important in regions of deep water formation such as the subpolar North Atlantic. Convective mixing is the most important mechanism by which the water column is ventilated and oxygenated (Kortzinger, Schimanski et al. 2004). For example, in the Labrador Sea (LS), deep convection mixes the surface waters to depths exceeding, at times, 2,000 meters (Lazier 1980, Clarke and Gascard 1983, Lazier, Hendry et al. 2002, Yashayaev 2007, Yashayaev, Bersch et al. 2007) and forms the fresh and cold, highly oxygenated dense water mass, the Labrador Sea Water (LSW). The LS is a highly dynamic region for the biogeochemical tracers. The historic O2 observations for the last 60 years do not yet exhibit a statistically significant trend but are dominated by the interannual and decadal varibility, indicating direct linkages between the strength of convective mixing, ventilation and oxygen concentrations (van Aken, de Jong et al. 2011). For the entire North Atlantic, the basin-scale O2 inventory is also relatively constant but consists of compensating changes within the basin likely due to the circulation variability (Stendardo and Gruber 2012). However, unabated warming of the Arctic will continue melting of both Arctic sea ice (Gillett, Stone et al. 2008) and terrestrial glaciers over Greenland (Rignot, Box et al. 2008, Mernild and Liston 2012), with the end result that more freshwater can converge into the Labrador Sea (Dickson, Rudels et al. 2007) and

possibly influence convective rates in the future (Stouffer, Yin et al. 2006, Boning, Behrens et al. 2016, Luo, Castelao et al. 2016). The LSW spreads across the northwest Atlantic at mid-depths (Talley and McCartney 1982, Curry, Duplessy et al. 1988, Bower, Lozier et al. 2009), flowing southward as a component of the North Atlantic Deep Water. Thus the oxygen trends and variability in the LS can impact throughout the subpolar North Atlantic the global deep oceans. A present concern is if, when and how a slowdown in deepwater formation in the North Atlantic will reduce the oxygen input to the deep ocean.

The primary objective of this study is to investigate the mechanisms driving the regional trends of dissolved oxygen in the subtropical and subpolar North Atlantic in the context of the state-of-the-art ESMs from the Coupled Model Intercomparison Project phase 5 (CMIP5). Both ocean-only and coupled climate models display large biases and divergent behavior in simulating the formation of deep water masses and their variability (Canuto, Howard et al. 2004, MacMartin, Tziperman et al. 2013, Danabasoglu, Yeager et al. 2014, Danabasoglu, Yeager et al. 2016). We will, therefore, begin our investigation by testing the ability of the ESMs to reproduce the present mean state of relevant physical and biogeochemical variables. Particular attention will be paid to the representation of the convection and hydrographic structure in the North Atlantic. We do not expect the CMIP5 models to reproduce the trajectories of the climate and biogeochemical variability perfectly, but we aim at evaluating the linkages between physical climate and biogeochemical variables and how similar or different they are across the models. We will then move on to analyze the model projections to the end of the 21st century focusing on commonalities about models and causes for divergence.

2.2 Data and Methods

We analyze a subset of CMIP5 ESMs used for the Intergovernmental Panel on Climate Change (IPCC) Fifth Assessment Report (AR5) for which all the variables of interest are available. We examine the transient simulations from 1850 to 2100 by combining the historical integrations and future projections based on the Representative Concentration Pathway 8.5 scenario (Riahi, Rao et al. 2011, Taylor, Stouffer et al. 2012). The CMIP5 ESMs used in this study are summarized in Table 2.1. The list includes the Community Earth System Model, CESM1-BGC (Long, Lindsay et al. 2013, Moore, Lindsay et al. 2013), two versions of the Geophysical Fluid Dynamics Laboratory (GFDL) Earth System Model, GFDL-ESM2G and GFDL-ESM2M (Dunne, John et al. 2013); two versions of the Hadley Center Global Environment Model version 2, HadGEM2-ES and HadGEM2-CC (Collins, Bellouin et al. 2011), two versions of the Institute Pierre Simon Laplace model, IPSL-CM5A-LR, IPSL-CM5A-MR (Dufresne, Foujols et al. 2013); two versions of the Max Plank Institute model, MPI-ESM-LR and MPI-ESM-MR (Giorgetta, Jungclaus et al. 2013), and NorESM1-ME (Bentsen, Bethke et al. 2013). GFDL-ESM2G and GFDL-ESM2M differ in their ocean module and vertical coordinate system with ESM2M using depth-based coordinates and the Modular Ocean Model (MOM) and ESM2G using isopycnal coordinates and the Generalized Ocean Layered Model (GOLD) (Adcroft and Hallberg 2006). The same atmospheric component is used for both versions. HadGEM2-CC increases the vertical discretization of the atmospheric module from the 38 layers in HadGEM2-ES to 60 but does not include the atmospheric chemistry scheme used in the –ES version. IPSL-A-LR and IPSL-A–MR use different resolution in the atmospheric module (1.875° × 3.75° in the LR for low resolution and 1.25° × 2.5° in the MR for medium

resolution). Finally, the MPI-ESM-MR configuration doubles the number of levels in the atmosphere and decreases the horizontal grid spacing of the ocean, compared to the LR setup.

Table 2. 1 CMIP5 modeling groups and model names.

Modeling Group/Center	Model Name	Reference
NOAA Geophysical Fluid Dynamics Laboratory (NOAA GFDL)	GFDL-ESM2M GFDL-ESM2G	[*Dunne et al.*, 2013]
Institute Pierre-Simon Laplace (IPSL)	IPSL-CM5A-LR IPSL-CMA-MR	[*Dufresne et al.*, 2013]
Met Office Fluid Hadley Center (MOHC)	HadGEM2-ES HadGEM2-CC	[*Collins et al.*, 2011] [*Jones et al.*, 2011]
Max Plank Institute for Meteorology (MPI)	MPI-ESM-LR MPI-ESM-MR	[*Giorgetta et al.*, 2013]
Community Earth System Model Contributors (CESM1)	CESM1-BGC	[*Long et al.*, 2013] [*Moore et al.*, 2013]
Norwegian Climate Centre (NCC)	NorESM1-ME	[*Bentsen et al.*, 2013]

The three-dimensional and annually averaged fields analyzed in this study are first interpolated horizontally onto a common domain of 1° x 1° longitude-latitude grid and vertically onto 33 depth levels. The variables we focus on are dissolved oxygen (O_2), temperature T, salinity S, particulate organic carbon export (EP), and the horizontal velocities (U, V). Further, potential density, stratification and oxygen saturation $O_{2,sat}$ are calculated from T and S.

Regarding oxygen, it has been shown that in the CMIP5 ESMs the biogeochemical tracers are not always equilibrated with respect to the ocean circulation and a drift may be present. To account for the magnitude and sign of the model drift, in all subsequent analyses we used the pre-Industrial Control simulations (piControl) and removed the (small) signal unrelated to externally forced centennial changes. We did so by defining, for example,

$O_{2_{trend}} = O_2^{rcp8.5(B)} - O_2^{hist(A)} - (O_2^{piControl\,(B)} - O_2^{piControl\,(A)})$ where A and B define the periods 1975-2005 and 2070-2100.

Stratification is calculated here as the potential density difference between the surface and 700 m, modifying the definition of (Capotondi, Alexander et al. 2012) relevant for tropical latitudes that considered the difference between surface and 200 m. Potential density is calculated from the modeled temperature and salinity fields using the EOS-80 polynomial. Oxygen saturation depends on temperature and salinity and is calculated based on (Garcia. and Gordon 1992). Apparent oxygen utilization (AOU) is then determined as the difference between the $O_{2,sat}$ and O_2, which is commonly used as a measure of biological oxygen utilisation. It should be noted that intense wintertime air-sea interaction often causes surface O_2 to be under-saturated leading to a non-negligible preformed AOU (Ito, Follows et al. 2004) but the model outputs do not allow for a more precise estimation. The CMIP5 ESMs are compared to the climatological observations for the present climate. Annual mean climatologies from the World Ocean Atlas 2009 (WOA 2009) (Antonov, D. Seidov et al. 2010, Garcia, R. A. Locarnini et al. 2010, Locarnini, A. V. Mishonov et al. 2010) are used as the observational reference of T, S, and O_2. Potential density, density stratification, oxygen saturation $O_{2,sat}$ and AOU are calculated using the same formula. For the ocean currents, we reference to the Simple Ocean Data Assimilation Reanalysis SODA 2.2.4 (Carton, Giese et al. 2005). SODA 2.2.4 is based on a multivariate sequential data assimilation scheme in which T and S observations from World Ocean Database 2009 are used to update the ocean model.

2.3 Results

2.3.1 Model evaluation

2.3.1.1 Domain average changes

Before examining the spatial variability of the oxygen trends and their causes, we describe the time evolution of the spatially averaged (volume weighted mean) anomalies of the quantities of interest for the entire North Atlantic (22°N-73°N; figure 2.1) from 1950 to 2100. Given our focus on deep mixing and deep water formation, we concentrate on the depth range 0-700 meters. The choice of 700 meters is somewhat arbitrary but represents a typical depth at which most models convect on a large enough area. The anomalies in figure 2.1 are calculated on the mean state of period 1975-2005 (period A) and the climatological volume weighted mean values from WOA are also indicated. Mean values are also shown for the projected interval 2070-2100 (period B). As expected, temperature and stratification increase and oxygen decreases in all models. The overall oxygen loss over 1950 to 2100 is in the range of 10-20 $mmolm^{-3}$, and is directly linked to the solubility decrease associated with the NA warming. Salinity and AOU trends, on the other hand, differ among the models and their magnitude is moderate, within (-0.35, +0.1) psu and ±5 mmol m^{-3} for the entire North Atlantic.

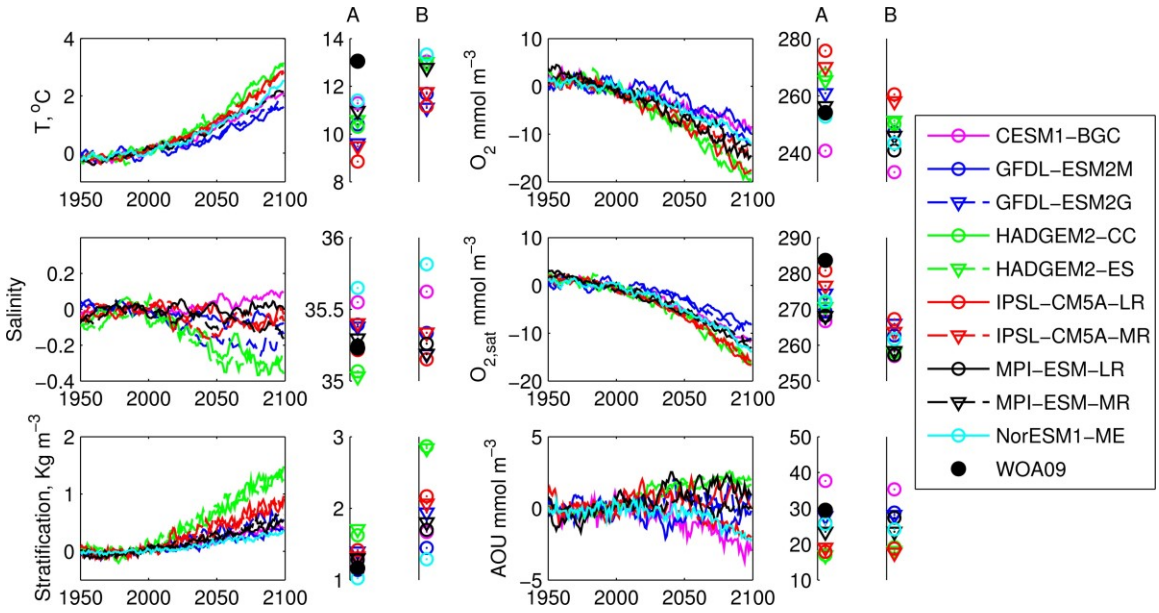

Figure 2. 1 Volume weighted mean time series anomalies over the North Atlantic (22ºN-73ºN) of temperature (T), salinity (S), stratification, dissolved oxygen, oxygen saturation (O2sat) and apparent oxygen utilization (AOU) over the period 1950-2100. The stratification index is defined as the density difference between 700 meters and surface. Mean values are also shown in the past and projected intervals 1975-2005 (period A) and 2070-2100 (period B).

In figure 2.2, we present the spatially averaged changes of each variable by dividing our domain in subtropical (22ºN-46ºN) and subpolar (46ºN-73ºN) regions. Both in the SPNA and STNA, all of the models warm up and increase their stratification (figure 2.2a, c). Salinity increases for all the models (figure 2.2b) in the STNA region except for the HadGEM versions which freshen at the eastern subtropical gyre and show a strong zonal ΔS gradient as revealed in the following (figure 2.12). In the SPNA, all the models but NorESM1-ME show negative salinity change (figure 2.2b). As revealed by the spatial changes (figure 2.12), NorESM1-ME significantly increases salinity in the eastern subpolar gyre counter balancing the freshening in the rest of the subpolar region. Along with warming, stratification also increases for all of the models in the whole NA (figure 2.2c).

The most diverse behavior is observed in the centennial AOU changes both among the different models but also between SPNA and STNA (figure 2.2d).

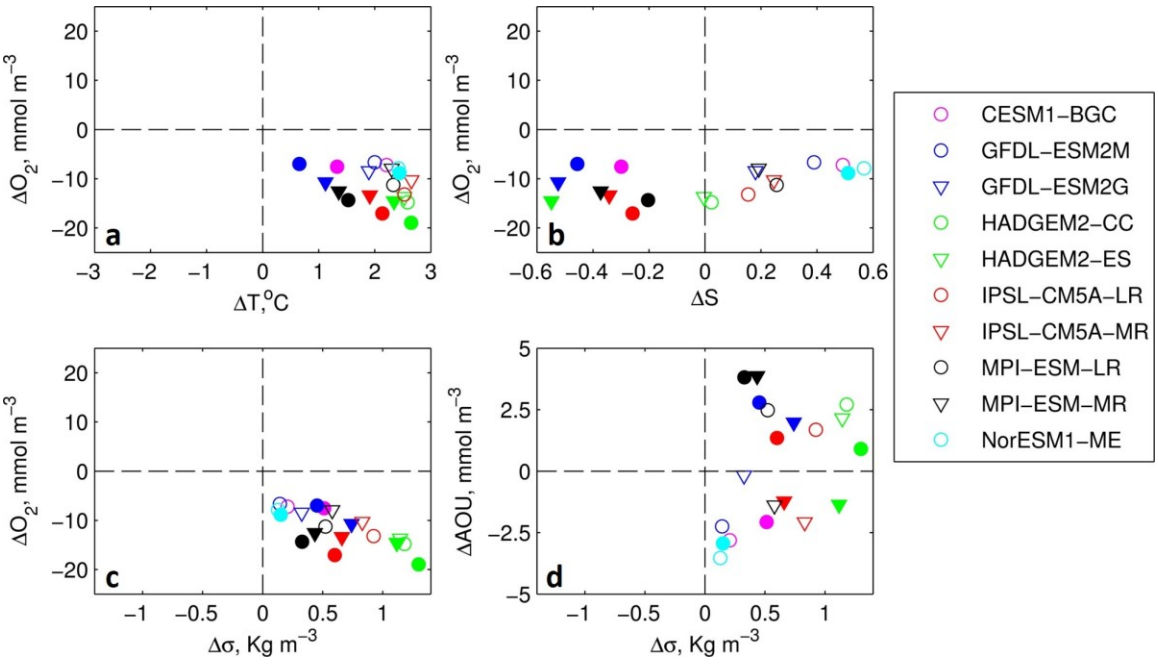

Figure 2. 2 Spatially averaged changes of dissolved oxygen (ΔO_2) along with a) temperature (ΔT), b) salinity (ΔS) ,c) stratification ($\Delta\sigma$) and d) apparent oxygen utilization ΔAOU along with stratification ($\Delta\sigma$). Filled shapes represent averaging over SPNA (46°N-73°N) and empty shapes represent averaging over STNA (22°N-46°N).

In this work we focus on the spatial representation of physical and biogeochemical quantities related to oxygen and we concentrate on centennial changes. Figure 2.1, however, shows hints of interannual variability superposed to a strong centennial trend in most variables. It remains to be determined how well CMIP5 models represent this component. Due to the limited measurements available, the temporal variability of dissolved oxygen on interannual to decadal scales cannot be easily determined over the whole North Atlantic and therefore cannot be effectively compared to that in the models. Under the assumption that the AMOC is its main driver, however, the analysis of the AMOC representation in CMIP5 has shown that most models display multidecadal variability with an approximate 60-yr periodicity (Cheng et al., 2013) but generally underestimate the observed interannual-to-decadal changes between 1850 and 2005.

2.3.1.2 Biases and Climatological Spatial fields

Next, we focus on the spatial representation of the physical and biogeochemical fields associated with oxygen variability in the North Atlantic. First, we investigate the historical period, using reanalysis products and WOA to validate the model outputs. Again, we analyse the set of variables indicated earlier and we consider their climatological means over 1975-2005 (period A) averaged over the depth range from the surface to 700 meters.

Common patterns of model biases emerge in temperature (T), salinity (S) and dissolved oxygen (O2), as shown in figures 2.3-5, respectively. The most noticeable bias common to all three variables, and among all model realizations but two, is a cold, fresh and overly oxygenated patch centered at about 48oN and 45oW. This feature is not relevant to GFDL-ESM2G and is only marginally apparent in GFDL-ESM2M. The O2 overestimation (figure 2.5) results from oxygen solubility, which reflects the cold bias in temperature. A similar pattern in the T-S structure was observed in the majority of the eighteen global ocean-sea-ice models forced by a common prescribed atmospheric state and run as part of the Coordinated Ocean-ice Reference Experiments - Phase II (CORE-II) (Danabasoglu, Yeager et al. 2014, Griffies, Yin et al. 2014).

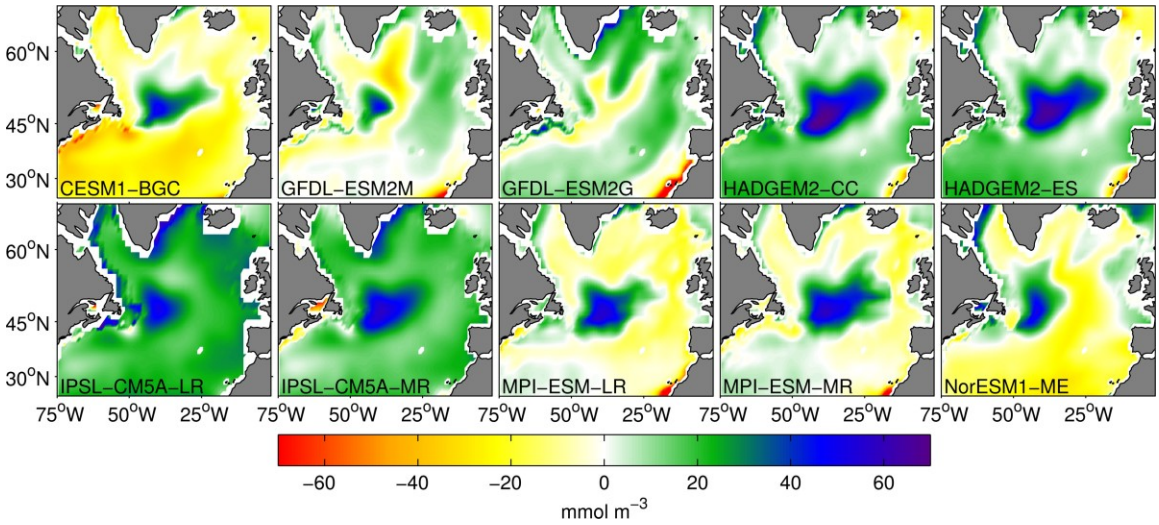

Figure 2. 3 Mean temperature (T) bias calculated as T-modeled – T-observed (from WOA09) over the period 1975-2005 depth averaged between 0 and 700 m.

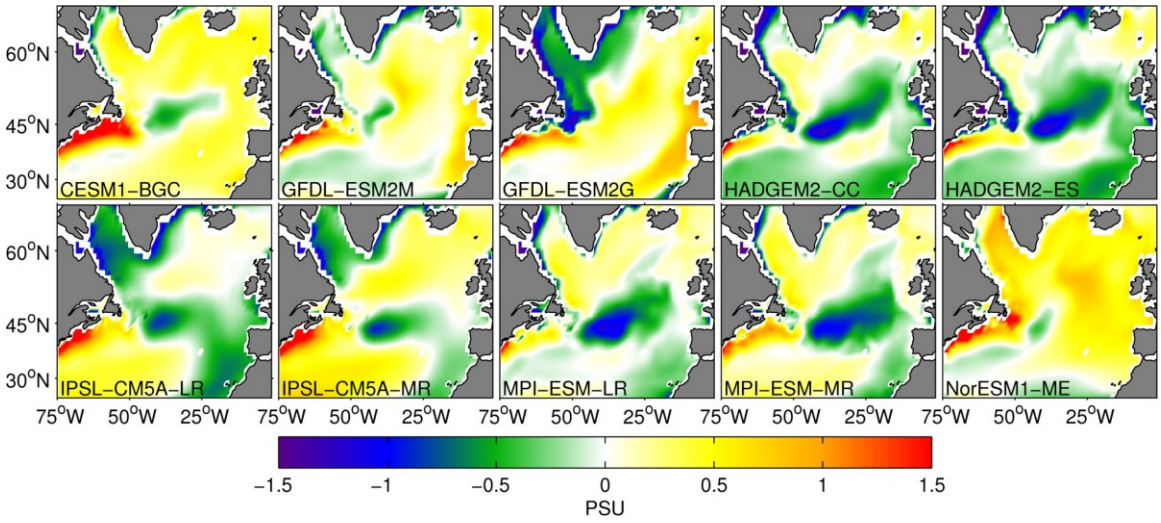

Figure 2. 4 Mean salinity (S) bias calculated as S-modeled – S-observed (from WOA09) over the period 1975-2005 depth averaged between 0 and 700 m.

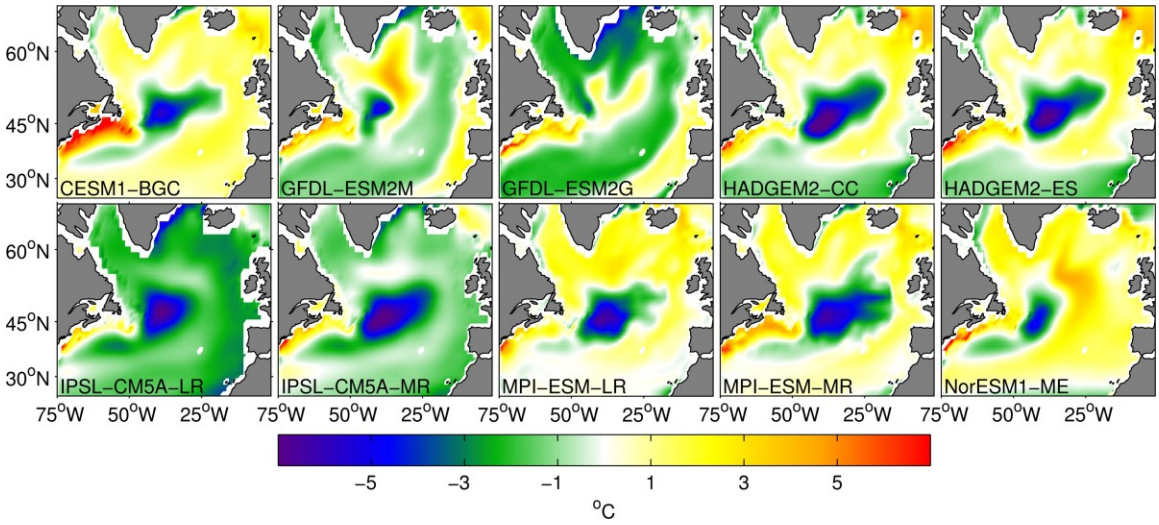

Figure 2. 5 Mean dissolved oxygen (O_2) bias calculated as O_2-modeled – O_2-observed (from WOA09) over the period 1975-2005 depth averaged between 0 and 700 m (notice the inverted colorbar).

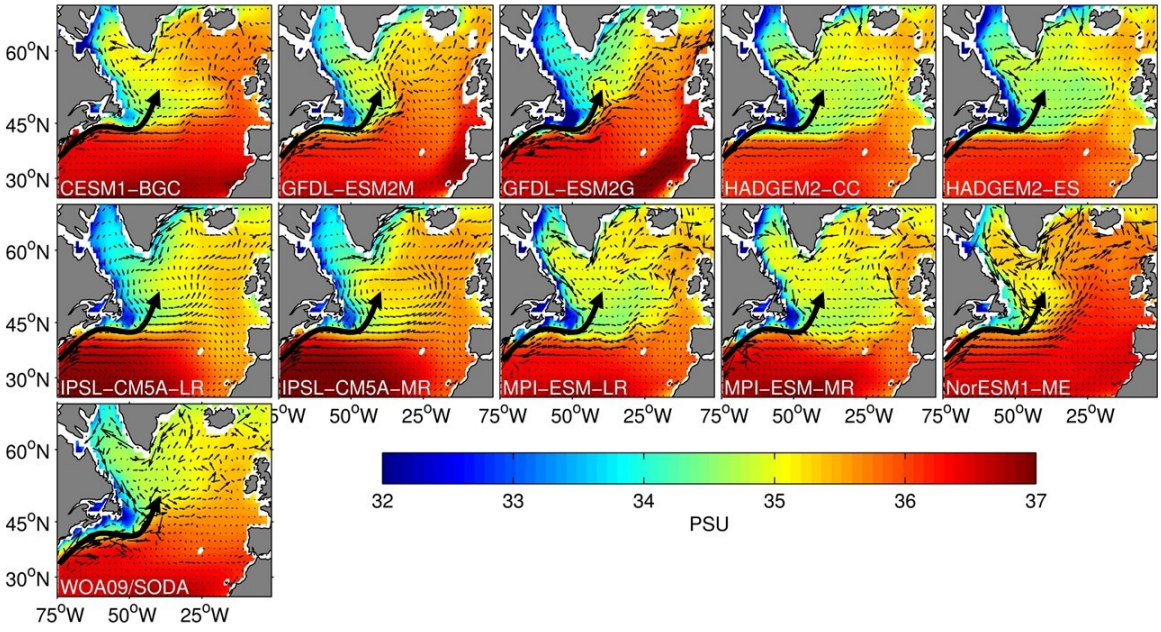

Figure 2. 6 Time-mean salinity S for the period 1975-2005, averaged over 0–700 meters, with superposed the depth-averaged velocity vectors for all the models and the observations (WOA09/SODA).The solid black arrow represents the observed pathway of the NAC, superimposed on the modeled circulation and salinity distribution.

The representation of the ocean circulation in the ESMs is indeed the key to explaining the model biases in T, S and O2 distributions. Figure 2.6 compares the climatological lateral circulation in the models and SODA 2.2.4 reanalysis, superimposed on the salinity distribution, both depth-averaged between the ocean surface and 700 m. The repeated solid black arrow represents the observed pathway of the NAC according to the SODA 2.2.4 product. The arrow follows the maxima in the depth integrated u, v fields and develops along the maximum salinity gradient. The superimposition over the individual model's circulation field (vectors) and salinity, clarifies the difference between models and observation. In agreement with the analysis in Danabasoglou et al. (2014), the North Atlantic Current (NAC) is more zonally oriented in the ESMs relative to the observations, and the Labrador Current extends further southeast and away from the shelf, carrying cold, fresh and highly oxygenated water into the central Subpolar North Atlantic (SPNA). The zonally-biased pathway of the NAC is also visible in the salinity distribution as the NAC separates the fresh subpolar waters from the salty subtropical ones. GFDL-ESM2M and GFDL-ESM2G better reproduce the NAC pathway, and as a result, the O2 distribution in those models matches more closely the observed climatology south of Greenland.

The modelled stratification for the period 1975-2005 is then compared with WOA in figure 2.7 and used to map the areas where deep convection occurs. Locations where the vertical density gradient $\Delta\sigma$ is less than 0.5 kg m-3 can be used as a proxy of modeled convective areas based on a comparison with winter (January-February-March) mixed-layer depth (MLD) performed on a subset of ESMs – six out of ten - for which monthly means of potential temperature and salinity are available over the historical period (not shown). It should be noted that when using a stratification criterion as a proxy for deep convection

the convective strength cannot be quantitatively compared between two convective regions for the same model or between different models. Also, the climatological stratification of the top 700 meters alone cannot inform us about the depth of convection or its seasonal cycle. No model, however, has mixed layer depth data available with monthly frequency after 2005.

With these caveats in mind, we compare the upper ocean stratification from each model to the WOA09 climatology. All CMIP5 models overestimate the stratification in the top 700 meters in comparison to the WOA09 data in both the subpolar and subtropical NA. In the SPNA, where deep convection takes place, the WOA09 climatology is weakly stratified, with $\Delta\sigma < 0.5\ kg\ m^{-3}$ over a broad region extending from the Labrador and Irminger Seas to Iceland and from 70oN to 50oN. In CESM1-BGC stratification with values as low as 0.5 kg m-3 can be found in the eastern subpolar region extending south to 50oN and along the western and eastern coast of Greenland. Both GFDL-ESM2M and GFDL-ESM2G display a weakly stratified region over the eastern SPNA, extending to 50oN. GFDL-ESM2M is weakly stratified also in the Labrador Sea, even if less so than WOA09, while GFDL-ESM2G does not appear to convect in the LS basin. The HadGEM2-CC and HadGEM2-ES provide the most stably stratified realizations and have similar vertical structure in the upper 700m. They both display their weakest stratification ($\sim 0.6\ kg\ m^{-3}$) in an area extending from the central LS to Iceland following the Greenland coast, and both have excess stratification biases ($\Delta\sigma > 0.9\ kgm^{-3}$) in the eastern side of the subpolar gyre compared to the other models and observations. Independently of resolution IPSL-CM5A show the lowest stratification ($\Delta\sigma < 0.5\ kg\ m^{-3}$) in the eastern SPNA. The weakly stratified region in IPSL-CM5A-MR extends further west compared to IPSL-CM5A-LR

but does not include the Labrador Sea interior. The lack of convective activity evidenced in figure 2.7 in the LS in both IPSL versions and GFDL-ESM2G is explained by the large fresh bias that characterizes these three models (figure 2.4). The MPI realizations show realistic patterns, but stratification is overall too strong compared to the observations. Both MPI-ESM versions show a distinct convective region in the LS, but the eastern SPNA is too stratified south of 60oN. NorESM1-ME is weakly stratified ($\Delta\sigma < 0.5\ kg\ m^{-3}$) over the SPNA region in a greater area than all other models.

Next, we examine the representation of dissolved O2 concentration averaged over the top 700 meters (Figure 2.8). There is broad agreement in the O2 distribution despite the known biases and inter-model differences in the representation of ventilation sites and the absence of distinguishable convection in the Labrador Sea for some of the realizations. Comparing figure 2.8 with figure 2.9, it is evident that the relatively high O2 in the western SPNA and the Labrador Sea primarily reflects the high solubility (O2sat) associated with the cold ocean temperature in those areas.

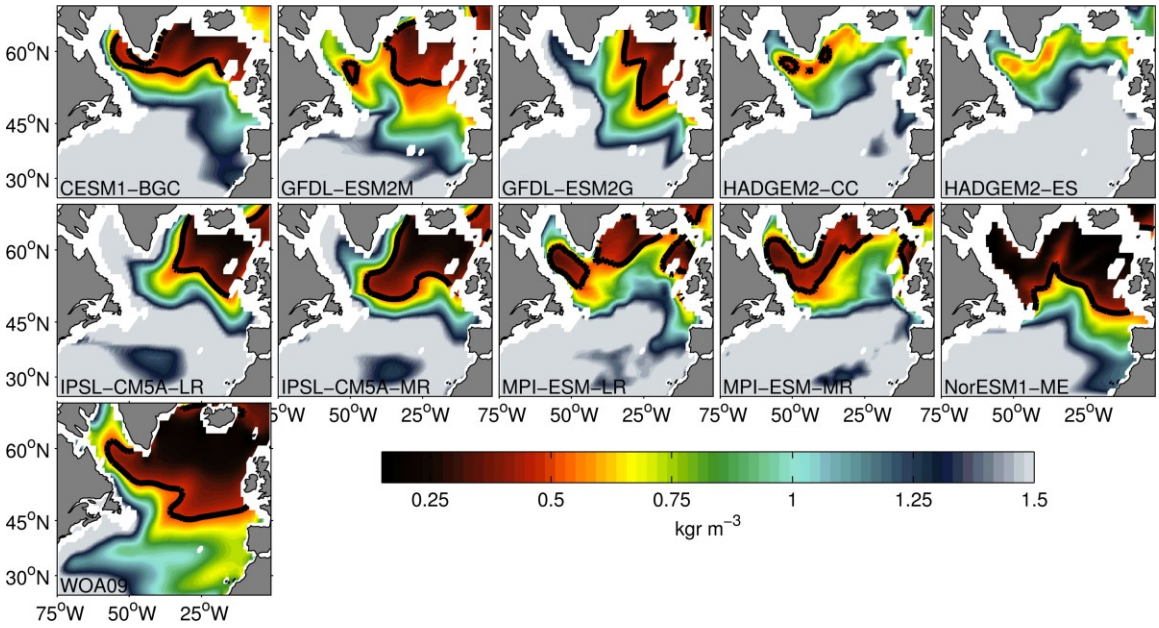

Figure 2. 7 Time-mean stratification for the period 1975-2005, averaged over 0–700 meters, defined as $\Delta\sigma = \sigma(700m) - \sigma(10m)$. The solid black contour encloses weakly stratified regions with $\Delta\sigma$ < 0.5 kg m^{-3}, as an approximation of regions impacted by convective activity or occupied by weakly stratified waters.

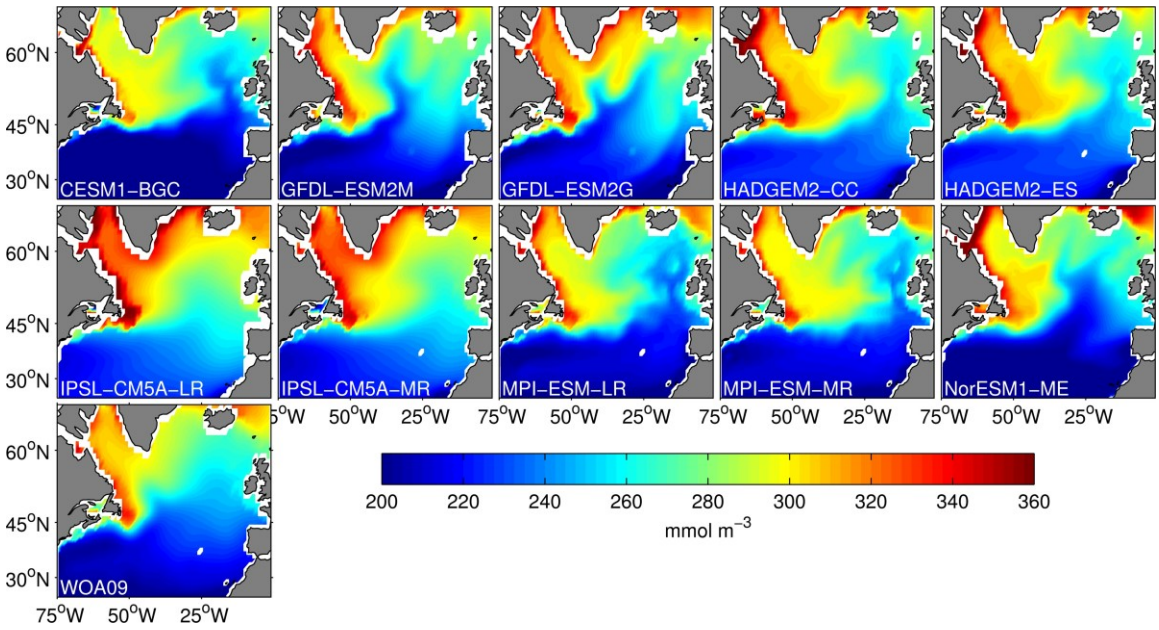

Figure 2. 8 Time-mean 1975-2005, 0–700 meters average, dissolved Oxygen.

Moving on to the AOU climatological distribution, it appears relatively homogeneous over the subtropical and subpolar region (~30 mmolm-3), with maximum values found along the east coast of North America (~60 mmolm-3) and off the shelf along the pathway of the NAC. Inter-model differences in AOU in the western SPNA and the Labrador Sea broadly match differences in stratification (figure 2.10). In the models, convection and deep water formation tend to decrease the regional AOU, while strongly stratified regions with a limited physical supply of O2 are characterized by a higher AOU. The majority of the models overestimate oxygen concentration in the subtropical region south of 48oN. CESM1-BGC and NorESM1-ME are the exceptions, underestimating dissolved oxygen values by 25-45 mmolm-3 (figure 2.8) south of 48oN. In both models the bias is due to a significant overestimation of AOU (figure 2.10), and values in excess of >40 mmol m-3 are found in the subtropics. Both CESM1-BGC and NorESM1-ME also exhibit a strong latitudinal gradient of AOU south of 48oN. In the remaining models, patterns are in generally good agreement with the observations and present a maximum in AOU that runs from the tropics along the Gulf Stream and extends further east following the inter-gyre boundary and the NAC. The elevated AOU values along the Gulf Stream and the NAC are associated with the transport of high-nutrient thermocline waters, figuratively termed as the "nutrient stream" (Palter, Lozier et al. 2005, Williams, Roussenov et al. 2006, Williams, McDonagh et al. 2011, Letscher, Primeau et al. 2016). All models but GFDL-ESM2M and GFDL-ESM2G underestimate AOU along the northern part of the nutrient stream as a result of the O2 overestimation, as shown in figure 2.5. The near-surface portion of the nutrient stream contributes significantly to the advective nutrient supply through induction across the tilted mixed layer base. Nutrient supply across the gyre margins is dominated by

lateral transport with vertical supply being secondary. As a result, the representation of the nutrient stream and associated high AOU is a crucial feature of the North Atlantic nutrient cycling.

GFDL-ESM2M and ESM2G reproduce the AOU pattern with values <40 mmol m-3 in the subtropical region and >50 mmol m-3 along the nutrient stream of the NAC. In the GFDL-ESM2G version the AOU is greater in the western subpolar region and in the LS (>45 mmol m-3), compared to GFDL-ESM2M and the rest of the models. This overestimation can be attributed to its stronger stratification (figure 2.7). In both versions of HadGEM the AOU values are lower than 18 mmolm-3 peaking along the NAC to values around 25 mmolm-3. Similarly, to HadGEM, IPSL-CM5A shows maximum AOU of about 40 mmolm-3 aligned with the NAC and lower values (<20 mmolm-3) north and south of it independently of resolution. In IPSL-CM5A-LR, AOU is elevated in the western SPNA and the LS compared to the MR version due to the relatively stronger stratification. Both versions of MPI-ESM-LR display AOU distributions enhanced along the NAC, with maximum values of about 40 mmolm-3, in good agreement with WOA data in the subtropics, and lower than observed in the SPNA.

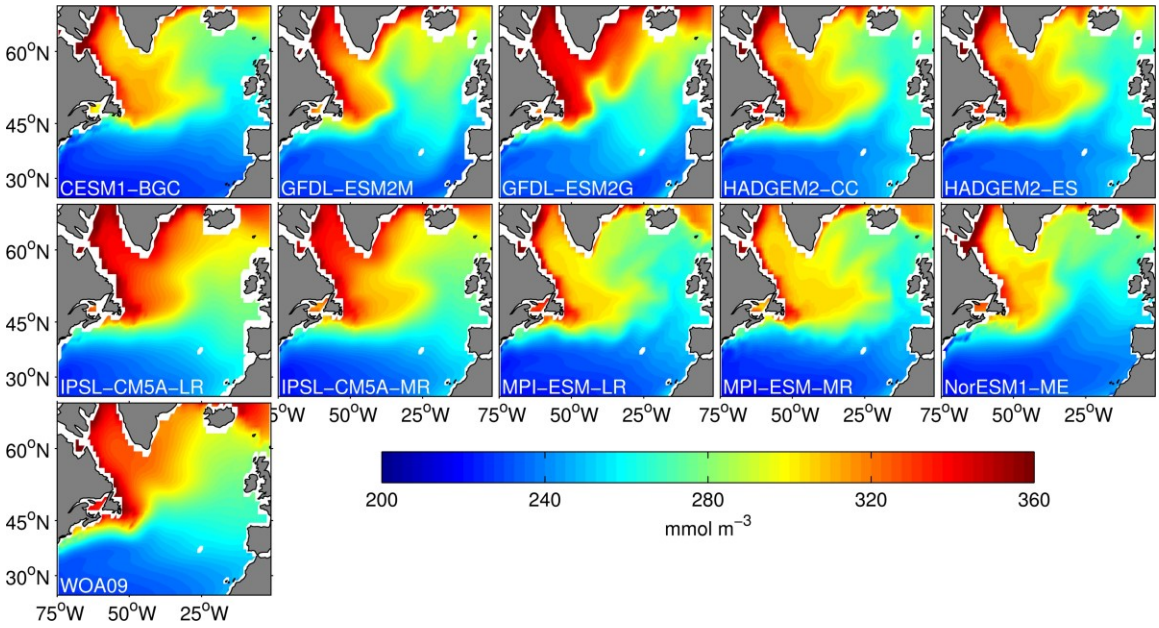

Figure 2. 9 Time-mean 1975-2005, 0–700 meters average of oxygen saturation.

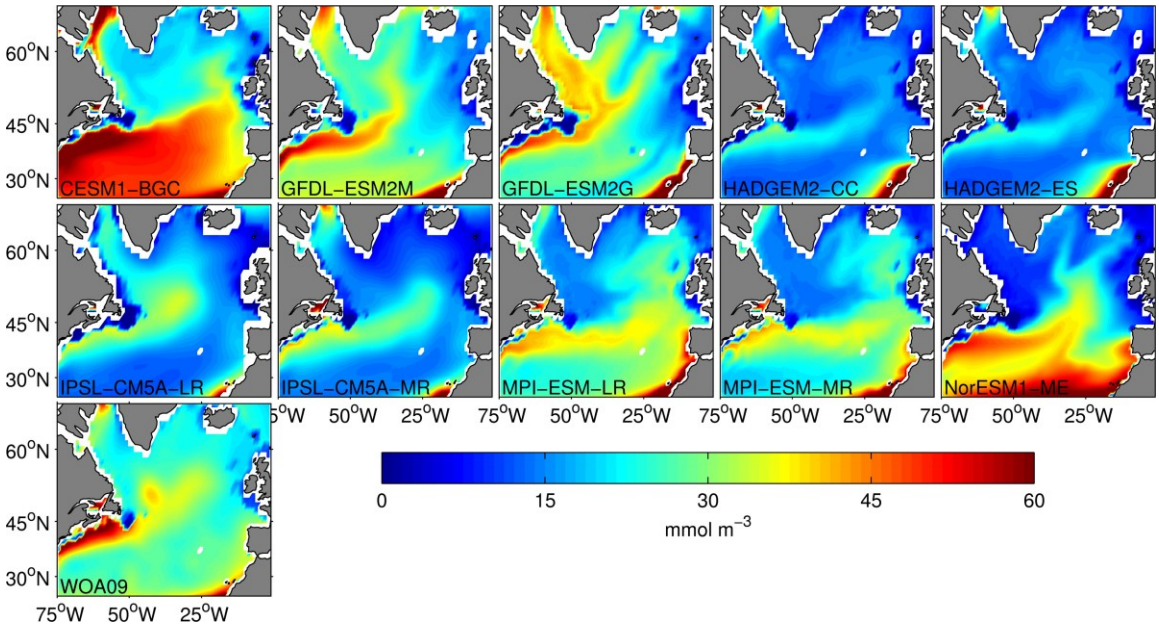

Figure 2. 10 Time-mean 1975-2005, 0–700 meters average of apparent oxygen utilization (AOU).

2.3.2 Spatial patterns of the centennial changes

We next examine the modelled centennial changes in the North Atlantic physical and biogeochemical variables. Centennial changes are quantified considering the differences between the 2070 - 2100 and 1975 - 2005 time averages. By using 30-year averages the impact of inter-annual to decadal variability on the projected centennial changes is mostly averaged out. Under the RCP8.5 scenario, the models predict on average warmer, fresher and more stratified waters in the SPNA. Temperature changes are shown in figure 2.11 and are bounded between 1 and 4 ºC except for a cooling patch stretching from Greenland to the south of Iceland depending on the model. The solid black contour in figure 2.11, connects points of zero change enclosing a cooling region, a feature known in the literature as the warming hole (Drijfhout, Oldenborgh et al. 2012, Rahmstorf, Box et al. 2015). AMOC reduction and reduced poleward heat transport have been suggested as a possible cause for such feature, but the processes behind the warming hole are not entirely understood. This feature plays an important role in simulted oxygen changes as we discuss later. Salinity changes are presented in figure 2.12. In all models salinity increases in the subtropics, partially offsetting the warming contribution on stratification. North of 45ºN the coastline surrounding the LS basin freshens in all models while freshening is also pronounced near the warming hole areas. The GFDL model shows the largest salinity decrease ($\Delta S<-1$) co-located with the warming hole, where stratification also reaches its maximum increases.

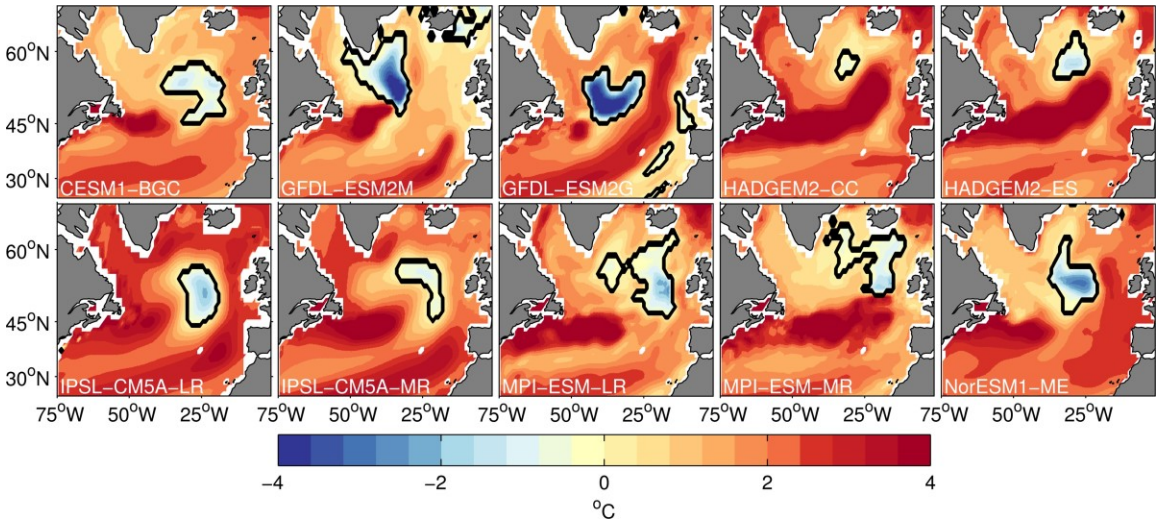

Figure 2. 11 Centennial change of T calculated as the difference in 30-year averages between (2070-2100) and (1975-2005). All plotted values are 0-700m averages. Solid black contour encloses 'warming hole'.

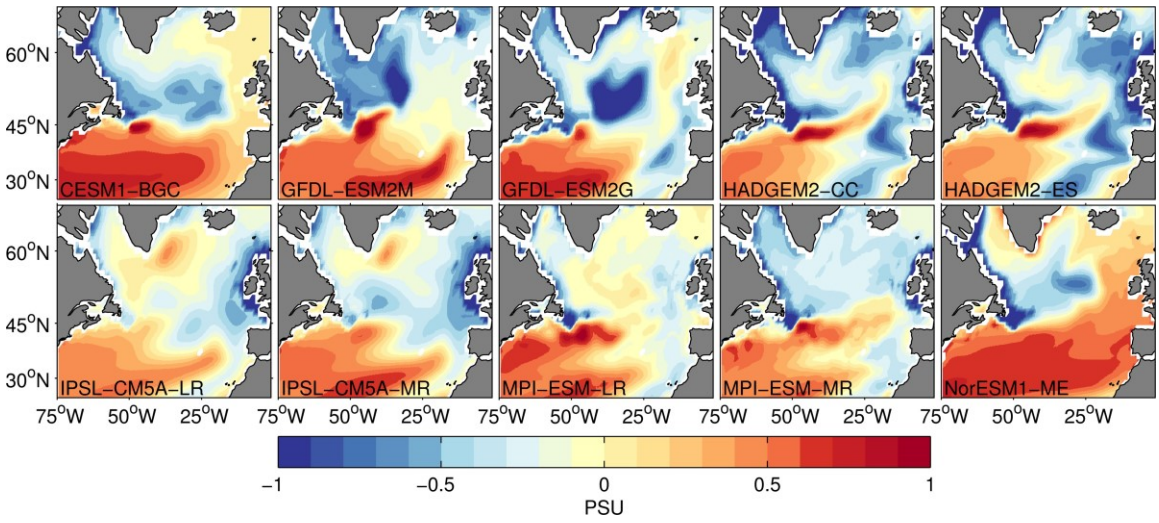

Figure 2. 12 Centennial change of S calculated as the difference in 30-year averages between (2070-2100) and (1975-2005). All plotted values are 0-700m averages.

All models but NorESM1-ME predict a more stratified future state of the ocean (figure 2.13) with spatially uneven changes as a result of uneven spatial warming and freshening (figure 2.11 and 2.12). NorESM1-ME displays compensation between temperature and salinity nearly everywhere in the NA. In the SPNA, salinity changes contribute the most in the projected stratification state (Fu, Randerson et al. 2015). CESM1-BGC, GFDL-ESM2M, and both MPI versions show stratification changes within the range of 0-1 kgm^{-3}, while for the remaining the change regionally exceeds 2 kgm^{-3}. In particular, both HADGEM and IPSL versions demonstrate their maximum increase along with their biased pathway of the NAC, and at eastern subtropical gyre, with values exceeding 1.5 kgm^{-3}. These zonally oriented changes in the vertical density structure result from the northward shift of the inter-gyre boundary, the warm and salty Gulf Stream extension and the NAC for those models, as revealed by the centenial changes of the kinetic energy (figure 2.18). The overall positive stratification change causes a suppression of the convective regions towards the eastern subpolar NA gyre. By the end of the 21st century, all models are strongly stratified in the LS and lack convection in the western part of SPNA (not shown).

The increasing temperature and stratification over this century have important implications for the oxygen budget. Firstly, the reduction of O_2 solubility can clearly be seen by comparing figure 2.11 with 2.15; the pattern of solubility change is indeed negatively correlated with that of temperature change. As expected the warming holes (marked by the solid black contours in figure 2.14) are characterized by strong regional solubility increase in all models (the warming hole effect), with the GFDL ESMs leading in both temperature decrease and O_2 increase. GFDL-ESM2G exhibits a strong warming hole and oxygen

increase even though it does not have a cold bias in the south of the Greenland over the historical period. While the cold bias in model climatology is still a concerning feature, the warming hole effect appears to be a robust response to greenhouse warming of all models analyzed in this study.

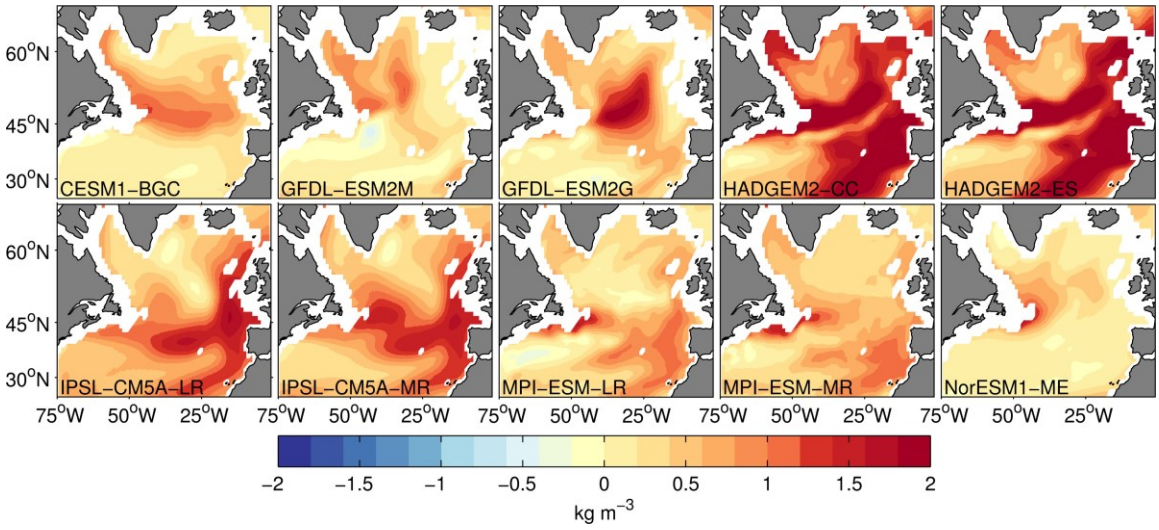

Figure 2. 13 Centennial change of stratification calculated as the difference in 30-year averages between (2070-2100) and (1975-2005). All plotted values are 0-700m averages.

Secondly, the suppression of convective mixing at high latitudes reduces the vertical O_2 transport, leading to an increase in AOU (figure 2.16) and a decrease in O_2 in the subpolar gyre in all models (figure 2.14). The quantitative relationship between AOU and stratification, however, varies among the models. CESM1-BGC and the two versions of the MPI models exhibit a large increase of stratification and AOU across the SPNA especially near the gyre boundary. The positions of maximum stratification (figure 2.13) and AOU increase (figure 2.16) are co-located in the two versions of GFDL and can be seen in the eastern part of the SPNA in the ESM2M version and in its central part in the ESM2G integration. The two versions of HADGEM2 have their maximum response in

both stratification and AOU in the southeastern part of the SPNA. In contrast, in the IPSL models, the locations of maximum AOU increase are decoupled from the regions of maximum stratification change, with the first occurring in the central/eastern part of the SPNA and the second in the southeastern part of the SPNA as in the HADGEM2 runs. Many processes may be responsible for the decoupling of AOU and stratification including the responses of lateral transport, ventilation and biological oxygen utilization to stratification changes. In the subtropics (<45ºN) the AOU responses differ across models, and those differences are reflected in the O_2 changes (figure 2.14). For O_2, and later for AOU, we also verified the statistical significance of the drift-corrected trends by testing if the average O_2 concentrations during 2070-2100 under the RCP8.5 scenario are significantly lower than those during 1975-2005 period relative to the interannual variability within each 30-year period. We used a t-test evaluating $t = \frac{-\{(\overline{x_{rcp8.5}}-\overline{x_{his}})-\Delta x_{piControl}}{\sigma\sqrt{\frac{1}{N_1}+\frac{1}{N_2}}}$ where σ is defined as $\sqrt{\frac{N_1 s_1^2+N_2 s_2^2}{N_1+N_2-2}}$, and the degree of freedom is d.f.=N_1+N_2-2 (d.f = 58 in our case). Preindustrial control simulations are used to correct for the model drift by subtracting their centennial changes.

In seven out of ten models significant AOU decrease is observed along the western boundary current and in its extension along the NAC (the nutrient stream effect). The solid black contour on figure 2.16 encloses the area of negative AOU change greater than the 150% of standard deviation of the negative values. The nutrient stream transports nutrient-enriched waters (high-AOU and low-oxygen) from low latitudes to subpolar region, which weakens in the warming ocean. AOU decreases in CESM1-BGC, in the two versions of GFDL-ESMs and, even if less uniformly, in the two versions of MPI-ESMs. Consequently,

in those models subtropical O_2 is resisting to deoxygenation despite the warming trend. In both versions of HADGEM2 and IPSL, on the other hand, AOU slightly increases.

Finally, biological productivity in the SPNA decreases in response to climate warming, likely due to the reduction in the vertical nutrient supply. In addition to the reduced convective mixing, a weakened AMOC may also slow down the nutrient stream of the Gulf Stream and NAC. This could potentially result in weakened export production and reduced biological consumption of subsurface O_2. The effect of biological productivity will not affect the solubility, and its impact only appears through the AOU changes. The centennial changes of AOU, therefore, reflect combined effects of convection and circulation changes, and biological oxygen consumption. A close examination of the modeled export production reveals that little agreement exists in both pattern and signs across models (figure 2.17). In CESM1-BGC export production decreases over the SPNA. In the two versions of IPSL and in NorESM1-ME export production increases in the warming hole and decreases outside. The other models show a mix of moderate increase and decrease in the SPNA, and all project a decrease in export production in the eastern subtropics. Despite these inter-model differences, centennial AOU is projected to increase in the SPNA in all models, suggesting that physical processes are playing the dominant role.

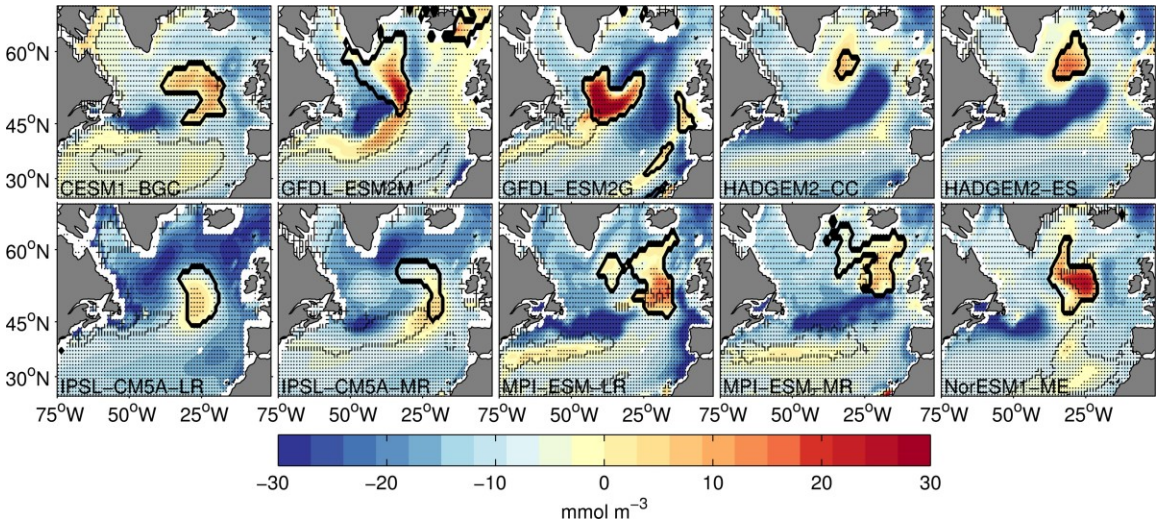

Figure 2. 14 Centennial change of dissolved oxygen calculated as the difference in 30-year averages between (2070-2100) and (1975-2005). All plotted values are 0-700m averages. Solid black contours enclose 'warming holes' while dashed contours highlight subtropical AOU decrease exceeding 1.5 times the standard deviation of negative values. Black dots indicate areas where the results are statistically significant at the 99% confidence level according to a t-test.

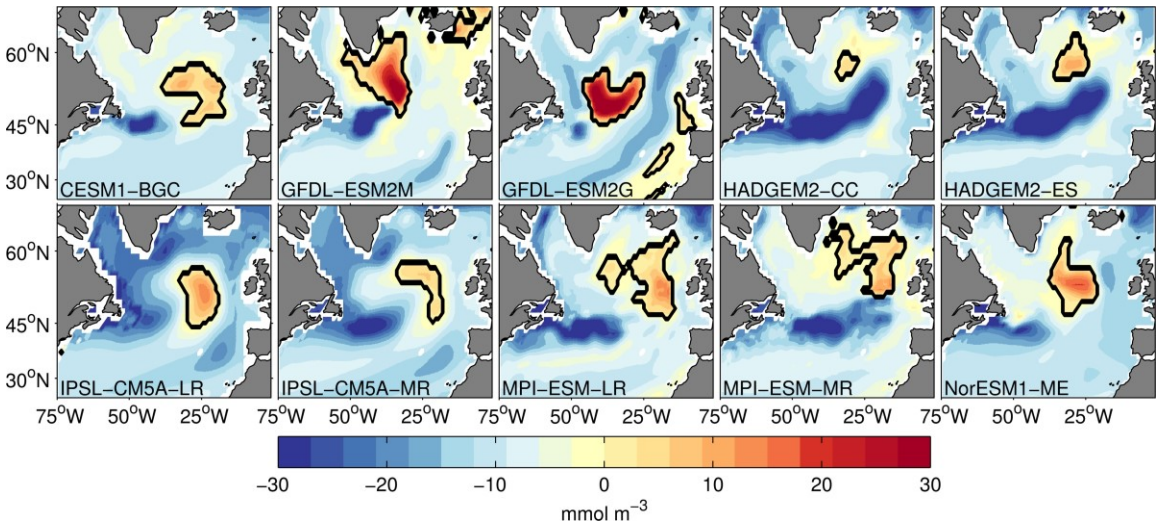

Figure 2. 15 Centennial change of oxygen saturation calculated as the difference in 30-year averages between (2070-2100) and (1975-2005). All plotted values are 0-700m averages.

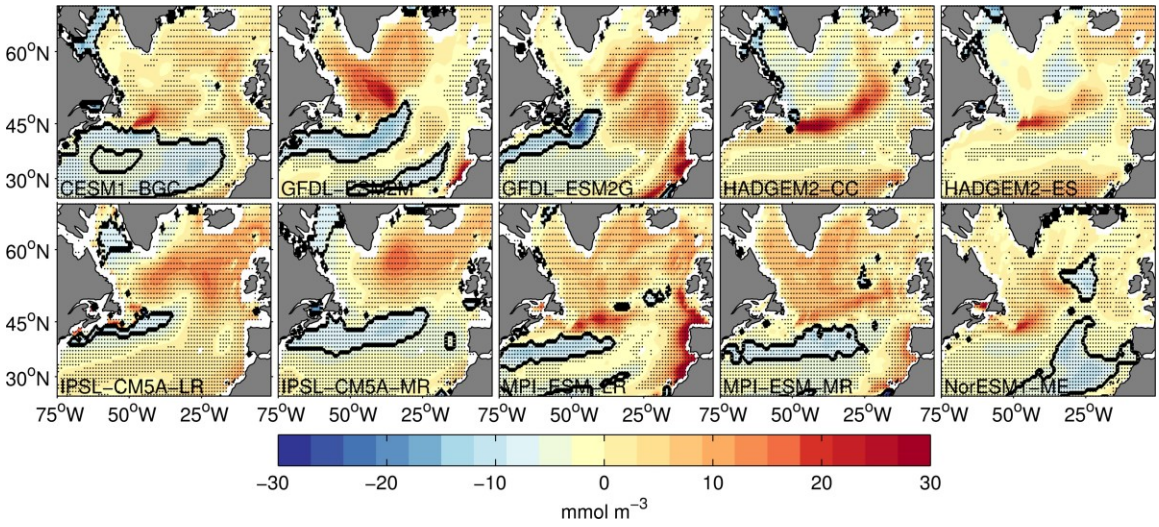

Figure 2. 16 Centennial change of apparent oxygen utilization (AOU) calculated as the difference in 30-year averages between (2070-2100) and (1975-2005). All plotted values are 0-700m averages. Solid black contours enclose areas where the AOU decrease exceeds 1.5 times the standard deviation of negative values. Black dots indicate areas where the results are statistically significant at the 99% confidence level according to a t-test.

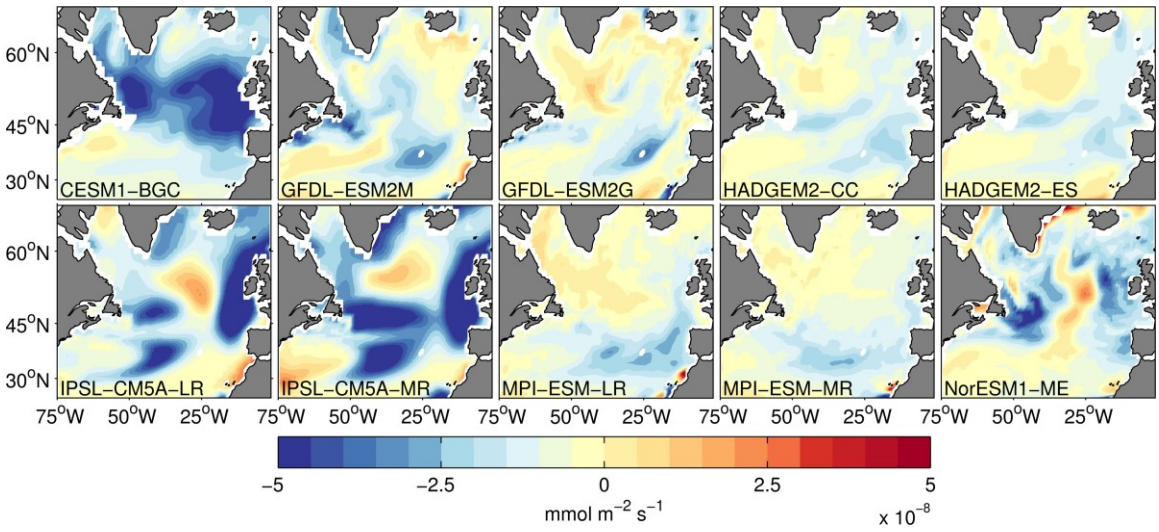

Figure 2. 17 Centennial change of export production at 100m depth (EP) calculated as the difference in 30-year averages between (2070-2100) and (1975-2005). The export production is expressed as the downward flux of organic carbon. All plotted values are 0-700m averages.

The combination of the three processes outlined above explains the complex, patchy patterns of O_2 changes (figure 2.14), and of the significant differences among models. Our analysis points to two major mechanisms; the thermally-driven solubility trend and the change in convective activity due to the increased stratification. Some of the model-model differences can be attributed to the different representation of the warming hole and its impact on the $\Delta O_{2,\,sat}$ field. The Δ(AOU) field also display complex, variable across models, patterns. The stratification change can explain the AOU increase in the SPNA only, in particular in the southeast of Greenland and between Iceland-Scotland, however, all models but the HADGEM2 exhibit also a significant AOU decrease near the gyre boundary around 45ºN, near the NAC. The AOU reduction in the vicinity of NAC occurs in all models except for the two versions of HADGEM2.

Figure 2.18 examines the centennial change of the mean kinetic energy (KE) in the North Atlantic. The centennial change of the KE reveals a substantial weakening of the major currents. In CESM1-BGC the NAC as well as the cyclonic circulation of the subpolar gyre weaken considerably. Both versions of GFDL show weakening of the NAC intensity without significant changes in the LS circulation. HADGEM versions show changes similar to CESM1, with weakening of the cyclonic circulation in the LS and weakening of the NAC. Increase in KE is also observed as a result of a northward shift of the NAC pathway. Such northward shift explains the zonal increase in stratification in the HADGEM model (figure 2.13) as a result of warmer and lighter waters penetrating further north in the subpolar gyre at latitudes greater than 45ºN. Weakening and northward shift of the NAC is also observed in the MPI runs, but without intruding far into the subpolar gyre as in

HADGEM. Both version of IPSL-CM5A project a weakening of the NAC but not as intense as in the other models.

In figure 2.18 the solid contours of the "warming holes" reveal that these patchy features in the SPNA result from the slowdown of the NAC that characterizes all models and extend from the surface to 700 m and below. Around 45ºN NAC changes coincides with the strongest AOU decrease, defined by the dashed contours in the subtropical region 30ºN-47ºN. The nutrient stream through which nutrient-enriched and oxygen-depleted waters are transported from low latitudes to the subtropical and subpolar region is therefore greatly reduced in a warming ocean.

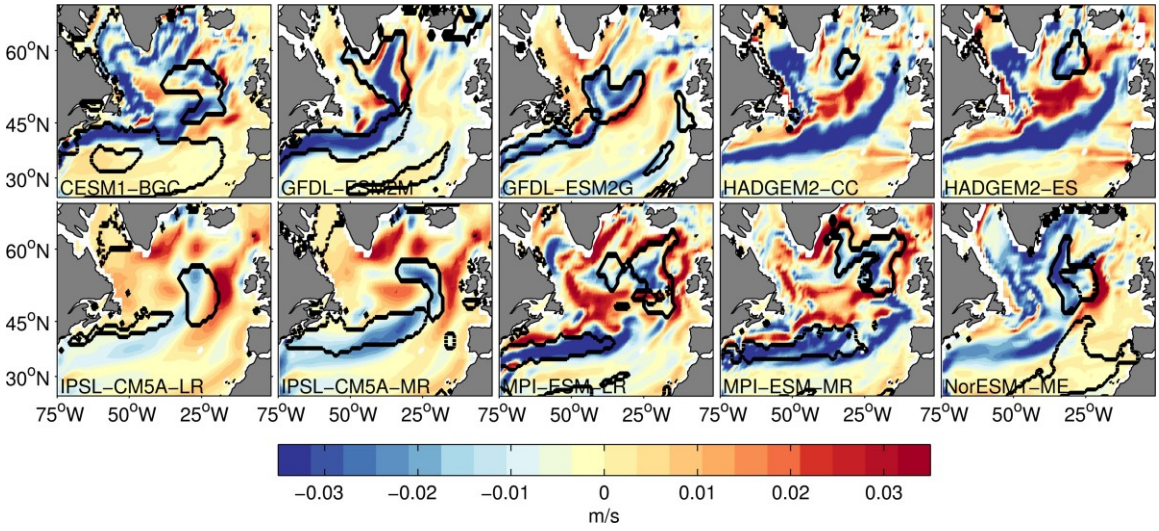

Figure 2. 18 Centennial change of KE (cast as a speed $V_{KE} = (\sqrt{u^2 + v^2})$) calculated as the difference in 30-year averages between (2070-2100) and (1975-2005). All plotted values are 0-700m averages. Solid contours enclose the warming holes as defined by temperature changes, and dashed contours enclose areas where AOU decrease exceeds 1.5 times the standard deviation of negative ΔAOU values.

Overall, CMIP5 ESMs display several common features in projecting the centennial-scale deoxygenation of the North Atlantic towards the end of our century. All models predict that O_2 will decrease in the subpolar region as a consequence of warming and weakened convection. Thermally-driven O_{2sat} decrease and stratification-driven AOU increase will reinforce one another at subpolar latitudes. However, the projected O_2 change is not uniform in space but exhibits rather complex spatial structures. Most models exhibit strong warming near the southern boundary of the subpolar gyre (~50^{o}N) and a strong decline of O_{2sat} there. The only patches of increasing O_2 in the subpolar regions are associated with the warming holes. At the intergyre boundary (~45^{o}N), the magnitude of deoxygenation is reduced in all models. In about half of those we examined O_2 moderately increases along the NAC pathway. The resistance to deoxygenation is primarily due to the reduction of AOU associated with the weakened lateral transport of AOU associated with the nutrient stream. In the subtropics (<40^{o}N), about half of the models predict that O_2 will regionally increase and the other half predicts that O_2 will decrease, depending on the sign of the AOU changes.

2.4 Conclusions and Discussion

We analyzed nine ESMs from the CMIP5 catalog with various physical climate models and marine biogeochemical modules of different complexity with the goal of understanding projected dissolved oxygen changes. The ability to properly represent the North Atlantic convective regions during the historical period varies among models. For example, three of them show little to no ventilation in the Labrador Sea, and all but two models display a significant bias in the representation of the position and strength of the NAC such that the Labrador Current delivers colder, fresher and more oxygenated waters further southeast

compared to observations. Under the RCP8.5 scenario in all models the mean ocean temperature in the upper 700 m of the North Atlantic (22ºN-73ºN) increases by 2-4ºC by the end of the 21st century, stratification also increases and dissolved oxygen concentrations decrease by 10-20 $mmolm^{-3}$. Trends in salinity and AOU, on the other hand, vary among models and between the subpolar and subtropical NA, broadly defined as north and south of 45º. These basin-scale analyses are consistent with the previous analyses of multi-model averages (Bopp, Resplandy et al. 2013, Cocco, Joos et al. 2013) generally following the ocean deoxygeneation hypothesis where anthropogenic warming of upper ocean leads to a decrease in the solubility of oxygen and a weakened vertical exchange due to an increased stratification.

New and unique findings of this study are the mechanisms of projected increase in the dissolved oxygen concentrations in limited areas, generally found to the south of Greenland. The existence of these patches of oxygenated waters is associated with the projected weakening of the NAC, while their locations are model-dependent due to the varied representation of the NAC pathway. This feature was not discussed in earlier studies based on multi-model averages because the patterns of oxygen change are highly model-dependent, and its signal can be obscured if averaged across many different models. However, this feature is caused by a few common mechanisms in all models. In particular, the weakening of the NAC has two distinct impacts on the projected changes in dissolved oxygen. First, reduced northward heat transport results in the models simulating a cold temperature anomaly in the SPNA causing a locally high oxygen concentration (the *warming hole* effect). The two versions of GFDL-ESMs are the only members in the subset considered that capture the northeastward direction of NAC in the historical runs, and

project the *warming hole* located south of Greenland, centered at about 50° N and 45°W. The rest of the models with a strongly zonal NAC, project the *hole* towards the eastern SPNA at about 50°N and between 45°W and 15°W. Those localized negative temperature changes induce a thermodynamically driven increase in dissolved oxygen as the oxygen saturation responds to temperature. Secondly, reduced northward mass transport results in the AOU decrease along the pathway of the Gulf Stream extension and the NAC. The weakened advection results in the oxygen increase along its pathway because of the reduced transport of low-oxygen/high nutrient waters from the low latitudes (the *nutrient stream* effect). Furthermore, the shift in the position of NAC causes localized, strong oxygen changes associated with the shifts in the boundaries of water masses. These localized mechanisms are operating in addition to the effects of basin-scale warming and stratification increase.

While there are differences in the detailed patterns of O_2 trend, the all ESMs agree that the basin-scale changes are primarily determined by the decline in oxygen saturation. The changes in AOU can modulate the signal but are not the determining factor for the basin-scale O_2 inventory. Despite the fact that AOU is expected to increase as a result of a more stratified ocean mean state, the changes in the circulation result in a reduction of AOU in the subtropics, leading to a relatively small change in the basin-scale AOU inventory. South of 45°N, AOU decreases for the majority of the models by 5-20 $mmolm^{-3}$. The weakening of the NAC causes a reduction in the lateral and vertical transport of nutrients capable of reaching the mixed layer and this in turn results in a lower biologically-driven O_2 consumption. These changes are likely explanations of the decline in the regional AOU. The western subtropical Atlantic is particularly resisting to the warming induced

deoxygenation. This behavior in the subtropics is common in half of the models, suggesting a potentially important, coupled physical-biogeochemical resistance to the ocean deoxygenation in global warming scenarios. In the future research, it will also be important to determine how circulation and stratification may change whenever eddies and mesoscale variability are properly accounted for instead of simply parameterized.

In this work we pinpointed both similarities and differences across ESM model runs. The results presented here should be interpreted keeping in mind that at least three sources of uncertainties affect the projections of ecosystem stressors (Hawkins and Sutton 2009): the models' internal variability and its potential to change over long timescales (internal variability uncertainty); the different physical and biogeochemical modules and their parameterizations (model uncertainty); and the uncertainty in future emissions of greenhouse gases (scenario uncertainty). [Frolicher, 2016] has shown that over centennial scales, as considered in this work, model uncertainty dominates for sea surface temperature over the subpolar North Atlantic and for O_2 over lower latitudes.

If global warming and resultant ocean heat uptake continues unabated, the O_2 saturation of the North Atlantic basin will decrease significantly in this and coming centuries. While more work is clearly needed to assess the importance of model biases in the representation of deep convection and mean currents in the future projections, our results show that the continuing warming of the SPNA will have far-reaching influence on the regional deoxygenation that will spread across other regions on the centennial timescale. Therefore, it is crucial to continue and increase data coverage of the oxygen sampling in addition to temperature and salinity so that the scientific community can better inform the public and policy makers about the progression and the potential risks of ocean deoxygenation. In this

regard, further development of autonomous sensors such as Bio-Argo can provide valuable observing platform for the long-term oxygen trends.

CHAPTER 3. MODULATION OF THE NORTH ATLANTIC DEOXYGENATION BY THE SLOWDOWN OF THE NUTRIENT STREAM

Published as

Tagklis, F., Ito, T., Bracco, A., (2020) Modulation of the North Atlantic deoxygenation by the slowdown of the nutrient stream. Biogeosciences, 17, 231–244, https://doi.org/10.5194/bg-17-231-2020, 2020

Abstract

Western boundary currents act as transport pathways for nutrient-rich waters from low to high latitudes (nutrient streams) and are responsible for maintaining mid- and high-latitude productivity in the North Atlantic and North Pacific. This study investigates the centennial oxygen (O_2) and nutrient changes over the Northern Hemisphere in the context of the projected warming and general weakening of the Atlantic Meridional Overturning Circulation (AMOC) in a subset of Earth System Models included in the CMIP5 catalogue. In all models examined, the Atlantic warms faster than the Pacific Ocean, resulting in a greater basin-scale solubility decrease. However, this thermodynamic tendency is compensated by changes in the biologically-driven O_2 consumption which dominates the overall O_2 budget. These changes are linked to the slow-down of the nutrient stream in this basin, in response to the AMOC weakening. The North Atlantic resists the warming-induced deoxygenation due to the weakened biological carbon export and remineralization, leading to higher O_2 levels. On the contrary, the projected nutrient stream and macro-nutrient inventory in the North Pacific remain nearly unchanged.

3.1 Introduction

Deoxygenation of the oceans is potentially one of the most severe ecosystem stressors resulting from global warming given the high sensitivity of dissolved oxygen to ocean temperatures. Unrestrained anthropogenic CO_2 emissions and consequent warming are likely to disrupt marine habitats and influence the cycles of biogeochemically essential elements (Gruber 2011). Global-scale deoxygenation has taken place during the second half of the 20th century (Stramma, Johnson et al. 2008), and a widespread recognisable signal of O_2 decline is emerging beyond the envelope of natural variability (Ito, Minobe et al. 2017, Schmidtko, Stramma et al. 2017). The Earth Systems Models (EaSMs) included in the CMIP5 (Coupled Model Intercomparison Project – Phase 5) catalog project a robust (across models) decline in dissolved O_2 inventory for the 21st century despite differences in models' complexity, biogeochemical parameterizations and warming responses. Under the "business as usual" scenario, all models predict enhanced hypoxic conditions and dissolved oxygen loss (Bopp, Resplandy et al. 2013, Cocco, Joos et al. 2013).

The dissolved oxygen is controlled by air-sea exchange, circulation, and biology, and the dissolved oxygen concentrations in the interior ocean reflect a balance between ventilation, circulation and biological consumption. Warming climate can cause shifts in this balance. The solubility of dissolved oxygen is inversely proportional to seawater temperature, and air-sea O_2 exchange is a relatively fast process in the ice-free open ocean, of the order of O(20 days) (Broecker and Peng 1974, Wanninkhof 1992). All else unchanged, in a warming climate there would be a corresponding O_2 decline closely following the temperature-solubility relationship of seawater (Najjar and Keeling 1997). However, changes in ocean stratification, ventilation and biological productivity can further change

dissolved oxygen. During the transient trajectory of the climate system as it adjusts to anthropogenic forcing, near-surface waters warm faster than deeper waters, leading to an increase in ocean stratification. In a more stratified ocean, the ventilation of sub-surface waters diminishes, reducing the O_2 supply to the ocean interior (Bopp, Le Quéré et al. 2002, Frölicher, Joos et al. 2009). Furthermore, increased stratification is expected to weaken the meridional overturning circulation and therefore the ventilation of the waters deeper than 1000 m (Meehl and Stocker 2007). At the same time, the weakening of the overturning circulation may decrease the overall vertical mixing and therefore the supply of nutrient-rich waters to the euphotic layer, thus causing a reduction in biological productivity and carbon export. As upwelling becomes less effective in uplifting nutrient-rich waters, export production of organic material and oxygen consumption through respiration also diminishes, but as water parcels spend more time in the ocean interior, the oxygen consumption integrated over time may increase (Rykaczewski and Dunne 2010).

Western Boundary Currents (WBCs) plays an essential role in biogeochemical cycling. In the northern hemisphere, WBCs represent an advection pathway for nutrients from the ocean boundaries into the open waters. They are known as “nutrient streams” and are responsible for maintaining basin-scale high productivity in the mid- and high-latitudes over interannual and longer timescales (Palter, Lozier et al. 2005, Williams, Roussenov et al. 2006, Williams, McDonagh et al. 2011, Letscher, Primeau et al. 2016). High nutrient concentrations extend from tropical coastal areas into the interior of the Pacific and Atlantic Oceans, following the Kuroshio Current and the Gulf Stream (Pelegrí and Csanady 1991). From a dynamical perspective, recent studies have shown that the nutrient supply due to the lateral transport in the subtropical euphotic zone dominates over the vertical transport

(Letscher, Primeau et al. 2016), with mean and eddy horizontal cross-boundary nutrient transport accounting for ~75% of the total nutrient supply into the subtropical gyres (Yamamoto, Palter et al. 2018). Therefore, changes in this horizontal nutrient transport, through changes in the WBC characteristics, can have a profound influence on the basin-scale biogeochemical cycling.

The primary objective of this study is to investigate how and why the dissolved oxygen content of the North Atlantic and the North Pacific basins is projected to change in the 21st century using a suite of EaSM integrations. In particular, we aim at understanding and quantifying the role of the nutrient streams in the centennial scale deoxygenation and nutrient loading of these two basins. We first verify the EaSMs' skill in reproducing the mean state of relevant biogeochemical variables and then analyze the model projections to the end of the 21st century.

3.2 Data and Methods

For this study, we analyse seven CMIP5 EaSMs for which the variables of interest are available. The suite includes two versions of the Geophysical Fluid Dynamics Laboratory (GFDL) Earth System Model, GFDL-ESM2G and GFDL-EASM-2M (Dunne, John et al. 2012, Dunne, John et al. 2013), the Community Earth System Model, CESM1-BGC (Long, Lindsay et al. 2013, Moore, Lindsay et al. 2013, Moore, Lindsay et al. 2013), two versions of the Institute Pierre Simon Laplace model, IPSL-CM5A-LR and IPSL-CM5A-MR (Dufresne, Foujols et al. 2013), and two of the Max Plank Institute model, MPI-ESM-LR and MPI-ESM-MR(Giorgetta, Jungclaus et al. 2013, Giorgetta, Jungclaus et al. 2013). The EaSMs vary regarding the parameterisations of the ocean circulation and

biogeochemical modules, but the biogeochemical component in all cases is formulated as Nutrient-Phytoplankton-Zooplankton-Detritus (NPZD) type. For each member, we examine the last 30 years (1970-2000) of the twentieth century in the historical simulations and the last 30 years (2070-2100) of the twenty-first century under the future projections based on the Representative Concentration Pathway 8.5 scenario or "rcp8.5" (Riahi, Rao et al. 2011, Riahi, Rao et al. 2011, Taylor, Stouffer et al. 2012).

All the variables used in the CMIP5 analysis are three-dimensional and annually averaged fields interpolated onto a common 1° x 1° longitude-latitude grid domain and 33 depth levels, consistent with the World Ocean Atlas. The interpolation method applied was bilinear using the Climate Data Operators (Schulzweida 2019). The variables of interest are dissolved oxygen (O_2), temperature (T), phosphate (PO_4), particulate organic carbon export at 100m depth (EP) and current speed (CS = $V_{CS} = (\sqrt{u^2 + v^2})$) in units of meters per second. Oxygen solubility ($O_{2,sat}$) is calculated from potential temperature and salinity following Garcia and Gordon (1992*).* Apparent oxygen utilisation (AOU) is then determined as the difference between the $O_{2,sat}$ and O_2 (AOU= $O_{2,sat}$ - O_2). AOU changes quantify contributions from processes other than warming, such as remineralisation of organic matter and/or the rate of transport and mixing of water mass (Sarmiento and Gruber 2006). The separation of oxygen changes ΔO_2 into a biologically/transport-driven component, Δ(AOU), and a thermodynamically-driven component, $\Delta O_{2,sat}$, is based on the assumption that the surface oxygen is always in equilibrium with the overlying atmosphere. However, intense air-sea interactions during wintertime at the high latitudes often cause under-saturated surface O_2, leading to a non-negligible preformed AOU (Ito, Follows et al.

2004). Unfortunately, stored variables in the model outputs do not allow a more precise estimation.

It has been shown that in the CMIP5-EaSMs the biogeochemical tracers are not always equilibrated with respect to the ocean circulation. To account for the magnitude and sign of this model drift, in all analyses we used the pre-Industrial Control simulations (piControl) and removed the drift by defining, for example, $O_{2_{trend}} = \left\{O_2^{rcp8.5(B)} - O_2^{hist(A)}\right\} - \left\{O_2^{piControl\,(B)} - O_2^{piControl\,(A)}\right\}$ where A and B indicate the periods 1970-2000 and 2070-2100.

3.3 Results

3.3.1 Model Evaluation

We first evaluate the model representation of the distributions of key biogeochemical variables, including PO_4, O_2 and AOU. We focus on the Northen Hemisphere (10ºN-65ºN) and concentrate on the upper layer of the ocean (depth range 0-700 m). The CMIP5 climatological values are calculated over the period 1970-2000 in the "esmHistorical" experiments. Annual mean climatologies from the World Ocean Atlas 2009 (WOA09) (Antonov, D. Seidov et al. 2010, Garcia, R. A. Locarnini et al. 2010, Locarnini, A. V. Mishonov et al. 2010) are used as an observational reference. Note that in Figures 3.1-3.3 the Pacific and Atlantic basins are plotted in separate panels with different color scales because of the large differences in their mean values.

The observed PO_4 concentrations **[Figure** 3.**1]** range from ~0.8μM in the subtropical North Pacific (STNP) gyre to values greater than 2.7μM in the subpolar North Pacific (SPNP)

gyre and the eastern boundary and equatorial upwelling region at the lower latitudes. The EaSM are broadly in agreement over the North Pacific regarding the PO_4 spatial gradients, with the exception of CESM1-BGC that underestimates the latitudinal differences with higher nutrient levels overall. In all models, there is a slight underestimation of PO_4 in the subpolar region, that is reflected in the multi-model mean (MMM) where values are about ~0.3μM smaller than in the WOA09. In the North Atlantic, the observed concentrations range from ~ 0.2μM in the subtropical (STNA) gyre to ~1.15μM in the subpolar (SPNA) gyre. In contrast to the Pacific ocean, there are significant model-to-model differences in the PO_4 spatial pattern. All models but IPSL-CM5A-LR overestimate the concentrations of PO_4, with CESM1-BGC displaying the largest bias, followed by GFDL-ESM2M.

The simulated pattern of dissolved oxygen is better captured than PO_4 by each model individually and therefore by the MMM, especially in the Atlantic basin. In the Pacific ocean, the observed dissolved oxygen concentrations range from ~160μM in the STNP gyre to ~50μM in the SPNP gyre. GFDL-ESM2M, IPSL-CM5A-LR and IPSL-CM5A-MR overestimate dissolved oxygen in the STNP by ~35μM and CESM1-BGC and MPI-ESM-MR underestimate oxygen concentration in the same area. The end result is a MMM that compares relatively well to WOA09 due to the compensating biases. In the North Atlantic the concentrations of dissolved oxygen range from ~180μM in the STNA gyre to ~340μM in the western SPNA and ventilation sites. The latitudinal gradient reflects both the temperature gradient and the presence of well-mixed and ventilated cold subpolar waters.

In terms of AOU, the CMIP5-ESMs integrations capture the observed climatological distribution with more robust (across models) patterns in the Atlantic region [Figure 3.3]. In the Pacific Ocean, the AOU concentrations range from ~30μM in the STNP gyre to

~250μM in the SPNP gyre. The overall higher values of AOU in the Pacific compared to the Atlantic basin are due to the older age of the waters and the limited physical O_2 supply to intermediate and deep waters. In the Atlantic Ocean, low AOU values are found in the SPNA as convection and deep water formation decrease the AOU in this region. The narrow band of higher AOU values around ~60μM that extends from the tropics to the east into the basin following the Gulf Stream and the North Atlantic Current (NAC) pathway is captured by all models with different intensity, and is present in the MMM, even if slightly weaker than observed due to biases in the representation of the Gulf Stream separation and NAC location. The skill of each model in capturing the mean nutrient concentration **[Figure** 3.**1]** is also reflected in the intensity of AOU **[Figure** 3.**3].** For example, CESM1-BGC as the one extreme in the North Atlantic, overestimating (>1.2μM) the nutrient concentration, shows the highest (>70μM) AOU values, while both IPSL versions underestimate the nutrient concentrations and show low AOU values (<70μM).

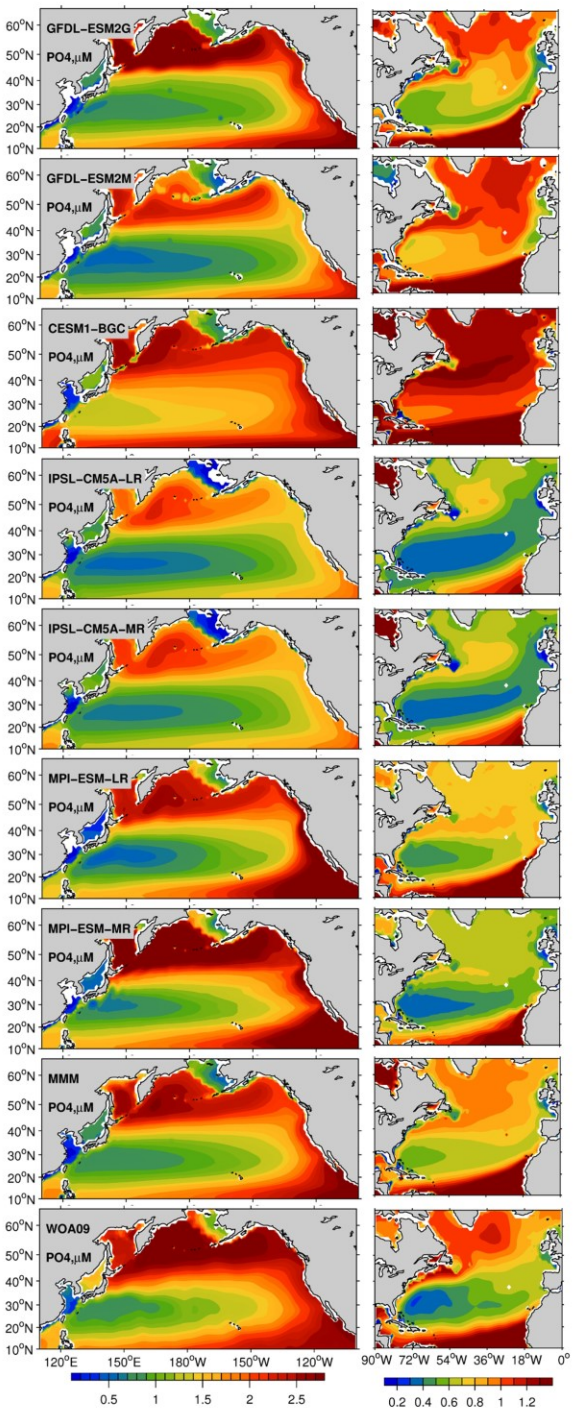

Figure 3. 1 Upper ocean (0-700 m) concentration of phosphate (PO4), for the period 1970-2000 in a subset of the CMIP5 models (esmHistorical), Multi-Model-Mean (MMM), and World Ocean Atlas 2009 (WOA09). The North Pacific and Atlantic basins are plotted with different colour ranges to better highlight the spatial patterns in models and observations.

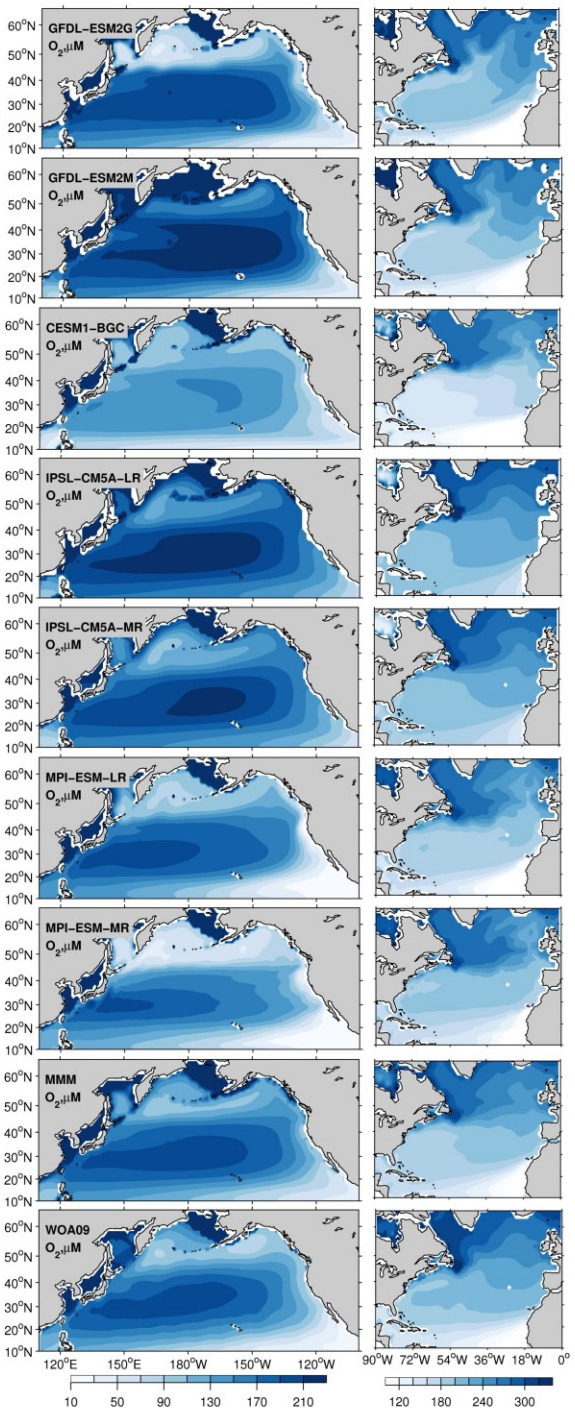

Figure 3. 2 Upper ocean (0-700 m) concentration of dissolved oxygen (O2), for the period 1970-2000 in a subset of the CMIP5 models (esmHistorical), Multi-Model-Mean (MMM), and World Ocean Atlas 2009 (WOA09). The North Pacific and Atlantic basins are plotted with different colour ranges to better highlight the spatial patterns in models and observations.

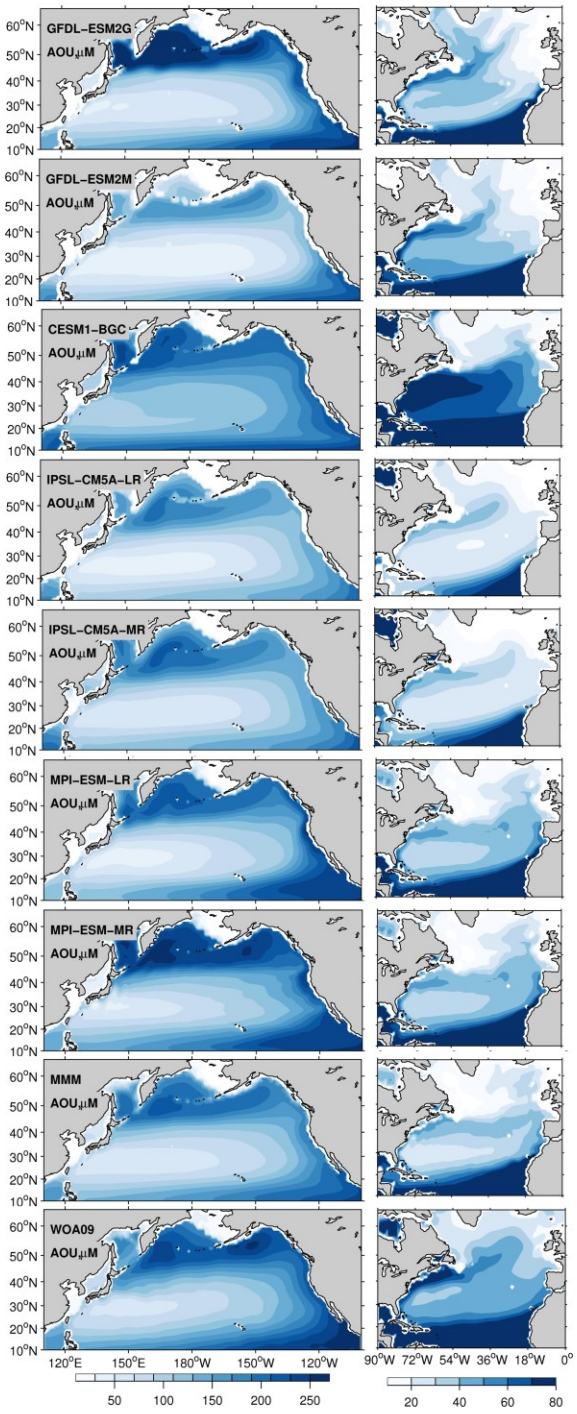

Figure 3. 3 Upper ocean (0-700 m) concentration of apparent oxygen utilization (AOU), for the period 1970-2000 in a subset of the CMIP5 models (esmHistorical), Multi-Model-Mean (MMM), and World Ocean Atlas 2009 (WOA09). The North Pacific and Atlantic basins are plotted with different colour ranges to better highlight the spatial patterns in models and observations.

3.3.2 Centennial Changes

We next examine hemispheric centennial changes of the physical and biogeochemical variables in the North Pacific and North Atlantic oceans. Changes are calculated as the differences between the 30-year period 2070-2100 in the rcp8.5 scenario and 1970-2000 in the historical simulations. We use 30-year periods to ensure that year to year changes are mostly averaged out. For O_2, T and AOU we also verify the statistical significance of the drift-corrected trends by testing if the average concentrations during 2070-2100 under the rcp8.5 scenario are significantly lower than those during 1970-2000 period relative to the interannual variability within each 30-year period. We did so using a t-test and evaluating $t = \frac{-\{(\overline{x_{rcp8.5}} - \overline{x_{his}}) - \Delta x_{piControl}\}}{\sigma\sqrt{\frac{1}{N_1}+\frac{1}{N_2}}}$ where σ is defined as $\sqrt{\frac{N_1 s_1^2 + N_2 s_2^2}{N_1+N_2-2}}$, and the degree of freedom is d.f.=N_1+N_2-2. In our case, the number of records in each sample set is the same N=N_1=N_2=30 and s_1, s_2 the corresponding sample variance. Preindustrial control simulations are used to correct for the model drift as mentioned earlier.

Under the rcp8.5 scenario, both basins warm by 0.5 - 4°C [**Figure** 3.**4]**, and the warming is generally stronger in the Atlantic than in the Pacific. A localised patch of cooling stands out in the SPNA in all models but in different locations. This patch is known as "warming hole" (Drijfhout, Oldenborgh et al. 2012, Rahmstorf, Box et al. 2015, Rahmstorf, Box et al. 2015) and is a response to the reduced poleward transport of heat due to the AMOC slowdown, which is common to all models (Tagklis, Bracco et al. 2017). The location of the warming hole depends on each model representation of the NAC pathway. Despite the presence of this cold patch, basin-scale averages between 10°N-48°N, shown in Table 3.1**,** reveal that the North Atlantic takes up more heat than the Pacific, and warms on average

$\Delta T \sim 1^{o}C$ more than the Pacific. This mean difference is consistent across the models. Additionally, in the Atlantic the warming pattern is consistent among the models, with stronger warming at the gyre boundaries, both at the tropical-subtropical and subtropical-subpolar boundaries.

Even though the Atlantic ocean is warming faster than the Pacific, the centennial changes of O_2 in Figure 3.5 reveal a more moderate deoxygenation rate in the Atlantic compared to the Pacific. The trends shown in the figure are statistically significant nearly everywhere, according to a t-test at the 99% confidence level. The oxygen trend in the Atlantic is "patchy" with the subtropics resisting to deoxygenation especially in correspondence of the Gulf Stream/NAC paths (Tagklis, Bracco et al. 2017). The subpolar regions offshore Newfoundland and Labrador, on the other hand, lose the most oxygen in this basin, in correspondence with the largest warming signal. The basin scale averages in Table 3.1 confirm that the Atlantic Ocean is losing oxygen at a lower rate than the Pacific in all seven models. The modelled basin averaged O_2 changes are between -3.4 and -12 μM but mostly in the -6 μM range in the Atlantic and between -10 to -18.1 μM in the Pacific**.** This corresponds to O_2 decline of 3% in the Atlantic and 10% in the Pacific compared to their 1970-2000 mean state.

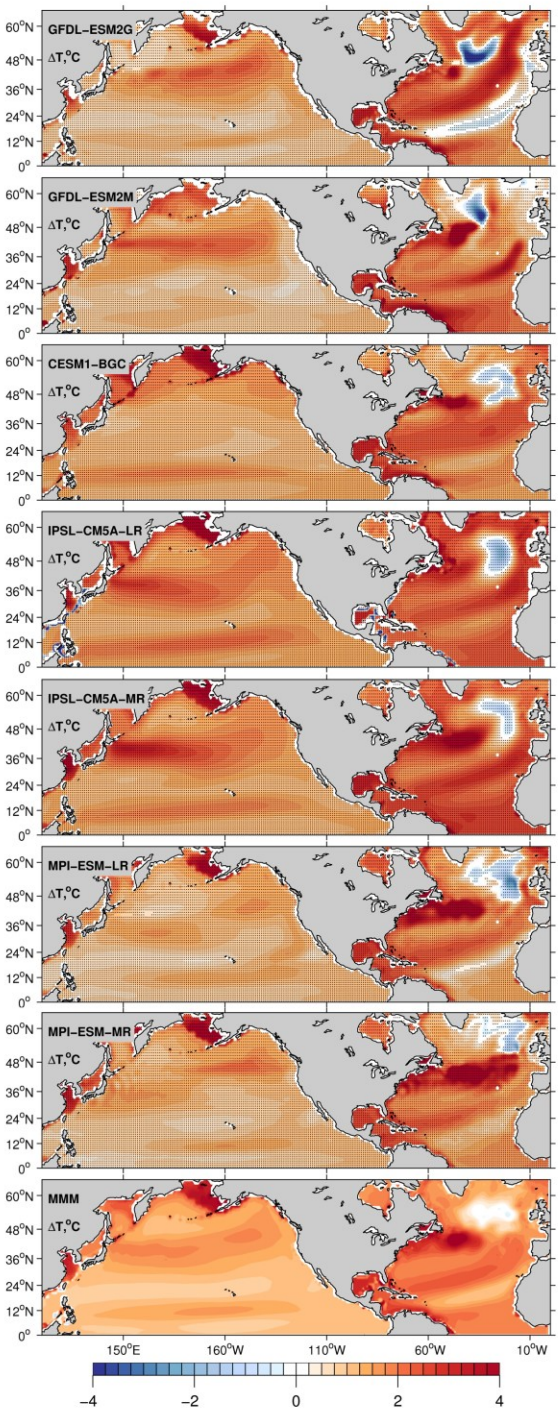

Figure 3. 4 Centennial change of T calculated as the difference in 30-year averages between (2070-2100) and (1970-2000). All plotted values are 0-700 m depth averages. Black dots indicate areas where the results are statistically significant at the 99% confidence level according to a t-test.

The inverse proportionality of the solubility of oxygen to seawater temperature implies that negative/positive changes in temperature are reflected as positive/negative changes in oxygen solubility $\Delta O_{2,sat}$. In thermocline waters, a temperature increase by 1°C causes a solubility decrease of about 7μM. Given the modeled warming trends, oxygen solubility decreases in both basins for all seven models, except for the warming holes in the SPNA. The rate of solubility change in the Atlantic Ocean ranges from -8.4 μM for GFDL-ESM2G to -12.2 μM for IPSL-CM5A-MR; in the Pacific Ocean ranges from -5.1 μM for MPI-ESM-LR to -8.6 μM for IPSL-CM5A-LR (see Table 3.1). The solubility decline is more pronounced in the subpolar Atlantic as expected, but this is in contrast to the net O_2 change in all models.

Table 3.1 Averaged changes of temperature (ΔT), dissolved oxygen (ΔO_2), oxygen solubility $\Delta(O_{2,sat})$, apparent oxygen utilisation Δ(AOU), and nutrient $\Delta(PO_4)$ between 10°N-48°N for Pacific and Atlantic basins averaged over the upper 0-700 m. The changes are calculated as the differences between the 30-year period 2070-2100 in the rcp8.5 scenario and 1970-2000 in the historical simulations.

	ΔT		ΔO_2		$\Delta O_{2,sat}$		ΔAOU		ΔPO_4	
	Pac	Atl	Pac	Atl	Pac	Atl	Pac	Atl	Pac	Atl
GFDL-ESM2G	1.14	1.69	-12.4	-6.9	-6.1	-8.4	6.3	-1.5	-0.007	-0.13
GFDL-ESM2M	1.14	2.21	-16.1	-6.1	-5.8	-11.0	10.1	-5	0.001	-0.15
CESM1-BGC	1.20	2.00	-16.8	-6	-6.2	-10.3	10.7	-4.2	-0.020	-0.16
IPSL-CM5A-LR	1.60	2.03	-18.1	-12	-8.6	-10.0	9.5	-1.7	0.000	-0.006
IPSL-CM5A-MR	1.60	2.45	-16.0	-7	-8.5	-12.2	7.5	-4.8	-0.005	-0.04
MPI-ESM-LR	1.07	1.90	-10.0	-6	-5.1	-9.5	4.6	-3.6	-0.001	-0.10
MPI-ESM-MR	1.12	2.00	-12.2	-3.4	-5.4	-10.0	6.7	-6.6	0.001	-0.10
MMM	1.26	2.04	-14.5	-6.7	-6.5	-10.2	7.9	-3.9	-0.004	-0.10

The AOU signal explains the different O_2 trend **[Figure** 3.**6]**. In the subtropical regions, the AOU decreases in all models in the North Atlantic, but increases overall in the Pacific, even if with inter-model regional differences. As the ocean's surface warms and becomes more stratified, AOU generally increases due to weakened ventilation and sustained biological O_2 consumption which dominates over the physical supply. The effect of respiration is accumulated as water spends more time in the ocean interior, leading to a decline of O_2. This is verified in most of the North Pacific and in the subpolar North Atlantic. In the subtropical North Atlantic, however, AOU and stratification decouple due to changes in lateral transport and biological oxygen utilization as shown next. Basin-scale averages of ΔAOU in Table 1 are in the range –1.5 μM for GFDL-ESM2G to **-**6.6 μM for MPI-ESM-2M in the Atlantic and in the range +4.6 μM for MPI-ESM-LR to +10.65 μM for CESM1-BGC in the Pacific. The question that naturally follows is: how could the subtropical North Atlantic have a significant decrease in AOU under the increasing stratification? It is unlikely that the thermocline ventilation increases under this condition. Also, the mechanism at work must be specific to the North Atlantic Ocean.

In all EaSMs examined the speed of the Gulf Stream and NAC extension decreases; in contrast, the speed of the Kuroshio Current does not change noticeably **[Figure** 3.**7]**. Consequently, the "nutrient stream" in the North Atlantic loses part of its strength. Since it is a major supply pathway of macro-nutrients for the North Atlantic, the nutrient inventory and the biological productivity decline in the subtropical gyre. This mechanism is confirmed by the significant decline of the PO_4 inventory projected in the North Atlantic **[Figure** 3.**8]**, and by the weakening in carbon export in all models **[Figure** 3.**9]**.

The weakened remineralization results in the regional AOU decline, which can compete against the effect of weakened ventilation. In the North Pacific, on the other hand, the PO_4 inventory displays a moderate increase, again following the currents' behaviour. Basin-scale averages of ΔPO_4 in Table 1**,** range from -0.006 μM for IPSL-CM5A-LR to -0.16 μM for CESM1-BG. In the North Pacific, the nutrient decline is close to zero. Further support for this proposed mechanism can be found in the North Atlantic in the IPSL-CM5A-LR model where the weakest current speed decline **[Figure** 3.**7]** is associated with the weakest PO_4 decline (-0.006 μM), the strongest warming and stronger deoxygenation (-12 μM; Table 1) among the models.

It is important to note there is no overall agreement in the patterns or signs of centennial changes in export production, ΔEPC_{100}, among the models. Also, the pattern of the carbon (C) export does not necessarily correspond to the changes in AOU, which instead follow the concomitant changes in ventilation. AOU reflects the integrated respiration rates over the ventilation pathways, so it is not surprising that the patterns look different between ΔAOU and ΔEPC_{100}. Having said this, it is expected that basin-scale decrese in carbon export and respiration are likely to cause a decrease in AOU. The C export decreases globally, but the magnitude of the decline is particularly strong in the North Atlantic **[Figure** 3.**9]**. It generally decreases under increasing stratification because of the reduced upwelling and entrainment of subsurface macro-nutrients, which partially compensates the deoxygenation due to the reduced ventilation. The net effect on the AOU is dominated by ventilation in the North Pacific and the subpolar North Atlantic. However, this is not the case in the subtropical North Atlantic. The decline of the C export is much stronger due to the compounding impacts of the increased stratification and the weakened North Atlantic

nutrient stream, as evidenced by the decline in the phosphorus inventory **[Figure** 3.**8]**. This is consistent with the decline in nutrient supply in the North Atlantic and the resultant decrease in AOU. On the contrary, the AOU in the subtropical gyre of the North Pacific increases, despite the weakened C export, suggesting that the weakened ventilation in this region contributes the most to deoxygenation.

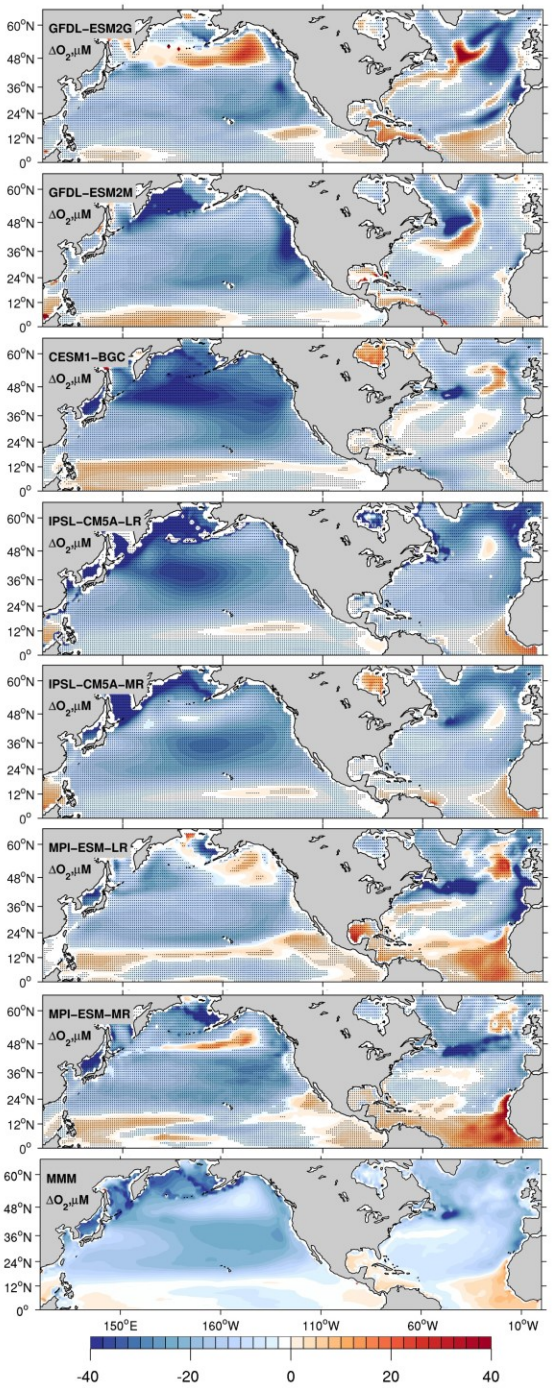

Figure 3. 5 Centennial change of dissolved oxygen calculated as the difference in 30-year averages between (2070-2100) and (1970-2000). All plotted values are 0-700 m depth averages. Drift is removed from the piControl simulation. Black dots indicate areas where the results are statistically significant at the 99% confidence level according to a t-test.

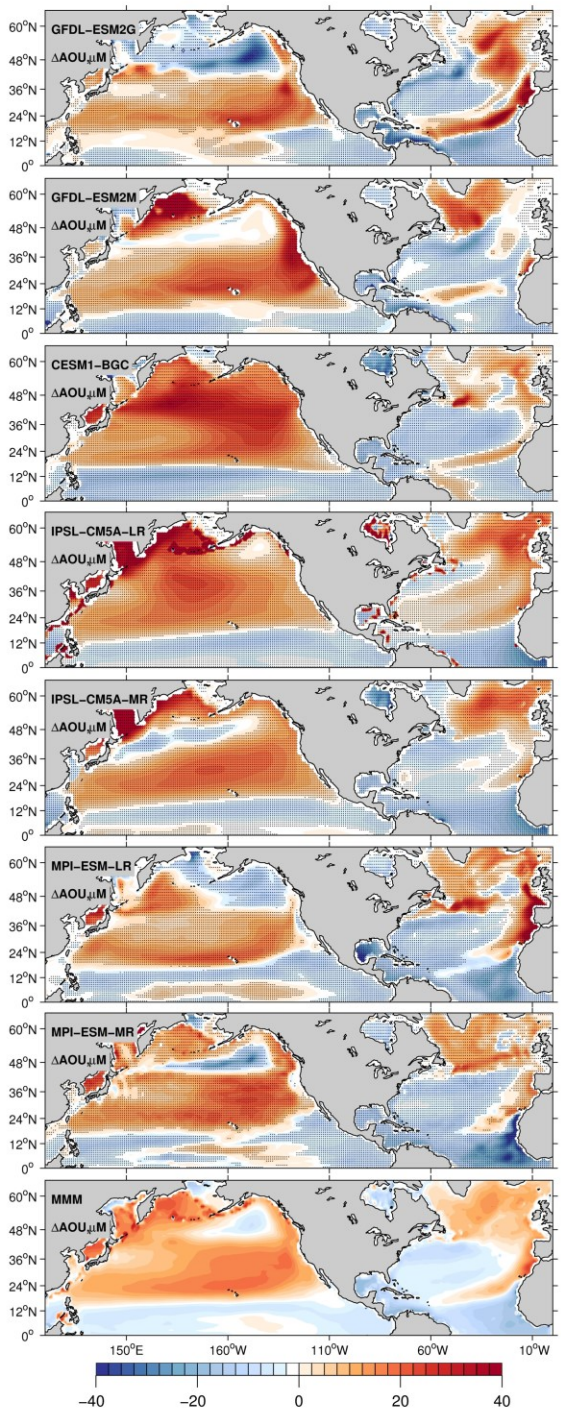

Figure 3. 6 Centennial change of apparent oxygen utilization calculated as the difference in 30-year averages between (2070-2100) and (1970-2000). All plotted values are 0-700 m depth averages. Drift is removed from the piControl simulation. Black dots indicate areas where the results are statistically significant at the 99% confidence level according to a t-test.

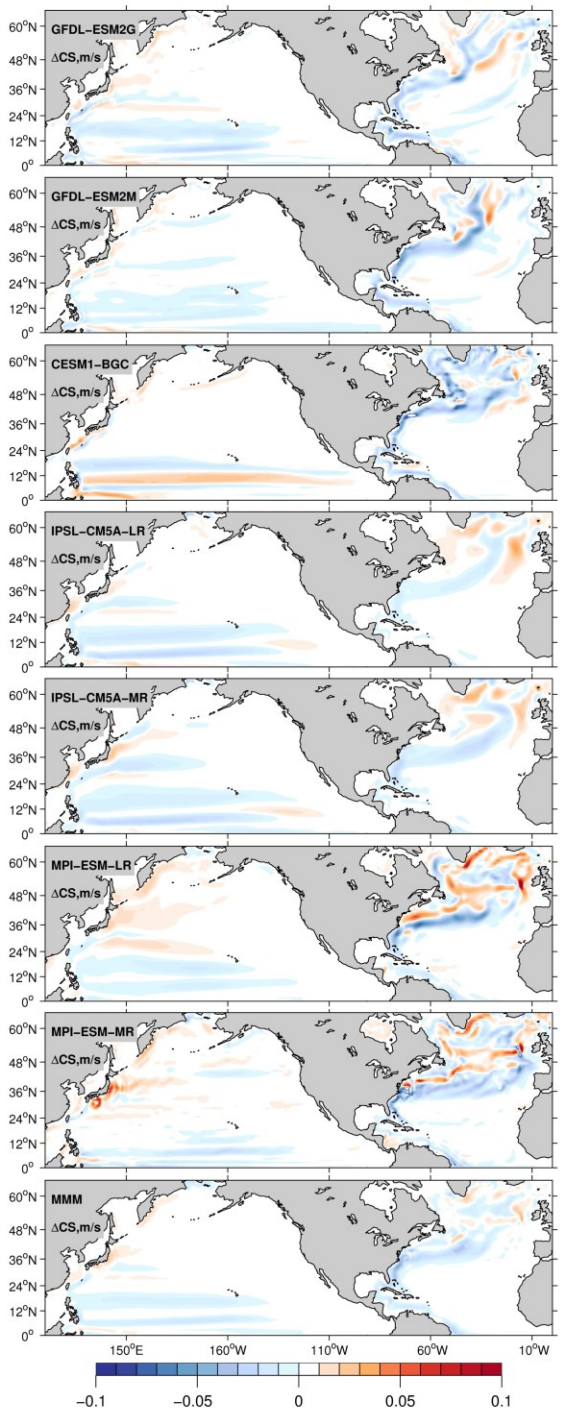

Figure 3. 7 Centennial change of current speed calculated as the difference in 30-year averages between (2070-2100) and (1970-2000). All plotted values are 0-700 m depth averages.

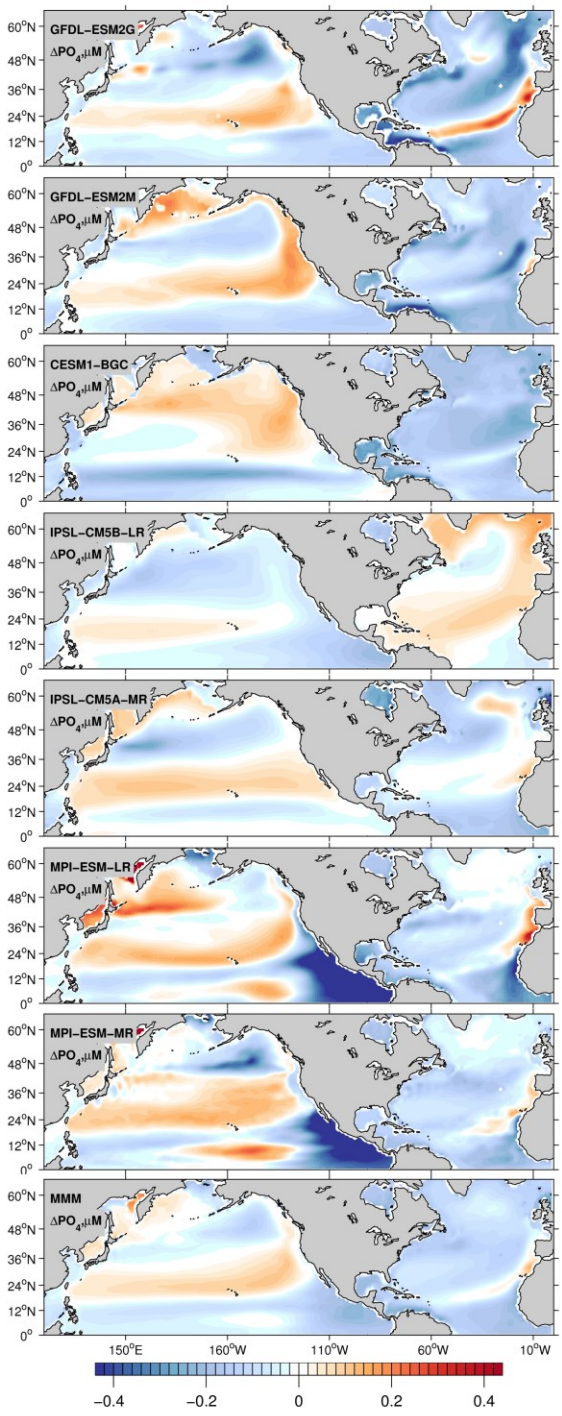

Figure 3. 8 Centennial change of PO_4 calculated as the difference in 30-year averages between (2070-2100) and (1970-2000). All plotted values are 0-700 m depth averages.

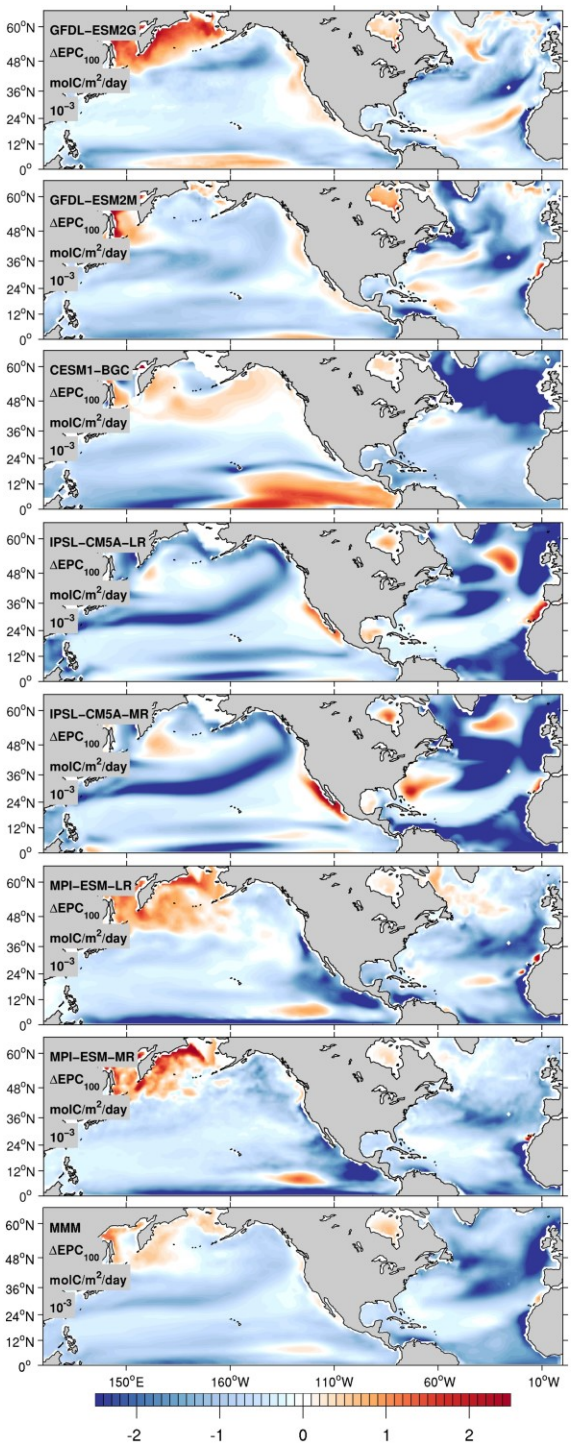

Figure 3. 9 Centennial change of export production calculated as the difference in 30-year averages between (2070-2100) and (1970-2000).

In Figure 3.10 and Figure 3.11, we further analyze the mechanisms at play in the Atlantic Basin. To investigate more in depth the nutrient inventory changes in the North Atlantic, we estimate changes of the northward supply of phosphate at 10ºN along with the nutrient inventory of the subtropical gyre. Figure 3.10 time series represent the zonally and vertically integrated northward transport of phosphate ($\overline{vPO_4}$) at 10ºN over the 0-700 meters depth range, decomposed in the overturning ($MO = \bar{v}\overline{PO_4}$) and gyre ($GY = \overline{v'PO'_4}$) components, along with the nutrient inventory (NI) zonally, meridionally and depth-integrated over 10ºN-48ºN and 0-700 meters. The overbar indicates the zonal mean, and the primes indicate the departure from the zonal mean. For better comparison, we apply a low pass filter of 10-years, and then we normalise the time series by subtracting their mean and divide by their standard deviation. The coloured values represent the percent centennial change of each transport component and nutrient inventory. The subtropical gyre nutrient inventory closely follows the declining trajectory of the overturning component of the northward nutrient transport at 10ºN for all models but IPSL-CM5A-LR.

To better understand the reduction in carbon export, we explore the nutrient supply to the surface euphotic layer through the vertical entrainment of thermocline nutrients. If averaged over a broad area, the downward export of organic matter is mostly replenished by the upwelling and vertical mixing of nutrients during cool seasons. Over the subtropical oceans, wind-driven Ekman downwelling dominates the mean large-scale circulation, so the winter-time deepening of the mixed layer is the primary pathway for the vertical nutrient supply. The entrainment flux of nutrient (P) can be represented as $E_{flux} = \wedge (P_{th} - P_m)\frac{\partial h}{\partial t}$, with the operator $\wedge = 1$ when the mixed layer thickness increases $\frac{\partial h}{\partial t} > 0$. $(P_{th} - P_m)$ is the vertical difference in nutrient concentration between the thermocline and

mixed layer. Integrating over one year, we approximate the annual entrainment as $E_{flux,ann} \sim H * dPz$, where H is the difference between the yearly maximum and minimum mixed layer depth, and dPz is the vertical nutrient difference between the surface and 300m. The centennial changes of those two terms are presented in Figure 3.10 as percent changes along with the changes of the ΔEPC_{100}. The change in sign of both terms ΔH and Δ(dPz) across SPNA and STNA are in response to different processes. We direct the reader's attention to the lower panels of Figure 3.10 and the multi-model mean behavior. In the subpolar regions, the maximum mixed layer depth is significantly reduced (ΔH<0) with the suppression of convective mixing, while the vertical gradient of the nutrient increases(ΔdPz>0). This indicates that the reduction in export production is primarily caused by the increased stratification and weakened vertical mixing of nutrients into the surface euphotic layer. The increased vertical nutrient gradient cannot cause the weakened export production. On the contrary, in the subtropical Atlantic region, the maximum mixed layer depth deepens with time (ΔH>0) along the WBC. Positive ΔH>0 tends to increase the entrainment of nutrient in the euphotic layer but the vertical gradient of the nutrient decreases (ΔdPz<0), as a result of the total nutrient inventory decline. The reduction in export production in the subtropics is likely caused by the weakened vertical gradient of nutrient. Increased seasonality of the mixed layer depth cannot explain the reduction in export production. The close relationship between the reduction in basin-scale nutrient inventory and the zonal mean (meridional overturning) nutrient transport indicates that the weakened nutrient stream is causing the weakened export production in the subtropical North Atlantic.

Finally, in Figure 3.11, we include an estimate of the regional nutrient budget using GFDL-ESM2M as a representative model. Following the geographical boundaries of the previous analysis, we consider a control volume enclosing the STNA with boundaries at approximately 10°N-48°N, 80°W-10°W and 700 meters depth using the native model grid. We calculate all lateral nutrient transport terms in and out of the control volume, in units of moles per second. Zonal and meridional fluxes are defined as positive eastward and northward, and the veritical flux is defined as positive upward.

Figure 3.11a shows the changes in magnitude and the sign of each component during the historical period 1861-2005 and rcp8.5 period 2006-2100. The northward supply of nutrients at 10°N ($vPO4_{(10oN)}$) has the most significant decline among the lateral transport terms and magnitude comparable to the northward transport of nutrient at 48°N ($vPO4_{(48oN)}$). The western boundary transport component at 80°W ($uPO4_{(80^oW)}$) represents the net nutrient supply through the Florida current which decreases to half of its magnitude by the end of the 21st century. The eastern boundary component at 10°W ($uPO4_{(10^oW)}$) remains largely unchanged. The vertical component at 700 meters depth ($wPO4_{(700m)}$) is negative (downwelling) with decreasing magnitude. The signs and the magnitude of the changes in the lateral and vertical transport terms are consistent with a weakening of the advective nutrient transport, providing additional support to our interpretation.

The flux convergence of the (resolved) advective transport must be balanced by the time derivative of the nutrient inventory and the net biological nutrient sources/sinks. Sub-grid scale parameterizations could also contribute to the regional nutrient budget. It is difficult to precisely close the nutrient budget with available dataset. However, we can still integrate over time the flux convergence of the advective transport to calculate the 'estimated'

nutrient inventory ($PO4_{estimated}$). Net advective convergence is positive, and its integral gradually increases over time because it does not include the nutrient uptake and export by biological processes (Bio). To account for the baseline pre-industrial biological component (Bio), we first determine the residual between the $PO4_{estimated}$ and the PO4 as Residual (=$PO4_{estimated}$ - PO4). The pre-industrial estimate of Bio is then estimated as a linear trend based on the first 60 years (1861-1920) of the Residual and the corrected $PO4_{estimated}$ is determined as the temporal integral of the advective flux convergence minus Bio. The $PO4_{estimated}$ time series reflects the change in STNA nutrient budget if there were no changes in biological sources/sinks (constant Bio). Figure 3.11b shows that the decline of $PO4_{estimated}$ is much larger than that of PO4. After 2005 and during the rcp8.5 period the actual PO4 inventory does not decrease as much as the estimated inventory $PO4_{estimated}$ due to the weakened biological export of nutrients. This result is consistent with a weakening of the biological productivity of the North Atlantic as well as the circulation change as drivers of the nutrient decline in the basin.

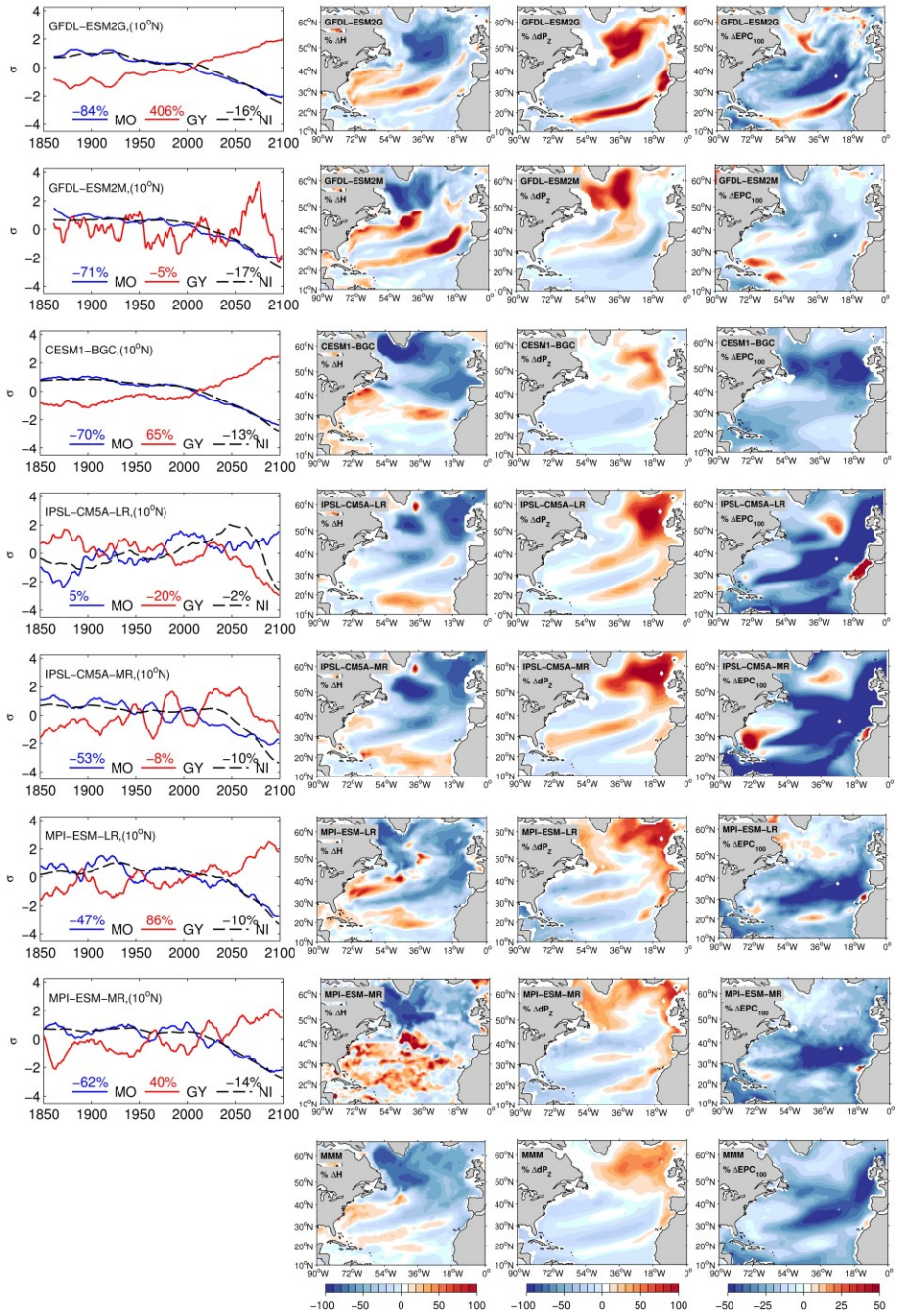

Figure 3. 10 (Left column) Normalized timeseries of zonally (70ºW-17ºW) and depth (0-700m) integrated northward nutrient transport components, ($MO = \overline{v}\overline{PO_4}$) and gyre ($GY = \overline{v'PO'_4}$), at 10ºN and nutrient inventory (NI) of the subtropical gyre (10ºN-48ºN, 0-700 meters). Coloured values represent the percent centennial change of each variable. Panels represent the percent centennial change of H (year maximum seasonal change of mixed layer depth), dPz (vertical gradient of PO_4), EPC_{100} export production, all calculated as the difference in 30-year averages between (2070-2100) and (1970-2000).

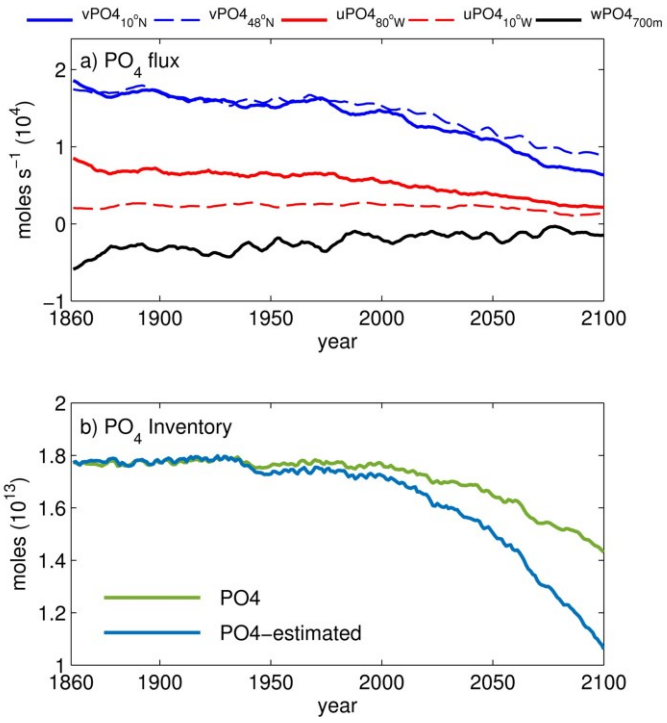

Figure 3. 11 a) Lateral nutrient fluxes in and out of a box enclosing the subtropical North Atlantic area with boundaries 10°N-48°N, 80°W-10°W and at 700 meters depth. All curved are in units of moles/s. b) Nutrient inventory estimated integrating lateral fluxes over time (light blue) and compared with the actual nutrient inventory (light green).

3.4 Conclusions and Discussion

We analyzed a subset of seven EaSMs included in the CMIP5 catalogue to understand current and future state of oxygen distribution in the upper 700 m of the water column in the northern hemisphere. During the historical period 1970-2000, models reproduce the observed mean state of dissolved oxygen concentration, capturing spatial variations in apparent oxygen utilisation and, most importantly, reproduce the "nutrient stream". By the end of this century, the upper water column in the business as usual scenario is projected

to warm more in the North Atlantic compared to the North Pacific. Despite this tendency, the subtropical North Atlantic resists to deoxygenation. As the ocean warms, O_2 saturation decreases globally, with the exception of the warming holes in the North Atlantic, but the two basins differ especially in the AOU. In the subtropical North Atlantic, the basin-mean AOU decreases and is decoupled from the stratification-induced reduction in ventilation. In all models but one (IPSL-CM5A-LR), the AMOC weakening is associated with a decline in the current speed of the Gulf Stream and its extension and, in turn, to a decline in the nutrient stream. Lateral nutrient supply, quantified by the reduction in phosphate inventory, decreases, and so does biological productivity, as confirmed by the negative trend in ΔEPC100. The decline in biological productivity and consequent retention of O_2 (by weakened biological consumption) in the subtropical North Atlantic are sizable enough to compensate the O_2 solubility trend. The decline in the nutrient stream is not detected in the North Pacific, where biological productivity does not change as dramatically as in the Atlantic, and the solubility trend dominates.

Our results imply that the ocean deoxygenation progresses more intensely in the North Pacific Ocean even though its heat uptake is moderate compared to its neighbour ocean. This faster and stronger decline appears to be supported by the relatively stable P inventory of the North Pacific. The macro-nutrient inventory of the North Pacific is “charged up” with the higher concentrations of nutrients in comparison to the North Atlantic due to the old age of the Pacific waters. In contrast, the North Atlantic nutrient inventory is more dynamic given that nutrient streams critically depend on the AMOC and its feedbacks on the western boundary current system. This difference has significant consequences given that the background, climatological O_2 levels are much lower in the Pacific basin, again

due to the older age. The Pacific Ocean indeed hosts already two of the four most voluminous oxygen minimum zones. Higher rate of O_2 loss can potentially lead to more frequent and intense hypoxic events, with devastating impacts for the marine ecosystem (Penn, Deutsch et al. 2018). The length of the EaSM integrations does not allow to verify if the reduction in the biological activity of the subtropical North Atlantic is only transient, and if a rebound may take place once a new climate equilibrium is achieved (Moore, Fu et al. 2018). Further investigations and higher resolution model outputs are also needed to better constrain the regional patterns of biological productivity and oxygen changes.

CHAPTER 4. SUBMESOSCALE MODULATION OF DEEP-WATER FORMATION IN THE LABRADOR SEA

Published as

Tagklis, F., Bracco, A., Ito, T. *et al.* Submesoscale modulation of deep water formation in the Labrador Sea. *Sci Rep* 10, 17489 (2020). https://doi.org/10.1038/s41598-020-74345-w

Abstract

Submesoscale structures fill the ocean surface, and recent numerical simulations and indirect observations suggest that they may extend to the ocean interior. It remains unclear, however, how far-reaching their impact may be - in both space and time, from weather to climate scales.

Here transport pathways and the ultimate fate of the Irminger Current water from the continental slope to Labrador Sea interior are investigated through regional ocean simulations. Submesoscale processes modulate this transport and in turn the stratification of the Labrador Sea interior, by controlling the characteristics of the coherent vortices formed along West Greenland. Submesoscale circulations modify and control the Labrador Sea contribution to the global meridional overturning, with a linear relationship between time-averaged near surface vorticity and/or frontogenetic tendency along the west coast of Greenland, and volume of convected water.

This research puts into contest the lesser role of the Labrador Sea in the overall control of the state of the MOC argued through the analysis of recent OSNAP (Overturning in the Subpolar North Atlantic Program) data with respect to estimates from climate models. It

also confirms that submesoscale turbulence scales-up to climate relevance, pointing to the urgency of including its advective contribution in Earth systems models.

4.1 Introduction

Oceanic submesoscale currents (SMCs) occur at horizontal scales of the order of 1 km in the form of density fronts, vortices, and filaments in the surface turbulent boundary layer and of topographic wakes throughout the interior (Molemaker, McWilliams et al. 2015, Bracco, Choi et al. 2016, McWilliams 2016, Srinivasan, McWilliams et al. 2019). Dynamically, SMCs are influenced, but not dominated, by the Earth's rotation and ocean stratification, which results in order 1 Rossby ($Ro = U/fl$) and Froude ($Fr = U/Nh$) numbers for these currents (U being a characteristic horizontal velocity scale, l and h horizontal and vertical length scales, f the Coriolis frequency, and N the Brunt–Vaisala frequency). In the presence of energetic boundary layer currents flowing along steep slopes, topographic wakes may become unstable with consequent generation of coherent vortices that are substantially submesoscale in nature and generated by partially unbalanced turbulence but can have size in the mesoscale (> 10 km) range. These vortices can have a long lifespan (> 1 year), travelling long distances from their point of origin, and their cumulative effect could impact the large scale transport and distribution of heat, nutrients and dissolved gases in the ocean. Few studies have focused on these features so far (Molemaker, McWilliams et al. 2015, Bracco, Choi et al. 2016, McWilliams 2016, Srinivasan, McWilliams et al. 2019), and their global impact has yet to be shown. Here, we attempt to demonstrate it focusing on the Labrador Sea (LS).

The LS is one of the two major sites of the North Atlantic where deep convection regularly occurs. Intense surface cooling during wintertime weakens the ambient stratification and induces convective mixing in the central LS and over portions of its shelves (Marshall and Schott 1999, Pickart, Torres et al. 2002). Convection mixes the surface waters to depths exceeding, in some years, 2000 m (Lazier 1988, Yashayaev 2007) and forms a fresh, cold and highly oxygenated water mass, the Labrador Sea Water (LSW). The LSW spreads southward across the northwest Atlantic at mid-depths (McCartney and Talley 1982), is a source to the North Atlantic Deep Water (NADW) and a contributor to the Atlantic portion of the Meridional Overturning Circulation (AMOC).

Despite its oceanographic and climatic importance, and the relatively good observational record (Lazier 1980, Marshall, Dobson et al. 1998, Sathiyamoorthy and Moore 2002), both ocean-only and coupled climate models suffer from biases and divergent behaviors in simulating LSW formation and variability at seasonal to decadal timescales (Canuto, Howard et al. 2004, Danabasoglu, Yeager et al. 2014, Danabasoglu, Yeager et al. 2016). A recent analysis (Li, Lozier et al. 2019) indicates that state-of-the-art climate models run by the three USA national laboratory (NCAR, NASA-GISS and GFDL) overestimate the LSW volume by 60 to 300%.

The surface circulation in the LS is cyclonic and intensified along the boundaries. Near the surface, the West Greenland Current (WGC) and the Labrador Current flow along the continental slopes, northward and southward, respectively. The WGC transports fresh and cold water from the Nordic Seas along the Greenland coast, while the Labrador Current carries cold and fresh water from Baffin Bay towards Nova Scotia. Underneath and offshore of the WGC, the Irminger Current (IC) carries the warmer and saltier Irminger

Sea Water (ISW). The IC contributes to restratifying the interior of the basin (Cuny, Rhines et al. 2002) and prevent ice formation in the central portion of the basin in winter.

Convective activity to the south of the Greenland tip is controlled by momentum fluxes and wind forcing, while in the central portion of the basin the LSW formation is driven by local surface buoyancy loss and modulated by the atmospheric heat fluxes (Luo, Bracco et al. 2014) and by ocean dynamics (Lilly, Rhines et al. 2003, Straneo 2006). Long-lived coherent mesoscale eddies populate the basin and modify the heat and salt budgets of the gyre interior. The largest are the Irminger Rings (IR) with a diameter between 30 and 60 km (Lilly, Rhines et al. 2003). They form through localized baroclinic instability (Bracco and Pedlosky 2003) near a constriction of the isobaths along West Greenland, north of Eirik Ridge (Katsman, Spall et al. 2004), are predominantly anticyclonic and transport off-shore the warm and salty water from the IC. As they approach the convective region, they release the heat in their cores and compensate the heat loss from the surface during wintertime convection (Lilly, Rhines et al. 2003, Hatun, Eriksen et al. 2007, Bracco, Pedlosky et al. 2008).

Several other factors contribute to the LS hydrography and its variability, including freshwater inputs from Arctic and Greenland Ice Sheet (GrIs) melting, continental runoff and precipitation. Over the recent decades, GrIS mass losses accelerated, especially along west Greenland, resulting in increased freshwater inputs into the adjacent seas. Future projections indicate as highly probable a further exponential acceleration (Hanna, Huybrechts et al. 2008, Fettweis, Franco et al. 2013). Freshwater fluxes contribute to the upper stratification in the LS (Boning, Behrens et al. 2016), also influencing the marine ecosystem primary productivity (Arrigo, van Dijken et al. 2017, Hopwood, Carroll et al.

2018, Oliver, Luo et al. 2018, Cape, Straneo et al. 2019). Recently, global climate models suggested that these freshwater anomalies may reduce dramatically the LS convection, weakening the AMOC (Rahmstorf, Box et al. 2015, Caesar, Rahmstorf et al. 2018). Regionally focused experiments at 2.5 km horizontal resolution, on the other hand, have shown that most of the surface meltwater runoff from southwest Greenland is not transported offshore the continental shelf (Luo, Castelao et al. 2016), with strength and direction of the winds in August and September determining the offshore transport of GrIs meltwater (Myers 2005, Luo, Castelao et al. 2016, Schulze Chretien and Frajka-Williams 2018). Little is known, however, of the contribution that SMCs may have in offshore advection of heat and freshwater anomalies.

In this work we probe how the LSW formation is represented in a regional model, at mesoscale permitting (15 km, LBR15), mesoscale resolving (5 km, LBR5) and submesoscale permitting (1.7 km and 1 km, LBR1.7 and LBR1, respectively) horizontal resolution, focusing on the contributions of submesoscale circulations. The integrations are performed with and without the GrIs meltwater input.

4.2 Methods

We use the Regional Ocean Modeling System (ROMS) (Shchepetkin and McWilliams 2003, Shchepetkin and McWilliams 2005) in its Coastal and Regional Ocean COmmunity model (CROCO) version (Debreu, Vouland et al. 2008, Debreu, Marchesiello et al. 2012). ROMS is a free-surface, terrain-following, hydrostatic primitive equation model, configured here loosely following (Luo, Castelao et al. 2016).

Convection in the LS takes place within vertical plumes of the order O(1) km in radius and vertically extend up to 2 km (Marshall and Schott 1999) that can be simulated directly only using non-hydrostatic models (Sun, Ito et al. 2017). In ROMS the non-local K-Profile Parametrization (KPP) scheme (Large, McWilliams et al. 1994) accounts for the unresolved vertical mixing and realizes the vertical turbulent fluxes as a summation of down-gradient fluxes and non-local contributions. Previous studies have shown that ROMS can properly simulate extent, seasonality and variability of convective episodes whenever the mesoscale circulation of the basin is resolved (Luo, Bracco et al. 2012, Luo, Bracco et al. 2014, Luo, Castelao et al. 2016).

The horizontal resolution in the study increases from 15 km (LBR15) to 5 km (LBR5), 1.7 km (LBR1.7), and finally 1 km (LBR1), with 30 vertical levels in all cases. We followed the offline-nesting procedure described in (Mason, Molemaker et al. 2010) as we moved towards decreasing the grid-point size, starting from the mesoscale permitting case (Figure 1). The topography is derived from ETOPO2 (Smith and Sandwell 1997). To avoid potential errors associated with the pressure gradient and the s-coordinate horizontal layers (Beckmann and Haidvogel 1993) but capture as much bathymetric detail as possible, the topography is smoothed using a logarithmic interpolation method (Penven, Marchesiello et al. 2008) to a maximum slope parameter r_{max}= 0.35. The parameter r_{max} is defined as the ratio ($r_{max}=\Delta h/h_{mean}$) of the maximum difference between adjacent grid cell depths and the mean depth at that point. The bathymetric details are important given the topographic control of the boundary current meandering and eddy formation along the West coast of Greenland, around Cape Desolation (Eden and Böning 2002, Bracco and Pedlosky 2003, Katsman, Spall et al. 2004).

The model domain in the LBR15 case covers approximately 48ºN - 66.5ºN and 34ºW - 65ºW. All boundaries are open and, at the boundaries, the velocity fields, along with temperature and salinity profiles, are nudged to the Simple Ocean Data Assimilation (SODA) reanalysis version 3.4.2 (Carton, Chepurin et al. 2018). The circulation in the basin is sensitive to the width, strength and variability of incoming currents, and the choice of SODA is supported by a previous comparison with other reanalysis products (Luo, Bracco et al. 2012). In all runs, the model is forced by daily surface winds stresses and heat fluxes from the ERA-interim product (Dee, Uppala et al. 2011) and the surface heat fluxes are corrected towards the NOAA Extended Reconstructed Sea Surface Temperature (ERSST), Version 4 (Huang, Banzon et al. 2015) , available at (https://psl.noaa.gov/thredds/catalog/Datasets/noaa.ersst.v4/catalog.html). As we increase horizontal resolution, the size of the nested domains decrease and boundary conditions are extracted from the run at the immediately lower resolution, so that LBR1 covers only the Labrador Sea proper (52.5ºN - 65.5ºN and 44ºW - 64ºW) (Figure 1B). We choose to impose high frequency boundary conditions (3-day averages) to avoid deflections along the southern boundary.

Stratification and horizontal density gradients along the west and east Greenland coasts (west of 47.6ºW, east of 44.2ºW and south of 66ºN) are strongly affected by the seasonal meltwater inflow from the Greenland fjords which is greatest during summer, between July and September. We focus in the period September 2007 – August 2013, during which very different momentum and meltwater fluxes conditions were observed. In a first set of runs, the meltwater is included and the input dataset used is that in (Luo, Castelao et al. 2016). The runoff at the 108 major fjords along the whole coast of Greenland is estimated by the

Modele Atmospheric Regional (MAR) coupled to the 1-D Surface Vegetation Atmosphere Transfer scheme Soil Ice Snow Vegetation Transfer (SISVAT) (Gallée and Schayes 1994). The amount of meltwater introduced from GrIs (Figure 1C) does not vary among the experiments but the number of source points 'fjords' may differ due to grid size limitations. For example, in the lower resolution case the meltwater is introduced at 80 grid points by summing up the discharge amount of two or three fjords within one CROCO grid cell into one source point. A passive tracer is also released at each source point with constant concentration and in each experiment, except for the highest resolution run. At all 'fjords', the meltwater and the corresponding passive tracer are injected with a constant vertical profile and among s-layers. In LBR1 the eastern boundary is located at 44^{o}W, thus the meltwater signal originating from the east coast of Greenland is introduced in the LS domain through the eastern open boundary nested onto the LBR1.7 case.

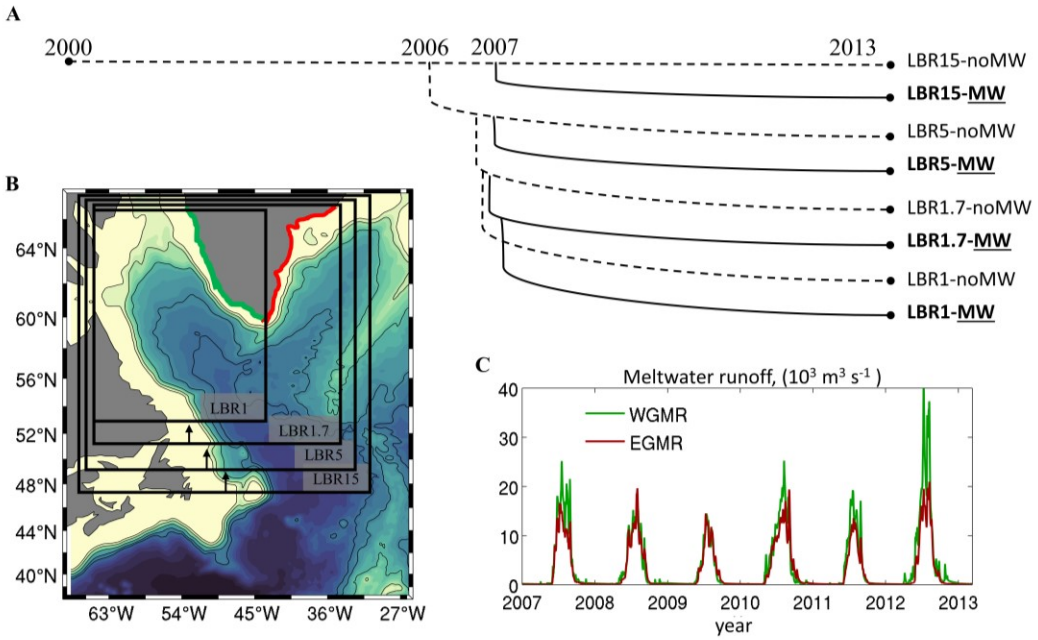

Figure 4. 1 . (A) Flowchart of experiments. Dashed black lines represent the experiments in the absence of meltwater input from the GrIS (noMW) and solid black lines represent the experiments with meltwater released along the Greenland coast (MW). (B) Black squares represent the boundaries of the domains with arrows pointing towards the nested domains. (C) Total GrIs meltwater runoff summing up the sources along the West Greenland coast (WGMR) and East Greenland coast (EGMW).

4.3 Results

4.3.1 Resolution dependency on mean circulation, eddies and vorticity

The mean circulation in the Labrador Sea is well reproduced in all numerical experiments, independently of the horizontal resolution. The maximum transport in the basin is 42 Sv ($1Sv=10^6$ m^3s^{-1}) in agreement with previous estimates (Reynaud, Weaver et al. 1995, Fischer, Schott et al. 2004). The mean WGC speed over the Greenland shelf is in the range of 0.2-0.4 m s^{-1}, comparable with the observed value of 0.35 m s^{-1} obtained from surface drifters (Cuny, Rhines et al. 2002). In the proximity of Hamilton Bank, the simulated Labrador Current speed is also in agreement with observations (~ 0.20 m s^{-1}) and is about 0.2-0.4 m s^{-1} onshore (Figure S1). Differences in the mean circulation among experiments can be summarized as follows: the intensity of the WGC, EGC and LC currents increases for increasing resolution; while intensity increases, WGC narrows and in the 1.7 km and 1 km resolution runs the intensification is confined to the core of the current that sits offshore the shelf and away from the fjords. The broader WGC flows westward at 60°N following a steady path along the 3000 meters isobath in the mesoscale permitting resolution, while the westward veering begins at lower latitudes, south of Cape Desolation, in the LBR5, LBR1.7 and LBR1 cases.

In Figure 2A the variance of the sea surface height averaged over the integration period is presented as a proxy of eddy activity. The maximum variability occurs off the west coast of Greenland, around 61°N and 52◦W, and a secondary maximum in the central Labrador Sea is found at about 58°N and 52◦W, as in the altimetric data (Prater 2002). The strength of the signal in both simulated areas of maximum variability increases with resolution.

Surface vorticity differs significantly among simulations, especially in winter, when eddies are more abundant (Luo, Bracco et al. 2011) [Figure 2B]. CROCO captures the formation of the IRs (Eden and Böning 2002, Hatun, Eriksen et al. 2007, Chanut, Barnier et al. 2008) only at the three finer resolutions, 5 km, 1.7 km and 1 km; more intense mesoscale eddies, submesoscale coherent vortices (or SCVs) and vorticity filaments (McWilliams 2016) fill the basin in the LBR1.7 and LBR1 simulations, as quantified by the time series of the domain-averaged vorticity [Figures 2C]. SCVs form abundantly where the continental slope meets the shelf which corresponds, on the Greenland side, at the meeting point between the IC and WGC. The time-series of absolute relative vorticity display small and comparable interannual variability in all cases and a seasonal cycle that becomes more pronounced the higher is the resolution, with elevated values from mid-November to May and a less active period during summer and early fall. In the submesoscale permitting cases, the winter amplification follows that found in open ocean studies (Mensa, Garraffo et al. 2013, Brannigan, Marshall et al. 2015, Callies, Ferrari et al. 2015). Noticeably, the increase in vorticity towards the end of summer happens not only faster but also slightly earlier in LBR1.7 and LRB1 compared to the mesoscale resolving case (LBR5).

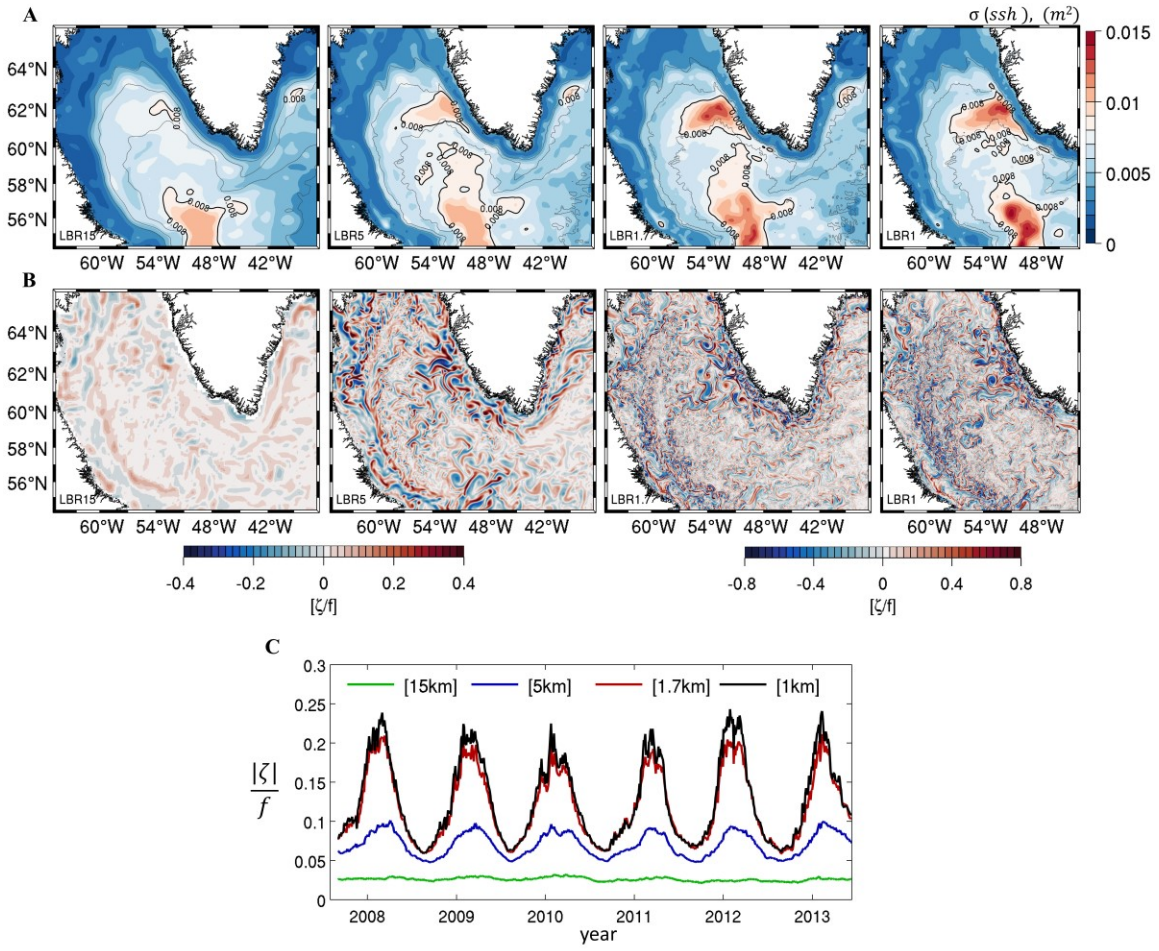

Figure 4. 2 (A) Sea surface height variance over the period September 2007- August 2013. Dashed, gray lines represent the 1000m, 2000m and 3000m isobath. (B) Instantaneous snapshots of surface relative vorticity normalized by Coriolis (ζ/f) in February 2009. The color intervals are chosen to highlight the structures but are not representative of the extremum values. Days plotted vary across runs and in the LRB5 and LBR1 cases were selected to have comparable mesoscale circulation offshore West Greenland. (C) Fall 2007- summer 2013 time-series of the absolute value of surface ζ/f averaged over LRB1 domain.

4.3.2 Resolution dependency on Deep Water Formation

Next, we explore the horizontal resolution dependency of the representation of deep convection in the LS, spanning different dynamical ranges, from mesoscale to submesoscale permitting. We quantify the impact of horizontal resolution in the representation of LSW formation computing the mixed-layer depth (MLD) over the basin, defined as the depth at which density differs from the surface by 0.008 kg m^{-3}, as in (Luo, Bracco et al. 2014). This threshold follows from the observation in (Frajka-Williams, Rhines et al. 2014) that density differences between the surface and the base of the mixed layer in the LS during convective events can be smaller than 0.01 kg m^{-3}, usually adopted in numerical studies (Lazier, Hendry et al. 2002). The convective patch is then defined as the area $A_{MLD>1000m}$where the MLD exceeds 1000 m, and the convective volume V_{MLD} (m^3) as the volume of water contained within this patch from the surface to the base of the mixed-layer ($V_{MLD} = \int_0^{MLD_{Base}} A_{MLD>1000m} dz$).

The MLD averaged over the period January-May of each year (2008-2013) is shown in Figure 3A for all simulations. The modelled convective patches are centered at about [57ºW - 57ºN], consistent with observations (Pickart, Torres et al. 2002, Vage, Pickart et al. 2009), but their extent differs significantly among runs. Convective area and convective volume decrease as resolution increases. As previous regional simulations have shown (Luo, Bracco et al. 2014), and in agreement with observational and modelling studies (Delworth and Greatbatch 2000, Eden and Willebrand 2001, Bentsen, Drange et al. 2004, Luo, Bracco et al. 2014, Holte, Talley et al. 2017), temporal characteristics of convective activity as initiation, intensity, seasonality and duration are modulated foremost

by the strength of the atmospheric heat fluxes, and secondly by the characteristics of the IC that is advected to the interior of the LS basin. From a numerical point of view, the representation of the boundary current system and its instabilities is important for reproducing correctly such stratification. The IRs, in particular, contribute through eddy-induced lateral fluxes and lateral mixing (Lilly, Rhines et al. 2003); however their effectiveness depends greatly on model resolution. In the simulation that barely resolves the Rossby deformation radius of the basin (LBR15), the absence of vigorous mesoscale activity causes a weak stratification of the upper water column in the central portion of the basin, as to be expected, resulting in stronger mixing and a deeper mixed layer patch that extends further north compared to the higher resolution cases (Figure 3). Resolving the mesoscale circulations (LBR5) induces a nearly 50% reduction of the convective volume produced by LBR15. This is shown in Figure 3B by the time series of the difference in convective volume between the lowest resolution experiment in the absence of meltwater input (LBR15-NoMW) and all other runs. The meltwater from the GrIS further decreases convection by an additional 2.7% (LBR5-MW). As Figure 3C suggests, in LBR5, this additional reduction takes place in the northeast corner of the convective patch case (thick versus thin blue lines). The contribution of submesoscale advection amounts to another 30% decrease. Differences between LBR1.7 and LBR1, with and without GrIS input, remain linear. This information is further quantified in Figure 3D, where the convective volume averaged over the convective season (Jan-May) is plotted against the mean value of near surface vorticity averaged over the LBR1 domain. A linear fit describes well the dependence of the time averaged quantities. It is enlightening to visualize the link between

meso- and submeso-scale circulations and MLD also through time-snapshots of MLD, shown for various days in February 2009 in Figure S2.

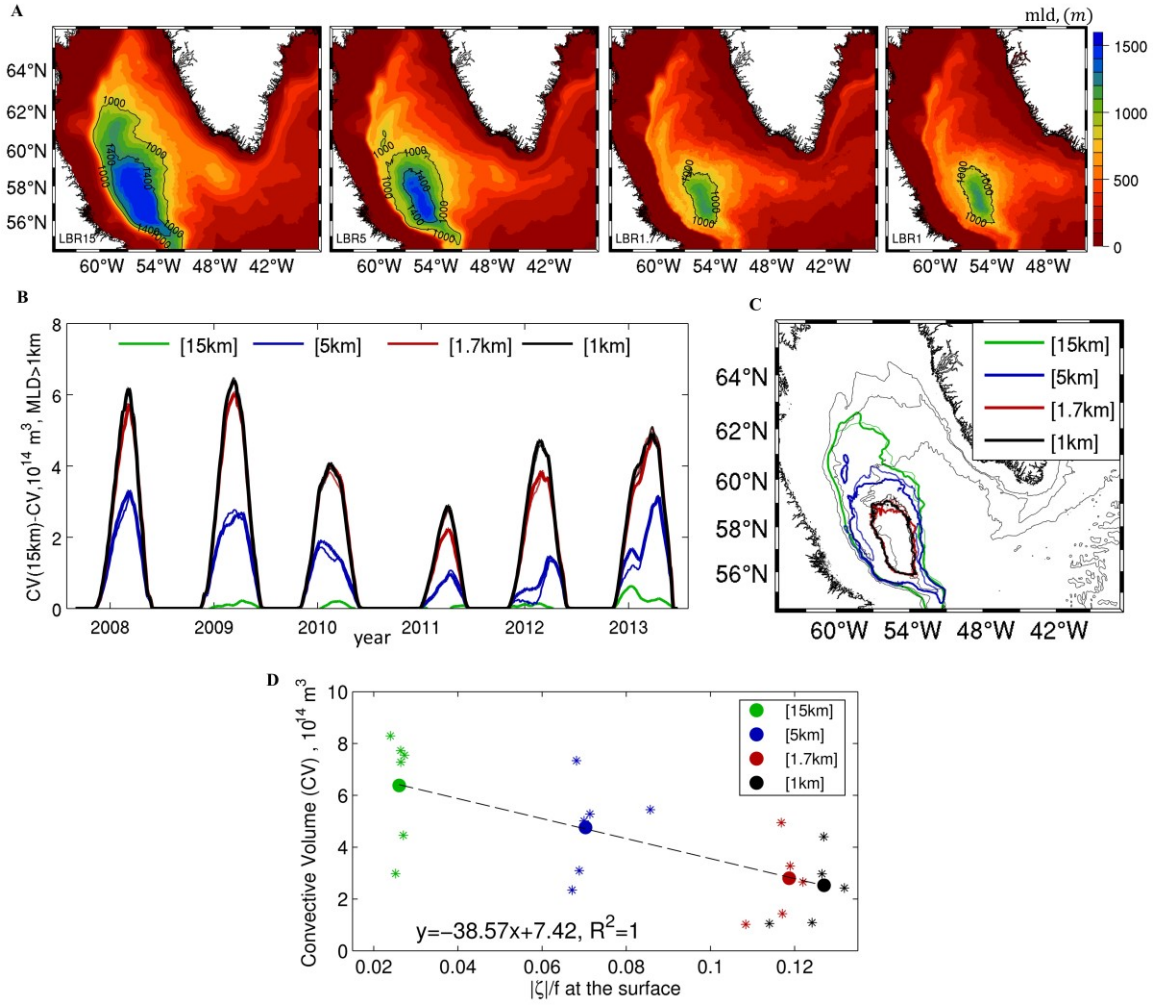

Figure 4. 3 (A): 5-year mean (2008-2013) mixed layer depth (in meters) defined using a density criterium 0.008 kg m^{-3} during the convective season (January-May). (B): Time series of the difference in convective volume (m^3) between the LBR15 NoMW case and all other simulations. (C): mean (2008-2013, January-May) convective patch, where MLD > 1000 m. Color represents the resolution and thickness indicates the experiment. Thick lines for MW experiments, thin lines for NoMW experiments. (D) Mean Jan-May convective volume (CV) and mean absolute value of surface ζ/f averaged over LRB1 domain. Stars represent annual means and dots represent the multi-year (2008-2013) means. The dashed line shows the linear fit based on the multi-year means.

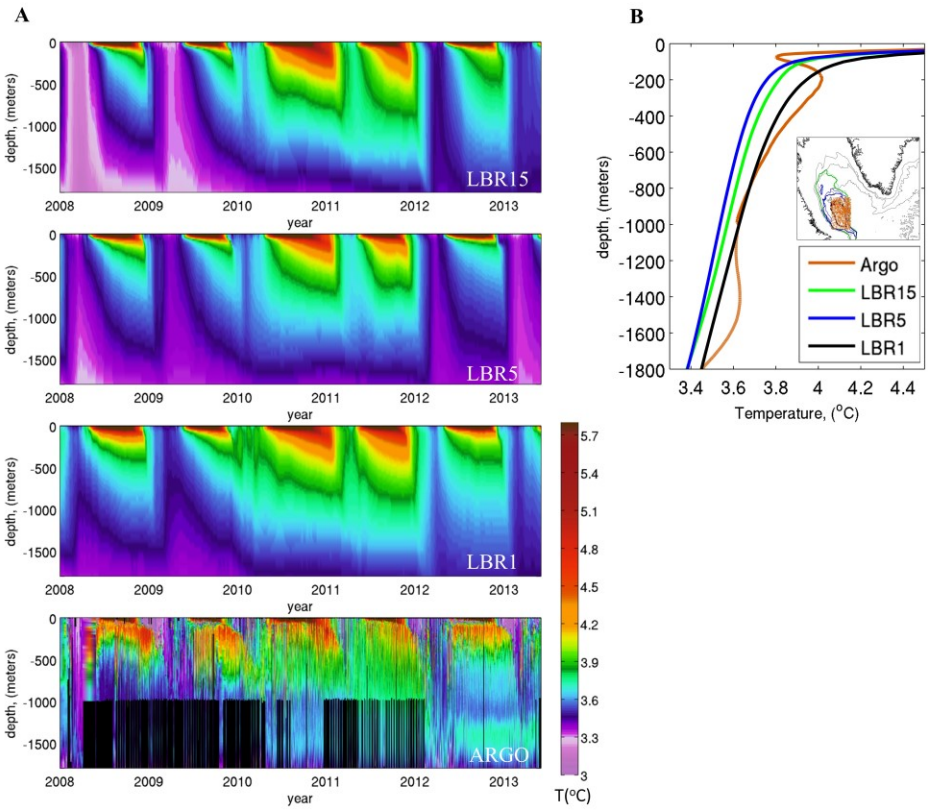

Figure 4. 4 (A) Evolution of potential temperature (T, in °C) in the region encompassing the convective area common to all simulations shown in LBR15, LBR5 and LBR1 and in the ARGO dataset from 2008 to 2013. Vertical temperature profile over the same region averaged over the entire period. The ARGO portion below 1000 m (orange) is dashed due to the paucity of profiles available. The average number of ARGO profiles in any given month is about 20 and varies between 2 and 70 with a positive trend over time; several profiles do not extend below 1000 m depth.

Previous simulations (Luo, Castelao et al. 2016) at 2.5 km horizontal resolution suggested that salinity anomalies are trapped by the energetic current system along the shoreline and on the shelf, winds are key to exporting the meltwater signal off-shore (Luo, Castelao et al. 2016, Schulze Chretien and Frajka-Williams 2018), and the meltwater modulation of deep convection is likely small in current meltwater conditions. This is confirmed by the

present experiments, independently of resolution. As the resolution increases towards submesoscale permitting, we observe additional export of meltwater towards the central Labrador Sea. The surface meltwater signal delimits in all cases the edges of the convective area (Figure S3) but has only a small impact on the overall convective activity for a given resolution (Table 1). The impact is inversely proportional to model resolution. Whenever the resolution is low, some GrIS meltwater can be advected into the convective area by the broader and more diffused boundary currents.

Table 4.1 Convective volume as a percentage to the volume produced in the lowest resolution 15 km case in the absence of melt water input from the GrIS (LBR15-NoMW) calculated over the convective period January to May and 2008-2013.

In comparison to LBR 15 km (NoMW)	Convective Volume (% LBR 15 -NoMW)	
	NoMW	**MW**
LBR15 (15 km)	100	**98.3**
LBR5 (5 km)	**52.8**	**50.1**
LBR1.7 (1.7 km)	**16.4**	**16.3**
LBR1 (1 km)	**15.8**	**15.3**

To verify that the representation of convective activity improves in realism whenever submesoscale processes are included, in Figure 4 A,B we compare the simulated temperature profiles averaged in a region that encompasses the common convective area (MW-experiment) over the integration period, and the same quantity reconstructed from ARGO floats. The average number of ARGO profiles in each month is about 20. The best representation of the mean temperature stratification is provided by LBR1 with LBR1.7 (not shown) being a close second, while a cold bias characterizes the other two resolutions,

in line with the greater convective volume. We note the poor representation of the details in the vertical structure found in the observed temperature profiles in the upper 400 m. The limited vertical resolution adopted is likely responsible for it. Indeed, 50 vertical levels would be needed to resolve the first baroclinic mode, with an additional 25 levels per subsequent mode (Stewart, Hogg et al. 2017) .

The very small differences between the integrations with and without meltwater suggest that the salinity anomalies linked to the GrIs do not contribute significantly (yet) to the stratification of the LS interior. Differences in overall heat transport must therefore drive the resolution dependence by controlling the stratification in the central portion of the basin; alternatively or additionally, submesoscale eddies formed locally in the central LS may restratify the water column in winter and impede convection. To verify both possibilities, in Figure 5, we evaluate the eddy contribution to the heat transport and the local available potential energy release in winter among the MW experiments. In Figure 5 A the depth-integrated eddy advection (E) of heat is presented for the four different resolutions. Eddy advective fluxes are defined as $E = -\nabla(\overline{u'C'}) - \partial_z \overline{w'C'}$ and the depth-integration extends to the whole water column. Prime values indicate the deviation from the average over the whole period (2007-2013), and the overbar indicates again their time average. ∇ is the 2 dimensional gradient operator; u(u,v) and w are the horizontal and vertical components of the velocity field, respectively; $C = \rho_o c_p \theta$ is the heat content, and ρ_o, c_p and θ are the reference density, specific heat, and potential temperature of water. Mean advective fluxes, defined as $M = -\bar{u}\nabla\overline{C} - \overline{w}\partial_z\overline{C}$ can be found in Figure S5. The spatial structure of both net mean and eddy contribution is far more complex in the three finer resolutions (LBR5, LBR1.7 and LBR1) than in LBR15 where a local maximum

cannot be distinguished, but the integral of the net mean contribution where convection can take place – the LBR15 convective patch - does not vary significantly across resolutions. For the eddy component (Figure 5A), on the other hand, very high values of E are located off the Greenland coast, in the region of eddy formation, in the mesoscale resolving and submesoscale permitting simulations (LBR5, LBR1.7 and LBR1), consistent with (Chanut, Barnier et al. 2008, Saenko, Dupont et al. 2014). Furthermore, in LBR1.7 and LBR1 the convergence of heat by eddy advection is large also in the central Labrador Sea following the IR path, with the maximum values reaching $E > 500$ Wm^{-2} to the north-northeast of the LBR1.7 and LBR1 convective patches. This heat convergence therefore delimits the convective patch in the submesoscale permitting runs by controlling the stratification in the off-shore portion of the basin. The time-mean eddy contribution to heat advection over the LBR5 convective area is 70 Wm^{-2} and over the same area increases to 83 and finally 90 Wm^{-2} in LBR1.7 and LBR1, respectively.

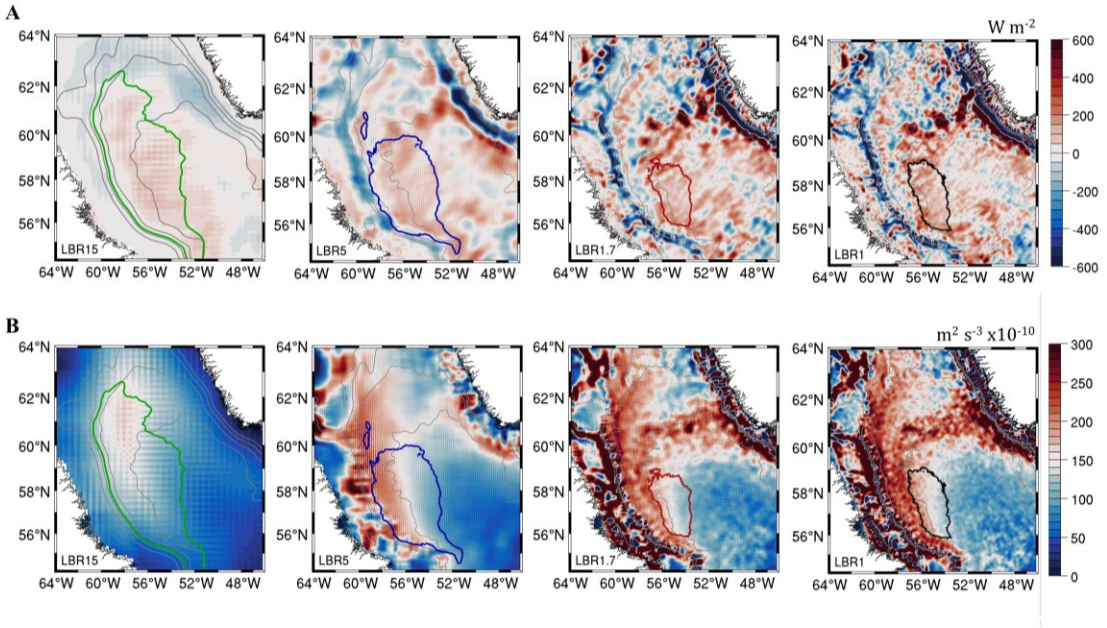

Figure 4. 5 . (A) Depth integrated eddy heat advection (W m^{-2}). Positive/negative values translate to heat convergence/divergence and temperature -and therefore stratification - increase/decrease. (B) Depth integrated vertical eddy flux of buoyancy, $\frac{1}{H}\int_0^H \overline{w'b'}\,dz$ over the top H=400 m. Thick colored contours represent the mean convective region (Figure 3C) and thin grey lines represent the 500-m, 1- , 2- and 3-km isobaths.

Submesoscale circulations, and specifically mixed-layer eddies, can also contribute to restratifying locally the upper portion of the water column (Boccaletti, Ferrari et al. 2007), and this contribution can be parameterized in climate models (Fox-Kemper, Ferrari et al. 2008). This local restratification mechanism can be evaluated through the available potential energy (APE) release in the convective season, from December to April. Such release is estimated by the vertical eddy flux of buoyancy, $\overline{w'b'}$, where b is buoyancy, here integrated over the upper 400 m of the water column, given the extent of the submesoscale circulations and the core of the IR (Figure 5B) . The APE release is small in

LBR15 everywhere but in the convective area, as to be expected, and increases by increasing resolution. Such increase is strong on the western portion of the basin between the 2000 and 3000 m isobaths in all other runs, and also along the IR path and the Greenland slope in LBR1.7 and LBR1. The APE release inside each respective convective area does not vary significantly or linearly between mesoscale resolving and submesoscale permitting runs (149, 146 and 158 x 10^{-10} m^2s^{-3} from LRB5 to LBR1), but increases steadily by 20 and then 30 x 10^{-10} m^2s^{-3} in the region comprised between the western boundary of the LBR1.7 and LBR1 patches and the 2000 m isobath to the west of it.

Overall, the latitudinal shrinking of the convective patch for increasing model resolution is dominated by the eddy-driven heat convergence, while the longitudinal shrinking is modulated by both mechanisms, with the local, restratification induced by the numerous submesoscale eddies (see Figure 2) playing a major role.

While the meltwater signal is confined near the surface and does not influence convection strongly, the advection pathways of the meltwater from Greenland into the interior provide another indication of the processes at play. In the submesoscale permitting cases, advection from the boundary currents is accomplished by the long-living population of anticyclonic vortices and cyclonic vorticity filaments characterized by *Ro* of order 1. The submesoscale process behind the subsurface intensification of these circulations in LBR1 or LBR1.7 compared to the lower resolution cases is, predominantly, strain-induced frontogenesis (McWilliams, Gula et al. 2015) along the continental slope. This is supported by the snapshots of the strain field at 200 m of depth, defined as $S = \left[\left(\frac{\partial u}{\partial x} - \frac{\partial v}{\partial y}\right)^2 + \left(\frac{\partial v}{\partial x} - \frac{\partial u}{\partial y}\right)^2\right]^{1/2}$ and the time-series of frontogenetic tendency, defined as $F = \frac{D(\nabla_h \rho)}{Dt} =$

$Q\nabla_h\rho$ with $Q = (Q_1, Q_2) = -\left(\frac{\partial u}{\partial x}\frac{\partial \rho}{\partial x} + \frac{\partial v}{\partial x}\frac{\partial \rho}{\partial y}, \frac{\partial u}{\partial y}\frac{\partial \rho}{\partial x} + \frac{\partial v}{\partial y}\frac{\partial \rho}{\partial y}\right)$ (Hoskins 1982, Capet, McWilliams et al. 2008) where *u* and *v* are the horizontal velocity components and ρ is density, shown in Figure 6. The generation of fronts, or frontogenesis, whenever F > 0, is indicative of the break-down of geostrophic balance and therefore submesoscale dynamics. The IRs in both LBR5 and LBR1.7/LBR1 simulations form near the separation point between the shallow coastal shelf and the deep continental slope along the west Greenland coast by baroclinic instability. They extend vertically to about 400 – 500 m, encompassing the IC core located between 100 and 300 m depth and their generation and overall impacts are independent of the meltwater input. They form in correspondence of the steepening of the bathymetry and result from baroclinic instability of the horizontal shear layers induced by the warm IC that meets the steep continental slope (Figure 7) (Bracco, Pedlosky et al. 2008). Resolution influences their characteristics in two ways. First, the steepness and veering of the actual bathymetry are better resolved in the LBR1 (and LBR1.7) than in LBR5 (or LBR15), contributing to the confinement, intensification and increased variability of the IC (Figure 7C-D). Second, the horizontal shear layer coinciding with a non-zero vertical component of the vorticity tensor that extends into the interior, because the interior mean flow has to be identically zero at the sloping bottom, is better resolved and intensified through strain-induced frontogenesis (Figure 6C-D, Figure S4 and video VS1) in the submesoscale permitting cases. In sum, in LBR1 and LBR1.7 this horizontal shear layer is more intense and has an elevated positive frontogenic tendency. There is indeed a nearly perfect linear relationship also between the frontogenetic tendency along the coast of Greenland at 200 m depth and the convective volume, similarly to what seen for surface vorticity (Figure 6E, F). The end result is the formation of eddies of size

comparable to the mesoscale case, being the size controlled by the bathymetry (Bracco and Pedlosky 2003, Bracco, Pedlosky et al. 2008), but of submesoscale strength ($Ro \sim 1$) being originated from the submesoscale fronts (Figure 7E-H). The eddies are then surface-intensified by the strong and variable winds. The IRs in the LBR1.7 and LBR1 runs are not only stronger, but they are also longer living that the LBR5 counterpart, are surrounded by submesoscale filaments, and, together with the filaments, contribute more effectively to the advection of warm water into the center of the LS. They form abundantly especially in late fall and winter, when the winds and the boundary current are stronger and more variable (Luo, Bracco et al. 2011), and they stratify the portion of the basin they travel to, effectively delimiting the convective patch and its volume. In this regard, Figure S3, showing the distribution of passive dye released at the fjords at the various resolution is illuminating. In doing so, they also transport freshwater originated from the GrIS melting, but the freshwater anomaly remains within the stratified region, where convection does not occur anyway, because of the IC heat contribution and the submesoscale eddy-induced restratification.

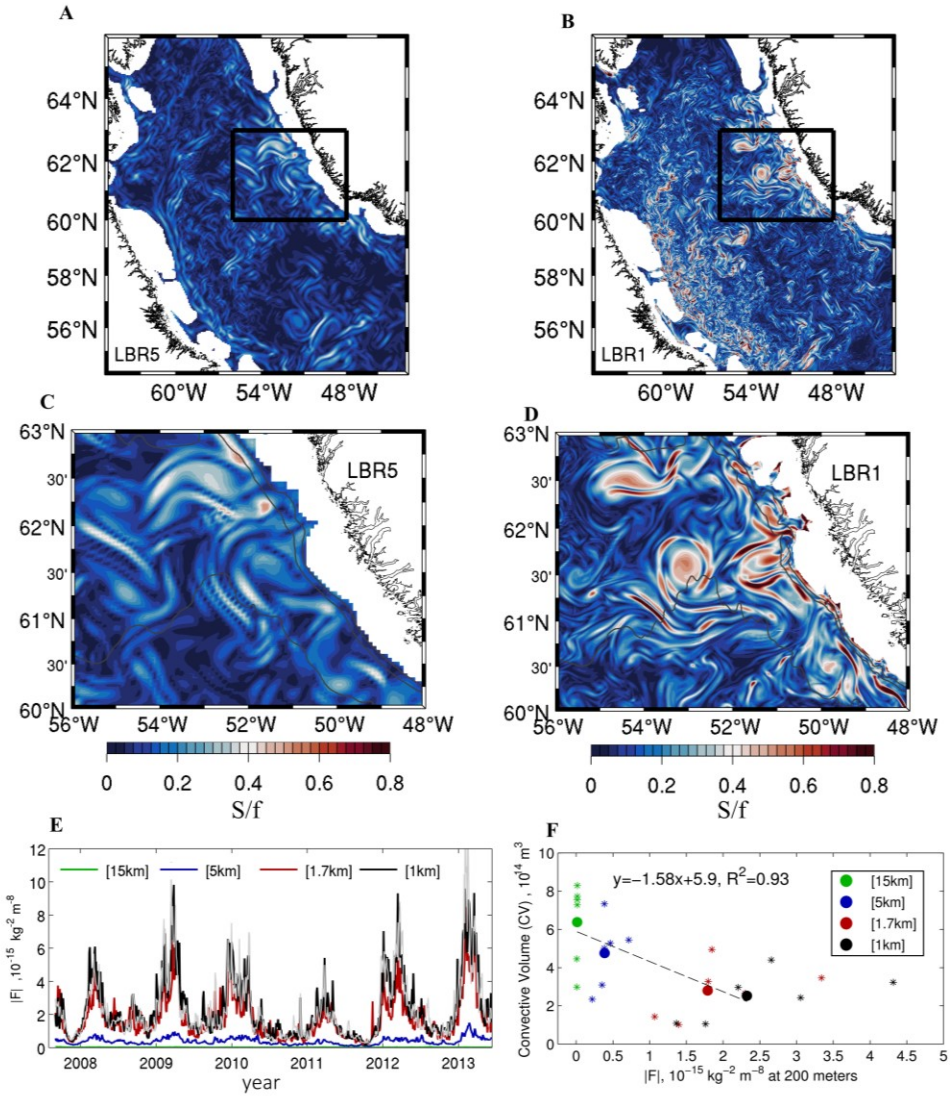

Figure 4. 6 (A-B): Instantaneous snapshots of strain rate normalized by Coriolis (S/f) in the LBR1 domain (times as in Fig. 1). High values, accompanied by a high frontogenetic tendency (Fig. S2), are indicative of submesoscale dynamics. (C-D): Zoom of (A-B) over the constriction of the isobaths along West Greenland, north of Eirik Ridge, where IRs are formed. (E): Time series of frontogenetic tendency |F| averaged over the LBR1 domain. (F) Mean Jan-May convective volume (CV) plotted against mean absolute value of F at 200 meters depth averaged over the domain of panels C and D. Stars represent annual mean values and dots represent the multi-year (2008-2013) mean. The dashed line shows the linear fit for the multi-year mean values.

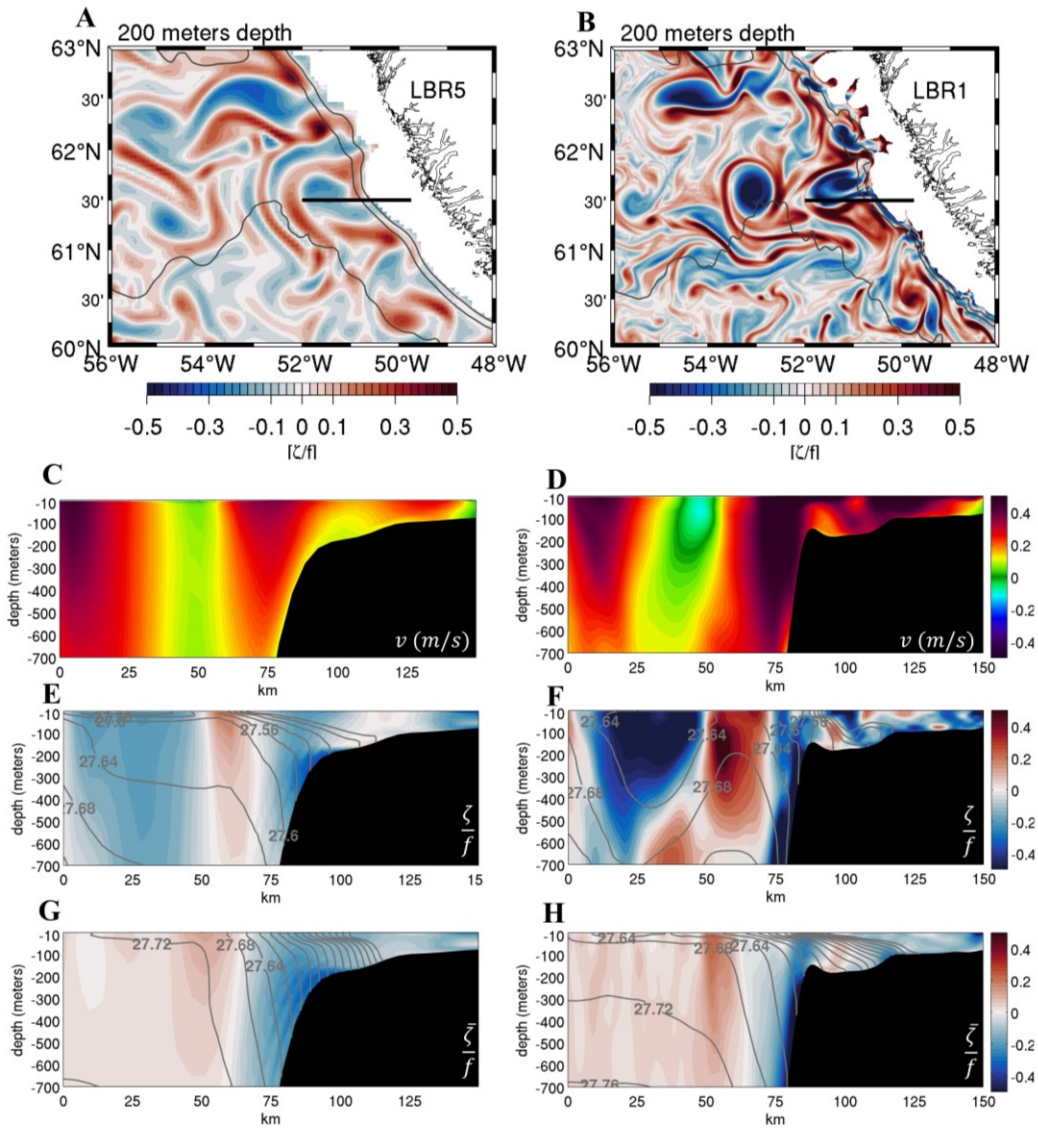

Figure 4. 7 Left column LBR5 and right column LBR1 simulations. (A-B): Relative vorticity normalized by Coriolis (ζ/f) at 200 m depth in wintertime zoomed over the constriction of the isobaths along West Greenland where IRs are formed. (C-D): Snapshot of meridional velocity in m s^{-1} along a transect at 61.5°N (black line in A-B panels) (times as in Fig. 1). (E-F): Snapshots of ζ/f with density isolines superposed. (G-H): ζ/f across the transect time-averaged over the 2009 convective season with corresponding density isolines superimposed.

4.4 Conclusions and Discussion

Our findings support the existence of a direct link between submesoscale instabilities and the Labrador Sea contribution to the global meridional overturning circulation. Model results reveal surprisingly large differences in the representation of Labrador Sea Water formation for varying resolution, with a 50 % reduction in the modeled volume of convected waters (calculated over the area where convection reaches depths greater than 1000 m) when mesoscale advection is included, and over 80% reduction if submesoscale processes are accounted for. Current state-of-the-art climate models do not fully resolve the mesoscale dynamics at high latitudes, and indeed tend to greatly overestimate the formation of Labrador Sea water (Li, Lozier et al. 2019). Interestingly, the model predicts a linear relationship between the amount of LSW formed, and the mean near-surface vorticity and/or the frontogenetic tendency along the west coast of Greenland, opening the possibility to a physically based parameterization of this contribution.

In the submesoscale permitting simulations, mesoscale anticyclonic eddies with submesoscale characteristics (in primis a Rossby number of order 1) and submesoscale cyclonic vorticity filaments form in correspondence of the intense horizontal shear layers induced by the Irminger Current interacting with the continental slope. These long-lived eddies (longer-lived and more intense than their counterpart in the mesoscale-resolving simulation) carry heat from the Irminger Current to the interior, effectively delimiting where deep convection takes place. They form independently of the near surface stratification along the Greenland coast, their generation being controlled by baroclinic instability associated with the bathymetry and not by the presence/absence of freshwater inputs from the Arctic and Greenland Ice Sheet. At the same time the large number of

submesoscale eddies formed locally in the region bounded by the 2000 m and 3000 m isobaths in the western portion of the basin controls locally the stratification, limiting the lateral extension towards the Labrador shelf of the convective patch.

Predicting the future evolution of the meridional overturning circulation and its persistence as global climate change progresses will hinge upon our ability to model the response of a multiscale environment.

This work provides physical context to the recent attribution of the differences in sea-level rise between the penultimate and last deglaciation to differences in subsurface warming in the North Atlantic subpolar gyre (Clark, He et al. 2020). It also helps understanding the lesser role of the Labrador Sea in the overall control of the state of the MOC argued through the analysis of recent OSNAP (Overturning in the Subpolar North Atlantic Program) data with respect to estimates from climate models, (Lozier, Li et al. 2019), while indicating that the representation of the interannual variability of the LSW formation can be captured independently of resolution.

Ultimately, these findings call for observational efforts aimed at carefully monitoring heat content and trends of the Irminger Current and point to the need for better investigating the rich complexity of interactions and feedbacks between processes localized at the ocean boundaries (in this case along the continental slope of West Greenland) and the global ocean, as they can affect the climate trajectory of our planet. They also call for parameterizations in earth system models that account for the advective role of coherent vortices generated by submesoscale instabilities in regions where submesoscale processes cascade to the larger (from basin to global) scales. For the LSW this can be easily achieved

by accounting for the linear relationship between convective volume and surface mean vorticity or frontogenetic tendency.

CHAPTER 5. SUMMARY AND FUTURE WORK

5.1 Understanding the North Atlantic response into a warming future

In this work I focused on the skill of the Earth System Models (ESMs) in representing the large-scale circulation, stratification, and the spatial distribution of physical and biogeochemical properties in the subpolar North Atlantic (Chapter 2 and 3). The ESMs ability to properly represent the North Atlantic convective regions during the historical period varies among models but all display significant biases in the representation of the position and strength of the NAC. As a consequence, the mean state of the physical and biogeochemical properties is not well represented (Frölicher, Rodgers et al. 2016). This inability to capture the mean state correctly cannot guarantee convergence or reliability in future projections. New and unique findings of this study are the projected resistance to deoxygenation in limited areas, generally found to the south of Greenland and along the Western Boundary Current, and the mechanisms that control this resistance. The existence of this nonuniform, patchy response is associated with the projected weakening of the NAC. This weakening has two distinct impacts on the projected changes in dissolved oxygen and nutrients. First, reduced northward heat transport is causing the formation of the so-called 'warming hole' south of Greenland, and secondly, as Chapter 3 suggest, nutrient advection in the Gulf Stream (GS) and its extension is changing in response to a weakening of the currents, shaping the response of the subtropical North Atlantic to future warming and deoxygenation.

It is important to notice that the Ocean General Circulation Models (OGCMs) analyzed in this first part of the thesis along the ESMs do not resolve the ocean mesoscale dynamics

due to their coarse spatial grid resolution, and mesoscale motions are accounted for only through sub-grid parametrizations (Gent and McWilliams 1990). Open questions related to the projection of future nutrient transport in the WBCs include: Are these models, which must parameterize the net effect of mesoscale motions, able to adequately represent the mechanisms of nutrient delivery and their evolution in current and future conditions?

5.2 Towards a better representation of Labrador Sea convection

Over the past two decades, the influence of submesoscale (~ km scale) circulations on the distribution of tracers at/near the ocean surface has been the focus of much research (e.g. (D'Asaro, Shcherbina et al. 2018, Su, Wang et al. 2018). These investigations have shown that submesoscale currents contribute substantially to the mixing of materials at the ocean surface (D'Asaro, Shcherbina et al. 2018), to the restratification of the mixed-layer (Fox-Kemper, Ferrari et al. 2008) and potentially to vertical heat fluxes in the mixed-layer (Su, Wang et al. 2018). To date, however, no study has been able to quantify systematic differences at climate-relevant and globally-relevant scales in the representation of offshore transport of heat and freshwater (and potentially nutrients and carbon), through processes that are submesoscale in nature.

The work of Chapter 4 points to a direct link between submesoscale instabilities along the West Greenland continental slope and the global overturning circulation. Eddies that are submesoscale in nature are generated along the coast of Greenland, where the Irminger Current approaches the continental shelf. These eddies the control lateral transport of heat and freshwater and the stratification in the center of the Labrador Sea, and in turn convection in winter. A linear relationship describes the dependence of the modeled multi-year-mean

convective volume and the frontogenetic tendency along the Greenland continental slope for varying model resolution. This work confirms that submesoscale turbulence scales-up to climate relevance, pointing to the urgency of including its advective contribution in Earth systems models. Additionally, this result contextualizes the lesser contribution of the Labrador Sea to the Meridional Overturning Circulation argued by the analysis of the Overturning in the Subpolar North Atlantic Program data with respect to Earth System Model predictions, and indicate a potential solution to correcting this fundamental model bias.

REFERENCES

Adcroft, A. and R. Hallberg (2006). "On methods for solving the oceanic equations of motion in generalized vertical coordinates." Ocean Modelling **11**(1-2): 224-233.

Antonov, J. I., D. Seidov, T. P. Boyer, R. A. Locarnini, A. V. Mishonov, H. E. Garcia, O. K. Baranova, M. M. Zweng and D. R. Johnson (2010). "World Ocean Atlas 2009, Volume 2: Salinity." S. Levitus **Volume 2**(U.S. Government Printing Office, Washington, D.C., 184 pp.).

Arrigo, K. R., G. L. van Dijken, R. M. Castelao, H. Luo, Å. K. Rennermalm, M. Tedesco, T. L. Mote, H. Oliver and P. L. Yager (2017). "Melting glaciers stimulate large summer phytoplankton blooms in southwest Greenland waters." Geophysical Research Letters **44**(12): 6278-6285.

Beckmann, A. and D. B. Haidvogel (1993). "Numerical Simulation of Flow around a Tall Isolated Seamount. Part I: Problem Formulation and Model Accuracy." Journal of Physical Oceanography **23**(8): 1736-1753.

Bentsen, M., I. Bethke, J. B. Debernard, T. Iversen, A. Kirkevag, O. Seland, H. Drange, C. Roelandt, I. A. Seierstad, C. Hoose and J. E. Kristjansson (2013). "The Norwegian Earth System Model, NorESM1-M - Part 1: Description and basic evaluation of the physical climate." Geoscientific Model Development **6**(3): 687-720.

Bentsen, M., H. Drange, T. Furevik and T. Zhou (2004). "Simulated variability of the Atlantic meridional overturning circulation." Climate Dynamics **22**(6-7): 701-720.

Biastoch, A., C. W. Boening, J. Getzlaff, J.-M. Molines and G. Madec (2008). "Causes of Interannual-Decadal Variability in the Meridional Overturning Circulation of the Midlatitude North Atlantic Ocean." Journal of Climate **21**(24): 6599-6615.

Boccaletti, G., R. Ferrari and B. Fox-Kemper (2007). "Mixed Layer Instabilities and Restratification." Journal of Physical Oceanography **37**(9): 2228-2250.

Boning, C. W., E. Behrens, A. Biastoch, K. Getzlaff and J. L. Bamber (2016). "Emerging impact of Greenland meltwater on deepwater formation in the North Atlantic Ocean." Nature Geoscience **9**(7): 523-+.

Bopp, L., C. Le Quere, M. Heimann, A. C. Manning and P. Monfray (2002). "Climate-induced oceanic oxygen fluxes: Implications for the contemporary carbon budget." Global Biogeochemical Cycles **16**(2).

Bopp, L., C. Le Quéré, M. Heimann, A. C. Manning and P. Monfray (2002). "Climate-induced oceanic oxygen fluxes: Implications for the contemporary carbon budget." Global Biogeochemical Cycles **16**(2): 6-1-6-13.

Bopp, L., L. Resplandy, J. C. Orr, S. C. Doney, J. P. Dunne, M. Gehlen, P. Halloran, C. Heinze, T. Ilyina, R. Seferian, J. Tjiputra and M. Vichi (2013). "Multiple stressors of ocean ecosystems in the 21st century: projections with CMIP5 models." Biogeosciences **10**(10): 6225-6245.

Bopp, L., L. Resplandy, J. C. Orr, S. C. Doney, J. P. Dunne, M. Gehlen, P. Halloran, C. Heinze, T. Ilyina, R. Séférian, J. Tjiputra and M. Vichi (2013). "Multiple stressors of ocean ecosystems in the 21st century: projections with CMIP5 models." Biogeosciences **10**(10): 6225-6245.

Bower, A. S., M. S. Lozier, S. F. Gary and C. W. Boning (2009). "Interior pathways of the North Atlantic meridional overturning circulation." Nature **459**(7244): 243-247.

Bracco, A., J. Choi, K. Joshi, H. Luo and J. C. McWilliams (2016). "Submesoscale currents in the northern Gulf of Mexico: Deep phenomena and dispersion over the continental slope." Ocean Modelling **101**: 43-58.

Bracco, A. and J. Pedlosky (2003). "Vortex Generation by Topography in Locally Unstable Baroclinic Flows." Journal of Physical Oceanography **33**(1): 207-219.

Bracco, A., J. Pedlosky and R. S. Pickart (2008). "Eddy formation near the West coast of Greenland." Journal of Physical Oceanography **38**(9): 1992-2002.

Brannigan, L., D. P. Marshall, A. Naveira-Garabato and A. J. George Nurser (2015). "The seasonal cycle of submesoscale flows." Ocean Modelling **92**: 69-84.

Broecker, W. S. and T.-H. Peng (1974). "Gas exchange rates between air and sea1." Tellus **26**(1-2): 21-35.

Caesar, L., S. Rahmstorf, A. Robinson, G. Feulner and V. Saba (2018). "Observed fingerprint of a weakening Atlantic Ocean overturning circulation." Nature **556**(7700): 191-196.

Callies, J., R. Ferrari, J. M. Klymak and J. Gula (2015). "Seasonality in submesoscale turbulence." Nature Communications **6**: 6862.

Canuto, V. M., A. Howard, P. Hogan, Y. Cheng, M. S. Dubovikov and L. M. Montenegro (2004). "Modeling ocean deep convection." Ocean Modelling **7**(1-2): 75-95.

Cape, M. R., F. Straneo, N. Beaird, R. M. Bundy and M. A. Charette (2019). "Nutrient release to oceans from buoyancy-driven upwelling at Greenland tidewater glaciers." Nature Geoscience **12**(1): 34-39.

Capet, X., J. C. McWilliams, M. J. Mokemaker and A. F. Shchepetkin (2008). "Mesoscale to submesoscale transition in the California current system. Part I: Flow structure, eddy flux, and observational tests." Journal of Physical Oceanography **38**(1): 29-43.

Capotondi, A., M. A. Alexander, N. A. Bond, E. N. Curchitser and J. D. Scott (2012). "Enhanced upper ocean stratification with climate change in the CMIP3 models." Journal of Geophysical Research-Oceans **117**.

Carton, J. A., G. A. Chepurin and L. Chen (2018). "SODA3: A New Ocean Climate Reanalysis." Journal of Climate **31**(17): 6967-6983.

Carton, J. A., B. S. Giese and S. A. Grodsky (2005). "Sea level rise and the warming of the oceans in the Simple Ocean Data Assimilation (SODA) ocean reanalysis." Journal of Geophysical Research-Oceans **110**(C9).

Chanut, J., B. Barnier, W. Large, L. Debreu, T. Penduff, J. M. Molines and P. Mathiot (2008). "Mesoscale eddies in the Labrador Sea and their contribution to convection and restratification." Journal of Physical Oceanography **38**(8): 1617-1643.

Clark, P. U., F. He, N. R. Golledge, J. X. Mitrovica, A. Dutton, J. S. Hoffman and S. Dendy (2020). "Oceanic forcing of penultimate deglacial and last interglacial sea-level rise." Nature **577**(7792): 660-664.

Clarke, R. A. and J. C. Gascard (1983). "THE FORMATION OF LABRADOR SEA-WATER .1. LARGE-SCALE PROCESSES." Journal of Physical Oceanography **13**(10): 1764-1778.

Cocco, V., F. Joos, M. Steinacher, T. L. Froelicher, L. Bopp, J. Dunne, M. Gehlen, C. Heinze, J. Orr, A. Oschlies, B. Schneider, J. Segschneider and J. Tjiputra (2013). "Oxygen and indicators of stress for marine life in multi-model global warming projections." Biogeosciences **10**(3): 1849-1868.

Cocco, V., F. Joos, M. Steinacher, T. L. Frölicher, L. Bopp, J. Dunne, M. Gehlen, C. Heinze, J. Orr, A. Oschlies, B. Schneider, J. Segschneider and J. Tjiputra (2013). "Oxygen and indicators of stress for marine life in multi-model global warming projections." Biogeosciences **10**(3): 1849-1868.

Collins, W. J., N. Bellouin, M. Doutriaux-Boucher, N. Gedney, P. Halloran, T. Hinton, J. Hughes, C. D. Jones, M. Joshi, S. Liddicoat, G. Martin, F. O'Connor, J. Rae, C. Senior, S. Sitch, I. Totterdell, A. Wiltshire and S. Woodward (2011). "Development and evaluation of an Earth-System model-HadGEM2." Geoscientific Model Development **4**(4): 1051-1075.

Cuny, J., P. B. Rhines, P. P. Niiler and S. Bacon (2002). "Labrador Sea Boundary Currents and the Fate of the Irminger Sea Water." Journal of Physical Oceanography **32**(2): 627-647.

Curry, R. and C. Mauritzen (2005). "Dilution of the northern North Atlantic Ocean in recent decades." Science **308**(5729): 1772-1774.

Curry, R. G., M. S. McCartney and T. M. Joyce (1998). "Oceanic transport of subpolar climate signals to mid-depth subtropical waters." Nature **391**(6667): 575-577.

Curry, W. B., J. C. Duplessy, L. D. Labeyrie and N. J. Shackleton (1988). "CHANGES IN THE DISTRIBUTION OF partial derivative C-13 OF DEEP WATER Sigma CO2 BETWEEN THE LAST GLACIATION AND THE HOLOCENE." Paleoceanography **3**(3): 317-341.

D'Asaro, E. A., A. Y. Shcherbina, J. M. Klymak, J. Molemaker, G. Novelli, C. M. Guigand, A. C. Haza, B. K. Haus, E. H. Ryan, G. A. Jacobs, H. S. Huntley, N. J. M. Laxague, S. Chen, F. Judt, J. C. McWilliams, R. Barkan, A. D. Kirwan, A. C. Poje and T. M. Özgökmen (2018). "Ocean convergence and the dispersion of flotsam." Proceedings of the National Academy of Sciences **115**(6): 1162-1167.

Danabasoglu, G., S. G. Yeager, D. Bailey, E. Behrens, M. Bentsen, D. Bi, A. Biastoch, C. Boening, A. Bozec, V. M. Canuto, C. Cassou, E. Chassignet, A. C. Coward, S. Danilov, N. Diansky, H. Drange, R. Farneti, E. Fernandez, P. G. Fogli, G. Forget, Y. Fujii, S. M. Griffies, A. Gusev, P. Heimbach, A. Howard, T. Jung, M. Kelley, W. G. Large, A. Leboissetier, J. Lu, G. Madec, S. J. Marsland, S. Masina, A. Navarra, A. J. G. Nurser, A. Pirani, D. Salas y Melia, B. L. Samuels, M. Scheinert, D. Sidorenko, A.-M. Treguier, H. Tsujino, P. Uotila, S. Valcke, A. Voldoire and Q. Wangi (2014). "North Atlantic simulations in Coordinated Ocean-ice Reference Experiments phase II (CORE-II). Part I: Mean states." Ocean Modelling **73**: 76-107.

Danabasoglu, G., S. G. Yeager, D. Bailey, E. Behrens, M. Bentsen, D. Bi, A. Biastoch, C. Boning, A. Bozec, V. M. Canuto, C. Cassou, E. Chassignet, A. C. Coward, S. Danilov, N. Diansky, H. Drange, R. Farneti, E. Fernandez, P. G. Fogli, G. Forget, Y. Fujii, S. M. Griffies, A. Gusev, P. Heimbach, A. Howard, T. Jung, M. Kelley, W. G. Large, A. Leboissetier, J. Lu, G. Madec, S. J. Marsland, S. Masina, A. Navarra, A. J. G. Nurser, A. Pirani, D. S. Y. Melia, B. L. Samuels, M. Scheinert, D. Sidorenko, A. M. Treguier, H. Tsujino, P. Uotila, S. Valcke, A. Voldoire and Q. Wangi (2014). "North Atlantic simulations in Coordinated Ocean-ice Reference Experiments phase II (CORE-II). Part I: Mean states." Ocean Modelling **73**: 76-107.

Danabasoglu, G., S. G. Yeager, W. M. Kim, E. Behrens, M. Bentsen, D. H. Bi, A. Biastoch, R. Bleck, C. Boning, A. Bozec, V. M. Canuto, C. Cassou, E. Chassignet, A. C. Coward, S. Danilov, N. Diansky, H. Drange, R. Farneti, E. Fernandez, P. G. Fogli, G. Forget, Y. Fujii, S. M. Griffies, A. Gusev, P. Heimbach, A. Howard, M. Ilicak, T. Jung, A. R. Karspeck, M. Kelley, W. G. Large, A. Leboissetier, J. H. Lu, G. Madec, S. J. Marsland, S. Masina, A. Navarra, A. J. G. Nurser, A. Pirani, A. Romanou, D. S. Y. Melia, B. L. Samuels, M. Scheinert, D. Sidorenko, S. Sun, A. M. Treguier, H. Tsujino, P. Uotila, S. Valcke, A. Voldoire, Q. Wang and I. Yashayaev (2016). "North Atlantic simulations in Coordinated Ocean-ice Reference Experiments phase II (CORE-II). Part II: Inter-annual to decadal variability." Ocean Modelling **97**: 65-90.

Danabasoglu, G., S. G. Yeager, Y. O. Kwon, J. J. Tribbia, A. S. Phillips and J. W. Hurrell (2012). "Variability of the Atlantic Meridional Overturning Circulation in CCSM4." Journal of Climate **25**(15): 5153-5172.

Debreu, L., P. Marchesiello, P. Penven and G. Cambon (2012). "Two-way nesting in split-explicit ocean models: Algorithms, implementation and validation." Ocean Modelling **49-50**: 1-21.

Debreu, L., C. Vouland and E. Blayo (2008). "AGRIF: Adaptive grid refinement in Fortran." Computers & Geosciences **34**(1): 8-13.

Dee, D. P., S. M. Uppala, A. J. Simmons, P. Berrisford, P. Poli, S. Kobayashi, U. Andrae, M. A. Balmaseda, G. Balsamo, P. Bauer, P. Bechtold, A. C. M. Beljaars, L. van de Berg, J. Bidlot, N. Bormann, C. Delsol, R. Dragani, M. Fuentes, A. J. Geer, L. Haimberger, S. B. Healy, H. Hersbach, E. V. Hólm, L. Isaksen, P. Kållberg, M. Köhler, M. Matricardi, A. P. McNally, B. M. Monge-Sanz, J.-J. Morcrette, B.-K. Park, C. Peubey, P. de Rosnay, C. Tavolato, J.-N. Thépaut and F. Vitart (2011). "The ERA-Interim reanalysis: configuration and performance of the data assimilation system." Quarterly Journal of the Royal Meteorological Society **137**(656): 553-597.

Delworth, T. L. and R. J. Greatbatch (2000). "Multidecadal thermohaline circulation variability driven by atmospheric surface flux forcing." Journal of Climate **13**(9): 1481-1495.

Dickson, B., I. Yashayaev, J. Meincke, B. Turrell, S. Dye and J. Holfort (2002). "Rapid freshening of the deep North Atlantic Ocean over the past four decades." Nature **416**(6883): 832-837.

Dickson, R., B. Rudels, S. Dye, M. Karcher, J. Meincke and I. Yashayaev (2007). "Current estimates of freshwater flux through Arctic and subarctic seas." Progress in Oceanography **73**(3-4): 210-230.

Doney, S. C., M. Ruckelshaus, J. E. Duffy, J. P. Barry, F. Chan, C. A. English, H. M. Galindo, J. M. Grebmeier, A. B. Hollowed, N. Knowlton, J. Polovina, N. N. Rabalais, W. J. Sydeman and L. D. Talley (2012). Climate Change Impacts on Marine Ecosystems. Annual Review of Marine Science, Vol 4. C. A. Carlson and S. J. Giovannoni. Palo Alto, Annual Reviews. **4:** 11-37.

Drijfhout, S., G. J. v. Oldenborgh and A. Cimatoribus (2012). "Is a Decline of AMOC Causing the Warming Hole above the North Atlantic in Observed and Modeled Warming Patterns?" Journal of Climate **25**(24): 8373-8379.

Dufresne, J. L., M. A. Foujols, S. Denvil, A. Caubel, O. Marti, O. Aumont, Y. Balkanski, S. Bekki, H. Bellenger, R. Benshila, S. Bony, L. Bopp, P. Braconnot, P. Brockmann, P. Cadule, F. Cheruy, F. Codron, A. Cozic, D. Cugnet, N. de Noblet, J. P. Duvel, C. Ethe, L. Fairhead, T. Fichefet, S. Flavoni, P. Friedlingstein, J. Y. Grandpeix, L. Guez, E. Guilyardi, D. Hauglustaine, F. Hourdin, A. Idelkadi, J. Ghattas, S. Joussaume, M. Kageyama, G. Krinner, S. Labetoulle, A. Lahellec, M. P. Lefebvre, F. Lefevre, C. Levy, Z. X. Li, J. Lloyd, F. Lott, G. Madec, M. Mancip, M. Marchand, S. Masson, Y. Meurdesoif, J. Mignot, I. Musat, S. Parouty, J. Polcher, C. Rio, M. Schulz, D. Swingedouw, S. Szopa, C. Talandier, P. Terray, N. Viovy and N. Vuichard (2013). "Climate change projections using the IPSL-

CM5 Earth System Model: from CMIP3 to CMIP5." Climate Dynamics **40**(9-10): 2123-2165.

Dunne, J. P., J. G. John, A. J. Adcroft, S. M. Griffies, R. W. Hallberg, E. Shevliakova, R. J. Stouffer, W. Cooke, K. A. Dunne, M. J. Harrison, J. P. Krasting, S. L. Malyshev, P. C. D. Milly, P. J. Phillipps, L. T. Sentman, B. L. Samuels, M. J. Spelman, M. Winton, A. T. Wittenberg and N. Zadeh (2012). "GFDL's ESM2 Global Coupled Climate–Carbon Earth System Models. Part I: Physical Formulation and Baseline Simulation Characteristics." Journal of Climate **25**(19): 6646-6665.

Dunne, J. P., J. G. John, E. Shevliakova, R. J. Stouffer, J. P. Krasting, S. L. Malyshev, P. C. D. Milly, L. T. Sentman, A. J. Adcroft, W. Cooke, K. A. Dunne, S. M. Griffies, R. W. Hallberg, M. J. Harrison, H. Levy, A. T. Wittenberg, P. J. Phillips and N. Zadeh (2013). "GFDL's ESM2 Global Coupled Climate-Carbon Earth System Models. Part II: Carbon System Formulation and Baseline Simulation Characteristics." Journal of Climate **26**(7): 2247-2267.

Eden, C. and C. Böning (2002). "Sources of Eddy Kinetic Energy in the Labrador Sea." Journal of Physical Oceanography **32**(12): 3346-3363.

Eden, C. and J. Willebrand (2001). "Mechanism of interannual to decadal variability of the North Atlantic circulation." Journal of Climate **14**(10): 2266-2280.

Feely, R. A., C. L. Sabine, K. Lee, W. Berelson, J. Kleypas, V. J. Fabry and F. J. Millero (2004). "Impact of anthropogenic CO2 on the CaCO3 system in the oceans." Science **305**(5682): 362-366.

Fettweis, X., B. Franco, M. Tedesco, J. H. van Angelen, J. T. M. Lenaerts, M. R. van den Broeke and H. Gallee (2013). "Estimating the Greenland ice sheet surface mass balance contribution to future sea level rise using the regional atmospheric climate model MAR." Cryosphere **7**(2): 469-489.

Fischer, J., F. A. Schott and M. Dengler (2004). "Boundary circulation at the exit of the Labrador Sea." Journal of Physical Oceanography **34**(7): 1548-1570.

Fox-Kemper, B., R. Ferrari and R. Hallberg (2008). "Parameterization of mixed layer eddies. Part I: Theory and diagnosis." Journal of Physical Oceanography **38**(6): 1145-1165.

Frajka-Williams, E., P. B. Rhines and C. C. Eriksen (2014). "Horizontal Stratification during Deep Convection in the Labrador Sea." Journal of Physical Oceanography **44**(1): 220-228.

Froelicher, T. L., F. Joos, G. K. Plattner, M. Steinacher and S. C. Doney (2009). "Natural variability and anthropogenic trends in oceanic oxygen in a coupled carbon cycle-climate model ensemble." Global Biogeochemical Cycles **23**.

Frölicher, T. L., F. Joos, G.-K. Plattner, M. Steinacher and S. C. Doney (2009). "Natural variability and anthropogenic trends in oceanic oxygen in a coupled carbon cycle–climate model ensemble." Global Biogeochemical Cycles **23**(1).

Frölicher, T. L., K. B. Rodgers, C. A. Stock and W. W. L. Cheung (2016). "Sources of uncertainties in 21st century projections of potential ocean ecosystem stressors." Global Biogeochemical Cycles **30**(8): 1224-1243.

Fu, W., J. Randerson and J. K. Moore (2015). "Climate change impacts on net primary production (NPP) and export production (EP) regulated by increasing stratification and phytoplankton community structure in CMIP5 models." Biogeosciences Discuss. **2015**: 12851-12897.

Gallée, H. and G. Schayes (1994). "Development of a Three-Dimensional Meso-γ Primitive Equation Model: Katabatic Winds Simulation in the Area of Terra Nova Bay, Antarctica." Monthly Weather Review **122**(4): 671-685.

Garcia, H. E., R. A. Locarnini, T. P. Boyer, J. I. Antonov, O. K. Baranova, M. M. Zweng and D. R. Johnson (2010). "World Ocean Atlas 2009, Volume 3: Dissolved Oxygen, Apparent Oxygen Utilization, and Oxygen Saturation." S. Levitus **Ed. NOAA Atlas NESDIS 70**.

Garcia. and L. I. Gordon (1992). "Oxygen solubility in seawater: Better fitting equations." Limnology and Oceanography **37**(6): 1307-1312.

Gent, P. R. and J. C. McWilliams (1990). "ISOPYCNAL MIXING IN OCEAN CIRCULATION MODELS." Journal of Physical Oceanography **20**(1): 150-155.

Gillett, N. P., D. A. Stone, P. A. Stott, T. Nozawa, A. Y. Karpechko, G. C. Hegerl, M. F. Wehner and P. D. Jones (2008). "Attribution of polar warming to human influence." Nature Geoscience **1**(11): 750-754.

Giorgetta, M. A., J. Jungclaus, C. H. Reick, S. Legutke, J. Bader, M. Boettinger, V. Brovkin, T. Crueger, M. Esch, K. Fieg, K. Glushak, V. Gayler, H. Haak, H.-D. Hollweg, T. Ilyina, S. Kinne, L. Kornblueh, D. Matei, T. Mauritsen, U. Mikolajewicz, W. Mueller, D. Notz, F. Pithan, T. Raddatz, S. Rast, R. Redler, E. Roeckner, H. Schmidt, R. Schnur, J. Segschneider, K. D. Six, M. Stockhause, C. Timmreck, J. Wegner, H. Widmann, K.-H. Wieners, M. Claussen, J. Marotzke and B. Stevens (2013). "Climate and carbon cycle changes from 1850 to 2100 in MPI-ESM simulations for the Coupled Model Intercomparison Project phase 5." Journal of Advances in Modeling Earth Systems **5**(3): 572-597.

Giorgetta, M. A., J. Jungclaus, C. H. Reick, S. Legutke, J. Bader, M. Böttinger, V. Brovkin, T. Crueger, M. Esch, K. Fieg, K. Glushak, V. Gayler, H. Haak, H.-D. Hollweg, T. Ilyina, S. Kinne, L. Kornblueh, D. Matei, T. Mauritsen, U. Mikolajewicz, W. Mueller, D. Notz, F. Pithan, T. Raddatz, S. Rast, R. Redler, E. Roeckner, H. Schmidt, R. Schnur, J. Segschneider, K. D. Six, M. Stockhause, C. Timmreck, J. Wegner, H. Widmann, K.-H. Wieners, M. Claussen, J. Marotzke and B. Stevens (2013). "Climate and carbon cycle

changes from 1850 to 2100 in MPI-ESM simulations for the Coupled Model Intercomparison Project phase 5." Journal of Advances in Modeling Earth Systems **5**(3): 572-597.

Grantham, B. A., F. Chan, K. J. Nielsen, D. S. Fox, J. A. Barth, A. Huyer, J. Lubchenco and B. A. Menge (2004). "Upwelling-driven nearshore hypoxia signals ecosystem and oceanographic changes in the northeast Pacific." Nature **429**(6993): 749-754.

Gray, J. S., R. S. S. Wu and Y. Y. Or (2002). "Effects of hypoxia and organic enrichment on the coastal marine environment." Marine Ecology Progress Series **238**: 249-279.

Griffies, S. M., J. Yin, P. J. Durack, P. Goddard, S. C. Bates, E. Behrens, M. Bentsen, D. Bi, A. Biastoch, C. W. Boening, A. Bozec, E. Chassignet, G. Danabasoglu, S. Danilov, C. M. Domingues, H. Drange, R. Farneti, E. Fernandez, R. J. Greatbatch, D. M. Holland, M. Ilicak, W. G. Large, K. Lorbacher, J. Lu, S. J. Marsland, A. Mishra, A. J. G. Nurser, D. Salas y Melia, J. B. Palter, B. L. Samuels, J. Schroeter, F. U. Schwarzkopf, D. Sidorenko, A. M. Treguier, Y.-h. Tseng, H. Tsujino, P. Uotila, S. Valcke, A. Voldoire, Q. Wang, M. Winton and X. Zhang (2014). "An assessment of global and regional sea level for years 1993-2007 in a suite of interannual CORE-II simulations." Ocean Modelling **78**: 35-89.

Gruber, N. (2011). "Warming up, turning sour, losing breath: ocean biogeochemistry under global change." Philos Trans A Math Phys Eng Sci **369**(1943): 1980-1996.

Hanna, E., P. Huybrechts, K. Steffen, J. Cappelen, R. Huff, C. Shuman, T. Irvine-Fynn, S. Wise and M. Griffiths (2008). "Increased Runoff from Melt from the Greenland Ice Sheet: A Response to Global Warming." Journal of Climate **21**(2): 331-341.

Hatun, H., C. C. Eriksen and P. B. Rhines (2007). "Buoyant eddies entering the Labrador Sea observed with gliders and altimetry." Journal of Physical Oceanography **37**(12): 2838-2854.

Hawkins, E. and R. Sutton (2009). "THE POTENTIAL TO NARROW UNCERTAINTY IN REGIONAL CLIMATE PREDICTIONS." Bulletin of the American Meteorological Society **90**(8): 1095-+.

Holte, J., L. D. Talley, J. Gilson and D. Roemmich (2017). "An Argo mixed layer climatology and database." Geophysical Research Letters **44**(11): 5618-5626.

Hopwood, M. J., D. Carroll, T. J. Browning, L. Meire, J. Mortensen, S. Krisch and E. P. Achterberg (2018). "Non-linear response of summertime marine productivity to increased meltwater discharge around Greenland." Nature Communications **9**(1): 3256.

Hoskins, B. J. (1982). "The Mathematical Theory of Frontogenesis." Annual Review of Fluid Mechanics **14**(1): 131-151.

Huang, B., V. F. Banzon, E. Freeman, J. Lawrimore, W. Liu, T. C. Peterson, T. M. Smith, P. W. Thorne, S. D. Woodruff and H.-M. Zhang (2015). "Extended Reconstructed Sea

Surface Temperature Version 4 (ERSST.v4). Part I: Upgrades and Intercomparisons." Journal of Climate **28**(3): 911-930.

Ito, T., M. J. Follows and E. A. Boyle (2004). "Is AOU a good measure of respiration in the oceans?" Geophysical Research Letters **31**(17).

Ito, T., S. Minobe, M. C. Long and C. Deutsch (2017). "Upper ocean O2 trends: 1958–2015." Geophysical Research Letters **44**(9): 4214-4223.

Jones, H. and J. Marshall (1997). "Restratification after deep convection." Journal of Physical Oceanography **27**(10): 2276-2287.

Katsman, C. A., M. A. Spall and R. S. Pickart (2004). "Boundary Current Eddies and Their Role in the Restratification of the Labrador Sea." Journal of Physical Oceanography **34**(9): 1967-1983.

Keeling, R. F., A. Koertzinger and N. Gruber (2010). "Ocean Deoxygenation in a Warming World." Annual Review of Marine Science **2**: 199-229.

Kleypas , Feely RA, Fabry VJ, Langdon C, Sabine CL and R. LL. (2006). Impacts of ocean acidification on coral reefs and other marine calcifiers: a guide for future research. . St. Petersburg, Florida**:** 88 pp.

Kleypas, J. A., R. W. Buddemeier, D. Archer, J. P. Gattuso, C. Langdon and B. N. Opdyke (1999). "Geochemical consequences of increased atmospheric carbon dioxide on coral reefs." Science **284**(5411): 118-120.

Kortzinger, A., J. Schimanski, U. Send and D. Wallace (2004). "The ocean takes a deep breath." Science **306**(5700): 1337-1337.

Large, W. G., J. C. McWilliams and S. C. Doney (1994). "Oceanic vertical mixing: A review and a model with a nonlocal boundary layer parameterization." Reviews of Geophysics **32**(4): 363-403.

Lazier, J. (1980). "Oceanographic conditions at Ocean Weather Ship Bravo, 1964–1974." Atmosphere-Ocean **18**(3): 227-238.

Lazier, J. (1988). "Temperature and salinity changes in the deep Labrador Sea, 1962–1986." Deep Sea Research Part A. Oceanographic Research Papers **35**(8): 1247-1253.

Lazier, J., R. Hendry, A. Clarke, I. Yashayaev and P. Rhines (2002). "Convection and restratification in the Labrador Sea, 1990-2000." Deep-Sea Research Part I-Oceanographic Research Papers **49**(10): 1819-1835.

Lazier, J. R. N. (1988). "TEMPERATURE AND SALINITY CHANGES IN THE DEEP LABRADOR SEA, 1962-1986." Deep-Sea Research Part a-Oceanographic Research Papers **35**(8): 1247-1253.

Letscher, R. T., F. Primeau and J. K. Moore (2016). "Nutrient budgets in the subtropical ocean gyres dominated by lateral transport." Nature Geosci **9**(11): 815-819.

Letscher, R. T., F. Primeau and J. K. Moore (2016). "Nutrient budgets in the subtropical ocean gyres dominated by lateral transport." Nature Geoscience **9**: 815.

Li, F., M. S. Lozier, G. Danabasoglu, N. P. Holliday, Y.-O. Kwon, A. Romanou, S. G. Yeager and R. Zhang (2019). "Local and Downstream Relationships between Labrador Sea Water Volume and North Atlantic Meridional Overturning Circulation Variability." Journal of Climate **32**(13): 3883-3898.

Lilly, J. M., P. B. Rhines, F. Schott, K. Lavender, J. Lazier, U. Send and E. D'Asaro (2003). "Observations of the Labrador Sea eddy field." Progress in Oceanography **59**(1): 75-176.

Locarnini, R. A., A. V. Mishonov, J. I. Antonov, T. P. Boyer, H. E. Garcia, O. K. Baranova, M. M. Zweng and D. R. Johnson (2010

). "World Ocean Atlas 2009, Volume 1 : Temperature. S. Levitus." **Volume 1**(Ed. NOAA Atlas NESDIS 68, U.S. Government Printing Office, Washington, D.C.): 184 pp.

Long, M. C., K. Lindsay, S. Peacock, J. K. Moore and S. C. Doney (2013). "Twentieth-Century Oceanic Carbon Uptake and Storage in CESM1(BGC)." Journal of Climate **26**(18): 6775-6800.

Lozier, M. S., F. Li, S. Bacon, F. Bahr, A. S. Bower, S. A. Cunningham, M. F. de Jong, L. de Steur, B. deYoung, J. Fischer, S. F. Gary, B. J. W. Greenan, N. P. Holliday, A. Houk, L. Houpert, M. E. Inall, W. E. Johns, H. L. Johnson, C. Johnson, J. Karstensen, G. Koman, I. A. Le Bras, X. Lin, N. Mackay, D. P. Marshall, H. Mercier, M. Oltmanns, R. S. Pickart, A. L. Ramsey, D. Rayner, F. Straneo, V. Thierry, D. J. Torres, R. G. Williams, C. Wilson, J. Yang, I. Yashayaev and J. Zhao (2019). "A sea change in our view of overturning in the subpolar North Atlantic." Science **363**(6426): 516-521.

Luo, H., A. Bracco and E. Di Lorenzo (2011). "The interannual variability of the surface eddy kinetic energy in the Labrador Sea." Progress in Oceanography **91**(3): 295-311.

Luo, H., A. Bracco, I. Yashayaev and E. Di Lorenzo (2012). "The interannual variability of potential temperature in the central Labrador Sea." Journal of Geophysical Research: Oceans **117**(C10).

Luo, H., A. Bracco and F. Zhang (2014). "The Seasonality of Convective Events in the Labrador Sea." Journal of Climate **27**(17): 6456-6471.

Luo, H., R. M. Castelao, A. K. Rennermalm, M. Tedesco, A. Bracco, Patricia L. Yager and T. L. Mote (2016). "Oceanic transport of surface meltwater from the southern Greenland ice sheet." Nature Geoscience **9**: 528.

MacMartin, D. G., E. Tziperman and L. Zanna (2013). "Frequency Domain Multimodel Analysis of the Response of Atlantic Meridional Overturning Circulation to Surface Forcing." Journal of Climate **26**(21): 8323-8340.

Marshall, J., F. Dobson, K. Moore, P. Rhines, M. Visbeck, E. d'Asaro, K. Bumke, S. Chang, R. Davis, K. Fischer, R. Garwood, P. Guest, R. Harcourt, C. Herbaut, T. Holt, J. Lazier, S. Legg, J. McWilliams, R. Pickart, M. Prater, I. Renfrew, F. Schott, U. Send, W. Smethie and G. Lab Sea (1998). "The Labrador Sea deep convection experiment." Bulletin of the American Meteorological Society **79**(10): 2033-2058.

Marshall, J. and F. Schott (1999). "Open-ocean convection: Observations, theory, and models." Reviews of Geophysics **37**(1): 1-64.

Mason, E., J. Molemaker, A. Shchepetkin, F. Colas, J. C. McWilliams and P. Sangrà (2010). "Procedures for offline grid nesting in regional ocean models." Ocean Modelling **35**: 1-15.

Matear, R. J., A. C. Hirst and B. I. McNeil (2000). "Changes in dissolved oxygen in the Southern Ocean with climate change." Geochemistry Geophysics Geosystems **1**.

McCartney, M. S. and L. D. Talley (1982). "THE SUB-POLAR MODE WATER OF THE NORTH-ATLANTIC OCEAN." Journal of Physical Oceanography **12**(11): 1169-1188.

McWilliams, J. C. (2016). "Submesoscale currents in the ocean." Proceedings of the Royal Society A: Mathematical, Physical and Engineering Sciences **472**(2189): 20160117.

McWilliams, J. C., J. Gula, M. J. Molemaker, L. Renault and A. F. Shchepetkin (2015). "Filament Frontogenesis by Boundary Layer Turbulence." Journal of Physical Oceanography **45**(8): 1988-2005.

Meehl, G. A. and T. F. Stocker (2007). Global Climate Projections.

Mensa, J. A., Z. Garraffo, A. Griffa, T. M. Özgökmen, A. Haza and M. Veneziani (2013). "Seasonality of the submesoscale dynamics in the Gulf Stream region." Ocean Dynamics **63**(8): 923-941.

Mernild, S. H. and G. E. Liston (2012). "Greenland Freshwater Runoff. Part II: Distribution and Trends, 1960-2010." Journal of Climate **25**(17): 6015-6035.

Molemaker, M. J., J. C. McWilliams and W. K. Dewar (2015). "Submesoscale Instability and Generation of Mesoscale Anticyclones near a Separation of the California Undercurrent." Journal of Physical Oceanography **45**(3): 613-629.

Moore, J. K., W. Fu, F. Primeau, G. L. Britten, K. Lindsay, M. Long, S. C. Doney, N. Mahowald, F. Hoffman and J. T. Randerson (2018). "Sustained climate warming drives declining marine biological productivity." Science **359**(6380): 1139-1143.

Moore, J. K., K. Lindsay, S. C. Doney, M. C. Long and K. Misumi (2013). "Marine Ecosystem Dynamics and Biogeochemical Cycling in the Community Earth System Model [CESM1(BGC)]: Comparison of the 1990s with the 2090s under the RCP4.5 and RCP8.5 Scenarios." Journal of Climate **26**(23): 9291-9312.

Moore, J. K., K. Lindsay, S. C. Doney, M. C. Long and K. Misumi (2013). "Marine Ecosystem Dynamics and Biogeochemical Cycling in the Community Earth System Model CESM1(BGC) : Comparison of the 1990s with the 2090s under the RCP4.5 and RCP8.5 Scenarios." Journal of Climate **26**(23): 9291-9312.

Myers, P. G. (2005). "Impact of freshwater from the Canadian Arctic Archipelago on Labrador Sea Water formation." Geophysical Research Letters **32**(6).

Najjar, R. and R. Keeling (1997). Analysis of the mean annual cycle of the dissolved oxygen anomaly in the World Ocean.

Oliver, H., H. Luo, R. M. Castelao, G. L. van Dijken, K. S. Mattingly, J. J. Rosen, T. L. Mote, K. R. Arrigo, Å. K. Rennermalm, M. Tedesco and P. L. Yager (2018). "Exploring the Potential Impact of Greenland Meltwater on Stratification, Photosynthetically Active Radiation, and Primary Production in the Labrador Sea." Journal of Geophysical Research: Oceans **123**(4): 2570-2591.

Orr, J. C., V. J. Fabry, O. Aumont, L. Bopp, S. C. Doney, R. A. Feely, A. Gnanadesikan, N. Gruber, A. Ishida, F. Joos, R. M. Key, K. Lindsay, E. Maier-Reimer, R. Matear, P. Monfray, A. Mouchet, R. G. Najjar, G. K. Plattner, K. B. Rodgers, C. L. Sabine, J. L. Sarmiento, R. Schlitzer, R. D. Slater, I. J. Totterdell, M. F. Weirig, Y. Yamanaka and A. Yool (2005). "Anthropogenic ocean acidification over the twenty-first century and its impact on calcifying organisms." Nature **437**(7059): 681-686.

Palter, J. B., M. S. Lozier and R. T. Barber (2005). "The effect of advection on the nutrient reservoir in the North Atlantic subtropical gyre." Nature **437**: 687.

Palter, J. B., M. S. Lozier and R. T. Barber (2005). "The effect of advection on the nutrient reservoir in the North Atlantic subtropical gyre." Nature **437**(7059): 687-692.

Pelegrí, J. L. and G. T. Csanady (1991). "Nutrient transport and mixing in the Gulf Stream." Journal of Geophysical Research: Oceans **96**(C2): 2577-2583.

Penn, J. L., C. Deutsch, J. L. Payne and E. A. Sperling (2018). "Temperature-dependent hypoxia explains biogeography and severity of end-Permian marine mass extinction." Science **362**(6419): eaat1327.

Penven, P., P. Marchesiello, L. Debreu and J. Lefèvre (2008). "Software tools for pre- and post-processing of oceanic regional simulations." Environmental Modelling & Software **23**(5): 660-662.

Pickart, R. S., D. J. Torres and R. A. Clarke (2002). "Hydrography of the Labrador Sea during Active Convection." Journal of Physical Oceanography **32**(2): 428-457.

Plattner, G. K., F. Joos and T. F. Stocker (2002). "Revision of the global carbon budget due to changing air-sea oxygen fluxes." Global Biogeochemical Cycles **16**(4).

Poertner, H. O. and R. Knust (2007). "Climate change affects marine fishes through the oxygen limitation of thermal tolerance." Science **315**(5808): 95-97.

Prater, M. D. (2002). "Eddies in the Labrador Sea as Observed by Profiling RAFOS Floats and Remote Sensing." Journal of Physical Oceanography **32**(2): 411-427.

Rahmstorf, S., J. E. Box, G. Feulner, M. E. Mann, A. Robinson, S. Rutherford and E. J. Schaffernicht (2015). "Exceptional twentieth-century slowdown in Atlantic Ocean overturning circulation." Nature Climate Change **5**: 475.

Rahmstorf, S., J. E. Box, G. Feulner, M. E. Mann, A. Robinson, S. Rutherford and E. J. Schaffernicht (2015). "Exceptional twentieth-century slowdown in Atlantic Ocean overturning circulation." Nature Climate Change **5**(5): 475-480.

Reynaud, T. H., A. J. Weaver and R. J. Greatbatch (1995). "SUMMER MEAN CIRCULATION OF THE NORTHWESTERN ATLANTIC-OCEAN." Journal of Geophysical Research-Oceans **100**(C1): 779-816.

Riahi, K., S. Rao, V. Krey, C. Cho, V. Chirkov, G. Fischer, G. Kindermann, N. Nakicenovic and P. Rafaj (2011). "RCP 8.5-A scenario of comparatively high greenhouse gas emissions." Climatic Change **109**(1-2): 33-57.

Riahi, K., S. Rao, V. Krey, C. Cho, V. Chirkov, G. Fischer, G. Kindermann, N. Nakicenovic and P. Rafaj (2011). "RCP 8.5—A scenario of comparatively high greenhouse gas emissions." Climatic Change **109**(1): 33.

Rignot, E., J. E. Box, E. Burgess and E. Hanna (2008). "Mass balance of the Greenland ice sheet from 1958 to 2007." Geophysical Research Letters **35**(20).

Rykaczewski, R. R. and J. P. Dunne (2010). "Enhanced nutrient supply to the California Current Ecosystem with global warming and increased stratification in an earth system model." Geophysical Research Letters **37**(21).

Saenko, O. A., F. Dupont, D. Yang, P. G. Myers, I. Yashayaev and G. C. Smith (2014). "Role of Resolved and Parameterized Eddies in the Labrador Sea Balance of Heat and Buoyancy." Journal of Physical Oceanography **44**(12): 3008-3032.

Sarmiento, J. L. and N. Gruber (2006). Ocean Biogeochemical Dynamics, Princeton University Press.

Sarmiento, J. L., T. M. C. Hughes, R. J. Stouffer and S. Manabe (1998). "Simulated response of the ocean carbon cycle to anthropogenic climate warming." Nature **393**(6682): 245-249.

Sathiyamoorthy, S. and G. W. K. Moore (2002). "Buoyancy flux at Ocean Weather Station Bravo." Journal of Physical Oceanography **32**(2): 458-474.

Schmidtko, S., L. Stramma and M. Visbeck (2017). "Decline in global oceanic oxygen content during the past five decades." Nature **542**: 335.

Schulze Chretien, L. M. and E. Frajka-Williams (2018). "Wind-driven transport of fresh shelf water into the upper 30 m of the Labrador Sea." Ocean Sci. **14**(5): 1247-1264.

Schulzweida, U. (2019). "CDO User Guide." Zenodo.

Shchepetkin, A. F. and J. C. McWilliams (2003). "A method for computing horizontal pressure-gradient force in an oceanic model with a nonaligned vertical coordinate." Journal of Geophysical Research: Oceans **108**(C3).

Shchepetkin, A. F. and J. C. McWilliams (2005). "The regional oceanic modeling system (ROMS): a split-explicit, free-surface, topography-following-coordinate oceanic model." Ocean Modelling **9**(4): 347-404.

Smith, W. H. F. and D. T. Sandwell (1997). "Global Sea Floor Topography from Satellite Altimetry and Ship Depth Soundings." Science **277**(5334): 1956-1962.

Spall, M. A. (2004). "Boundary currents and watermass transformation in marginal seas." Journal of Physical Oceanography **34**(5): 1197-1213.

Srinivasan, K., J. C. McWilliams, M. J. Molemaker and R. Barkan (2019). "Submesoscale Vortical Wakes in the Lee of Topography." Journal of Physical Oceanography **49**(7): 1949-1971.

Stendardo, I. and N. Gruber (2012). "Oxygen trends over five decades in the North Atlantic." Journal of Geophysical Research-Oceans **117**.

Stewart, K. D., A. M. Hogg, S. M. Griffies, A. P. Heerdegen, M. L. Ward, P. Spence and M. H. England (2017). "Vertical resolution of baroclinic modes in global ocean models." Ocean Modelling **113**: 50-65.

Stouffer, R. J., J. Yin, J. M. Gregory, K. W. Dixon, M. J. Spelman, W. Hurlin, A. J. Weaver, M. Eby, G. M. Flato, H. Hasumi, A. Hu, J. H. Jungclaus, I. V. Kamenkovich, A. Levermann, M. Montoya, S. Murakami, S. Nawrath, A. Oka, W. R. Peltier, D. Y. Robitaille, A. Sokolov, G. Vettoretti and S. L. Weber (2006). "Investigating the causes of the response of the thermohaline circulation to past and future climate changes." Journal of Climate **19**(8): 1365-1387.

Stramma, L., G. C. Johnson, J. Sprintall and V. Mohrholz (2008). "Expanding Oxygen-Minimum Zones in the Tropical Oceans." Science **320**(5876): 655-658.

Straneo, F. (2006). "Heat and freshwater transport through the central Labrador Sea." Journal of Physical Oceanography **36**(4): 606-628.

Su, Z., J. Wang, P. Klein, A. F. Thompson and D. Menemenlis (2018). "Ocean submesoscales as a key component of the global heat budget." Nature Communications **9**(1): 775.

Sun, D., T. Ito and A. Bracco (2017). "Oceanic Uptake of Oxygen During Deep Convection Events Through Diffusive and Bubble-Mediated Gas Exchange." Global Biogeochemical Cycles **31**(10): 1579-1591.

Tagklis, F., A. Bracco and T. Ito (2017). "Physically driven patchy O2 changes in the North Atlantic Ocean simulated by the CMIP5 Earth system models." Global Biogeochemical Cycles **31**(8): 1218-1235.

Talley, L. D. and M. S. McCartney (1982). "DISTRIBUTION AND CIRCULATION OF LABRADOR SEA-WATER." Journal of Physical Oceanography **12**(11): 1189-1205.

Talley, L. D., G. L. Pickard, W. J. Emery and J. H. Swift (2011). Chapter 1 - Introduction to Descriptive Physical Oceanography. Descriptive Physical Oceanography (Sixth Edition). L. D. Talley, G. L. Pickard, W. J. Emery and J. H. Swift. Boston, Academic Press**:** 1-6.

Taylor, K. E., R. J. Stouffer and G. A. Meehl (2012). "AN OVERVIEW OF CMIP5 AND THE EXPERIMENT DESIGN." Bulletin of the American Meteorological Society **93**(4): 485-498.

Vage, K., R. S. Pickart, V. Thierry, G. Reverdin, C. M. Lee, B. Petrie, T. A. Agnew, A. Wong and M. H. Ribergaard (2009). "Surprising return of deep convection to the subpolar North Atlantic Ocean in winter 2007-2008." Nature Geoscience **2**(1): 67-72.

van Aken, H. M., M. F. de Jong and I. Yashayaev (2011). "Decadal and multi-decadal variability of Labrador Sea Water in the north-western North Atlantic Ocean derived from tracer distributions: Heat budget, ventilation, and advection." Deep-Sea Research Part I-Oceanographic Research Papers **58**(5): 505-523.

Wanninkhof, R. (1992). "RELATIONSHIP BETWEEN WIND-SPEED AND GAS-EXCHANGE OVER THE OCEAN." Journal of Geophysical Research-Oceans **97**(C5): 7373-7382.

Williams, R. G., E. McDonagh, V. M. Roussenov, S. Torres-Valdes, B. King, R. Sanders and D. A. Hansell (2011). "Nutrient streams in the North Atlantic: Advective pathways of inorganic and dissolved organic nutrients." Global Biogeochemical Cycles **25**: 16.

Williams, R. G., E. McDonagh, V. M. Roussenov, S. Torres-Valdes, B. King, R. Sanders and D. A. Hansell (2011). "Nutrient streams in the North Atlantic: Advective pathways of inorganic and dissolved organic nutrients." Global Biogeochemical Cycles **25**(4).

Williams, R. G., V. Roussenov and M. J. Follows (2006). "Nutrient streams and their induction into the mixed layer." Global Biogeochemical Cycles **20**(1): 18.

Williams, R. G., V. Roussenov and M. J. Follows (2006). "Nutrient streams and their induction into the mixed layer." Global Biogeochemical Cycles **20**(1).

Yamamoto, A., J. B. Palter, C. O. Dufour, S. M. Griffies, D. Bianchi, M. Claret, J. P. Dunne, I. Frenger and E. D. Galbraith (2018). "Roles of the Ocean Mesoscale in the Horizontal Supply of Mass, Heat, Carbon, and Nutrients to the Northern Hemisphere Subtropical Gyres." Journal of Geophysical Research: Oceans **0**(0).

Yashayaev, I. (2007). "Changing freshwater content: Insights from the subpolar North Atlantic and new oceanographic challenges." Progress in Oceanography **73**(3-4): 203-209.

Yashayaev, I. (2007). "Hydrographic changes in the Labrador Sea, 1960-2005." Progress in Oceanography **73**(3-4): 242-276.

Yashayaev, I., M. Bersch and H. M. van Aken (2007). "Spreading of the Labrador Sea Water to the Irminger and Iceland basins." Geophysical Research Letters **34**(10).

Yashayaev, I. and D. Seidov (2015). "The role of the Atlantic Water in multidecadal ocean variability in the Nordic and Barents Seas." Progress in Oceanography **132**: 68-127.